HAL open science

A binuclear cobalt complex for molecular CO_2 electrocatalysis

Antoine Bohn, Juan José Moreno, Pierre Thuéry, Marc Robert, Orestes Rivada-Wheelaghan

To cite this version:

Antoine Bohn, Juan José Moreno, Pierre Thuéry, Marc Robert, Orestes Rivada-Wheelaghan. A binuclear cobalt complex for molecular CO_2 electrocatalysis. 2021. cea-03468211

HAL Id: cea-03468211

https://cea.hal.science/cea-03468211v1

Preprint submitted on 7 Dec 2021

HAL is a multi-disciplinary open access archive for the deposit and dissemination of scientific research documents, whether they are published or not. The documents may come from teaching and research institutions in France or abroad, or from public or private research centers.

L'archive ouverte pluridisciplinaire **HAL**, est destinée au dépôt et à la diffusion de documents scientifiques de niveau recherche, publiés ou non, émanant des établissements d'enseignement et de recherche français ou étrangers, des laboratoires publics ou privés.

Distributed under a Creative Commons Attribution - NonCommercial - NoDerivatives 4.0 International License

A Binuclear Cobalt Complex for Molecular CO_2 Electrocatalysis

Antoine Bohn,[a] Juan José Moreno,[b] Pierre Thuéry,[c] Marc Robert,[a,d] and Orestes Rivada–Wheelaghan*[a]

[a] Dr. A. Bohn, Prof. M. Robert and Dr. O. Rivada–Wheelaghan
Laboratoire d'Electrochimie Moléculaire
Université de Paris, CNRS
F–75006 Paris, France
E–mail: orestes.rivada@u–paris.fr

[b] Dr. J. J. Moreno
Instituto de Investigaciones Químicas (IIQ), Departamento de Química Inorgánica and Centro de Innovación en Química Avanzada (ORFEO–CINQA)
Consejo Superior de Investigaciones Científicas (CSIC) and University of Sevilla
Avenida Américo Vespucio 49, 41092 Sevilla (Spain)

[c] Dr. P. Thuéry
NIMBE
UniversitéParis–Saclay, CEA, CNRS,
91191 Gif–sur–Yvette, France.

[d] Prof. M. Robert
Institut Universitaire de France (IUF)
F–75005 Paris, France.

Abstract: A pyrazole–based ligand substituted with terpyridine groups at the 3 and 5positions has been synthesized to form the dinuclear cobalt complex **1**, that electrocatalytically reduces carbon dioxide (CO_2) to carbon monoxide (CO) in the presence of Brønsted acids in DMF. Chemical, electrochemical and UV–vis spectro–electrochemical studies under inert atmosphere indicate a single 2 electron reduction process of complex **1** at first, followed by a 1 electron reduction at the ligand. Infrared spectro–electrochemical studies under CO_2 and CO atmosphere allowed us to identify a reduced CO–containing dicobalt complex

which results from the electroreduction of CO_2. In the presence of trifluoroethanol (TFE), electrocatalytic studies revealed single–site mechanism with up to 94 % selectivity towards CO formation when 1.47 M TFE were present, at –1.35 V *vs* Saturated Calomel Electrode in DMF (0.39 V overpotential). The low faradaic efficiencies obtained (<50%) are attributed to the generation of CO–containing species formed during the electrocatalytic process, which inhibit the reduction of CO_2.

Introduction

Mishandling of global resources has led to anthropogenic climate change.[1] To decrease its harmful effects and *Make Our Planet Great Again*,[2] shifts towards renewable energy storage,[3] circular feedstocks,[4] and energy–efficient processes are required.[5] Consequently, molecular electrocatalysis has experienced a renewed interest,[6–8] since it can contribute to sustainable and energy–efficient organic redox chemistry,[9–11] and to develop new strategies towards energy storage applications.[7,12] Along these lines, bimetallic electrocatalytic systems have been synthesized and broadly studied aiming towards energy storage transformations,[13,14] such as water oxidation,[15] oxygen reduction,[16] hydrogen evolution reaction,[17] nitrogen reduction,[18] or carbon dioxide reduction[19] (Figure 1). Moreover, advances on the understanding of the structure and reactivity of metal–based cofactors has caused the growth of bioinspired multimetallic molecular systems,[13,20,21] to exploit their cooperative–reactivity potential.[22] A recent example of bioinspired bimetallic electrocatalysis for CO_2 transformation was recently published by Duboc *et al.*, in which a NiFe–hydrogenase model promoted the conversion of CO_2 to CH_4 in aqueous solutions at pH 4 with 16% faradaic efficiency (FE).[23] Another relevant example of bimetallic electrocatalyst was reported by Bowman *et al.*, where a dicopper molecular system yielded 12 equivalents of oxalate from CO_2 at –0.03 V *versus* the normal hydrogen electrode.[24] As with this two examples, no metal–metal interaction has been reported to participate during molecular bimetallic electrocatalytic reduction of CO_2,[7,19] with cooperativity arising from bimetallic substrate activation in some cases.[25] In this regard, pyrazole–based ligands are well–stablished platforms that allow such reactivity.[26] Under the right synthetic conditions, the

deprotonated pyrazolate acts as an *exo*–bridge that generates the desired bimetallic complex. However, depending on the metal precursor and substituents at 3,5–positions at the N–heterocycle not only homo– or hetero–bimetallic complexes can be formed, but also mono– and polynuclear species (Figure 1).[26,27]

In our search for new molecular systems that can electrochemically activate and reduce CO_2,[28,29] we decided to synthesize a new bimetallic molecular complex bearing a pyrazole–core substituted with terpyridine groups at the 3,5–positions (Figure 1). Although this approach blocks the possibility of *exo*–bimetallic substrate activation,[30] ligands bearing a terpyridine fragment have shown the ability to reduce the overpotential for CO_2 electroreduction through metal–ligand cooperativity.[31–33] Additionally, the new synthesized ligand structure would generate a complex with structural similarities to the $[Co^{II}(qpy)(H_2O)_2]^{2+}$ electrocatalyst (qpy = 2,2':6',2'':6'',2'''–quaterpyridine), which our group has thoroughly studied,[34–36] and that could serve as a mononuclear comparative system (Figure 1). Thus, in this report we describe the synthesis and characterization of a new bimetallic molecular Co^{II}–complex and its electrochemical characterization under inert atmosphere. We studied its electrocatalytic activity towards CO_2 reduction in the absence and presence of Brønsted acids, including its distinct behavior in different organic solvents.

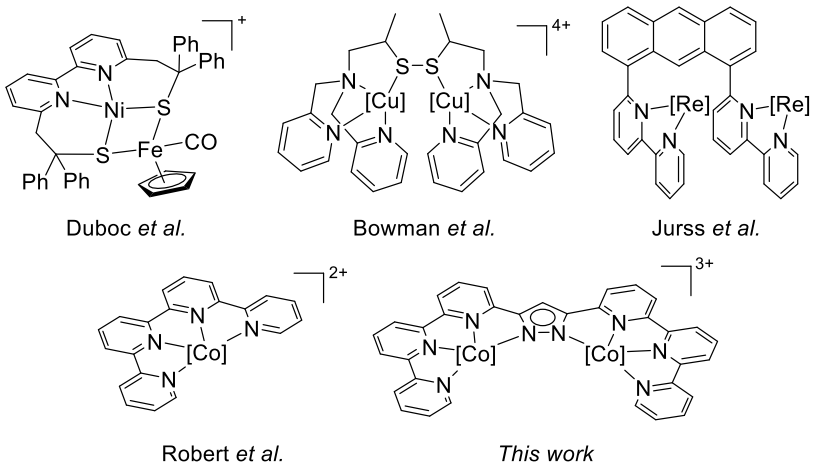

Figure 1. Bimetallic complexes used as electrocatalyst for the transformation of CO_2 (top). Monometallic cobalt electrocatalyst for CO_2 reduction and new bicobalt–based electrocatalyst for CO_2 reduction (bottom).

Results and Discussion

Ligand and complex synthesis and characterization.

The pyrazole–based ligand, 3,5–bis{6–(2,2':6',2"–terpyridine)}pyrazole, **L–H**, has been characterized by NMR and high resolution mass spectrometry (HRMS) and was obtained in 30 % yield, by reacting synthesized 6–methyl–2,2':6',2"–terpyridine carboxylate with 6–acetyl 2,2':6',2"–terpyridine, following reported procedures.[37] **L–H** exhibits low solubility in most solvents, presenting a symmetrical pattern in the ^{1}H and ^{13}C{^{1}H} NMR spectra, with the characteristic H–signal from the 4–position of the pyrazole ring appearing at 7.84 ppm in DMSO–d_6 (Figure S9). **L–H** was suspended in THF and deprotonated with 1.1 equivalents of ^{t}BuOK. Once a clear orange solution was formed, 2 equivalents of $CoCl_2$ were added, followed by 5 equivalents of $AgBF_4$ and MeCN. The reaction was left stirring overnight protected from light inside the glovebox. Mixture purification generated the desired complex **1**, $[Co^{II}_2(L)(MeCN)_4][BF_4]_3$ in high yields (Scheme 1).

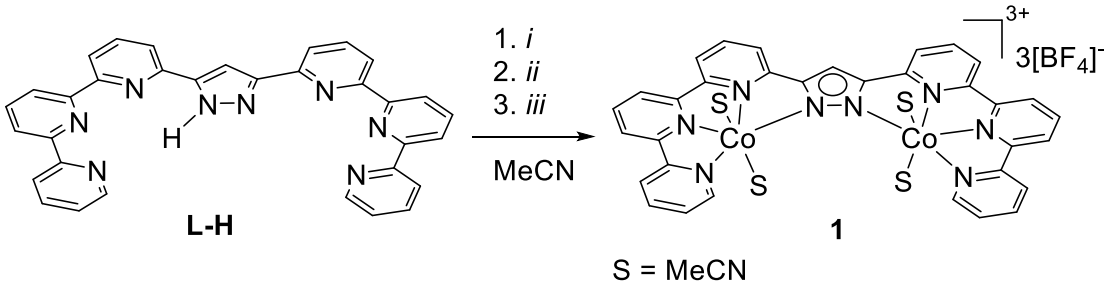

Scheme 1. Complex synthesis. *i*: 1.1 equivalent of ^{t}BuOK in THF; *ii*: 2 equivalents of $CoCl_2$ in THF; *iii*: 5 equivalents of $AgBF_4$ in MeCN.

Complex **1** crystallizes from concentrate MeCN/toluene solutions at room temperature, yielding large orange crystals suitable for single-crystal X–ray diffraction. As expected, the deprotonated ligand **L** binds to two Co^{II} atoms, where each center is six–coordinated and binds besides the terpyridine fragment (terpy)

and a N–atom from the pyrazolate, two N–atoms from coordinated MeCN at the apical positions. Thus, **1** is a tricationic dicobalt (II) complex, with **L** sharing a negative charge with both metal centers (Figure 2). Complex **1** is paramagnetic and thus silent by ^{1}H NMR (μ_{eff} = 6.232 BM).[38] The lower effective magnetic moment observed compared to a previously reported high–spin bimetallic octahedral Co^{II} complex,[39] might reflect the distorted octahedral geometry observed at each Co^{II}center.[40] Interestingly, previously reported bimetallic Co^{II} complexes stabilized with pyrazolate core ligands have shown antiferromagnetic coupling.[41]

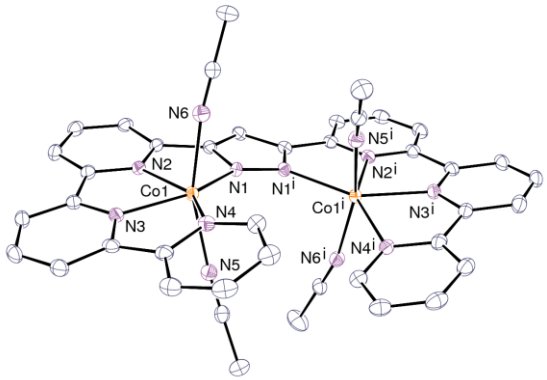

Figure 2. ORTEP view of complex **1**. Displacement ellipsoids are drawn at the 50% probability level and counterions, solvent molecules and hydrogen atoms are omitted.

Electrochemical studies.

We analyzed the redox properties of complex **1** by cyclic voltammetry (CV). The electrochemical measurements were performed in dry solvents (MeCN or DMF) using a glassy carbon working electrode, a Pt–counter electrode, and a Saturated Calomel Electrode (SCE) as a reference electrode (at constant T = 293 K). As observed in Figure 3, CV analysis of **1** (0.5 mM) in dry MeCN with 0.1 M Bu_4NPF_6 under Ar exhibited three redox events at –0.69 ($R1_{Ar}^{MeCN}$), –1.14 ($R2_{Ar}^{MeCN}$) and –1.56 ($R3_{Ar}^{MeCN}$) V *vs* SCE. The first cathodic wave at redox event $R1_{Ar}^{MeCN}$ (solid red, Figure 3) is diffusion controlled and the other two more negative waves resemble adsorption phenomena. We applied the methodology developed by Amatore *et*

al. to determine the value of the electron stoichiometry corresponding to the first electrochemical wave (Figures S21–S23).[42] This method is based on comparison of the currents measured by a pair of analytical techniques such as chronoamperometry with microelectrodes and cyclic voltammetry using ultramicroelectrodes. Knowing the number of electrons involved at the first redox event in MeCN, we could determine the diffusion coefficient (D) of complex **1**. Thus, after variable scan rate analysis and application of the Randles–Sevcik equation, we obtained $D = 2.1 \cdot 10^{-6}$ cm^2 s^{-1}.[43]

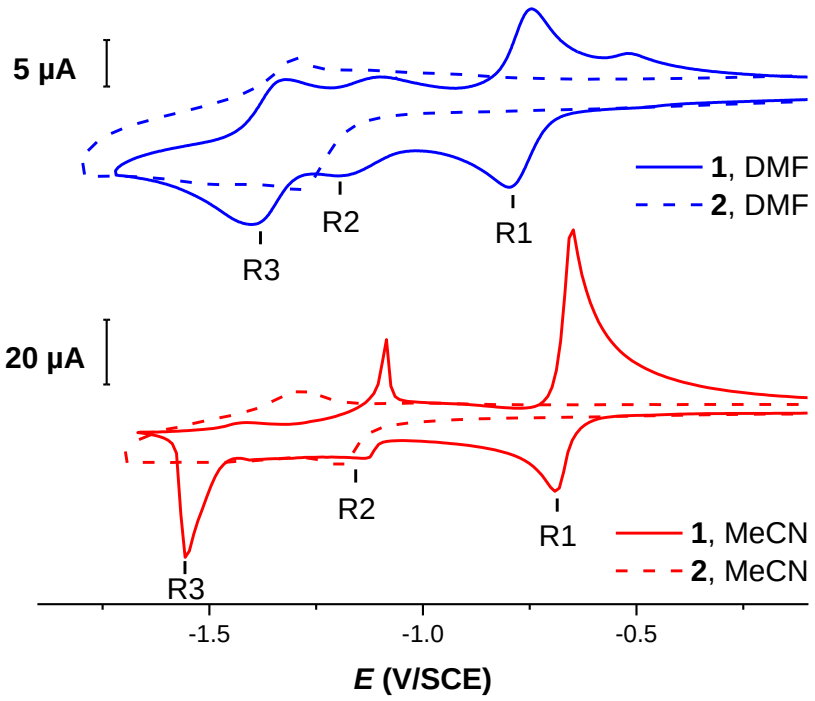

Figure 3. CVs of complexes **1** (line) and **2** (dotted line), 0.5 mM, in anhydrous DMF (blue) and MeCN (red) with 0.1 M of $TBAPF_6$, at 20 °C and scan rate of 0.1 $V \cdot s^{-1}$.

In addition, to gain further insight into the nature of the electrogenerated species at such potentials, we performed thin–layer UV–vis spectroelectrochemistry (UV–SEC), since it could provide useful information about the intermediate formed in the reaction layer surrounding the electrode surface. As it can be observed in Figure 4, the spectra exhibit the appearance of 2 new bands centered at 400 and 500 nm (bordeaux), when the experiment was performed at room temperature under argon atmosphere. Being a reversible

process, application of a positive voltage forms back complex **1**, generating the initial spectrum (blue). Moreover, we analyzed by UV–vis the reduction reaction of **1** with 2 equivalents of cobaltocene in MeCN since the one–electron redox couple potential of cobaltocene falls between the $R2_{Ar}^{MeCN}$ and $R1_{Ar}^{MeCN}$ (E°_{CoCp2}= –0.9 V *vs* SCE).[44] As it is observed in Figure 4, the wave obtained (green) is similar to the electrogenerated species (bordeaux), supporting our assignment of a two–electron reduction process at $R1_{Ar}^{MeCN}$. The high absorbance observed at 260 nm corresponds to the presence of 2 equivalents of cobaltocenium in solution.[45] Unfortunately, the reduced complex is unstable, leading to the disappearance of the band when the solution is left for 30 min under Ar at room temperature. Attempts to isolate the reduced species through glovebox or Schlenk techniques were unfruitful.

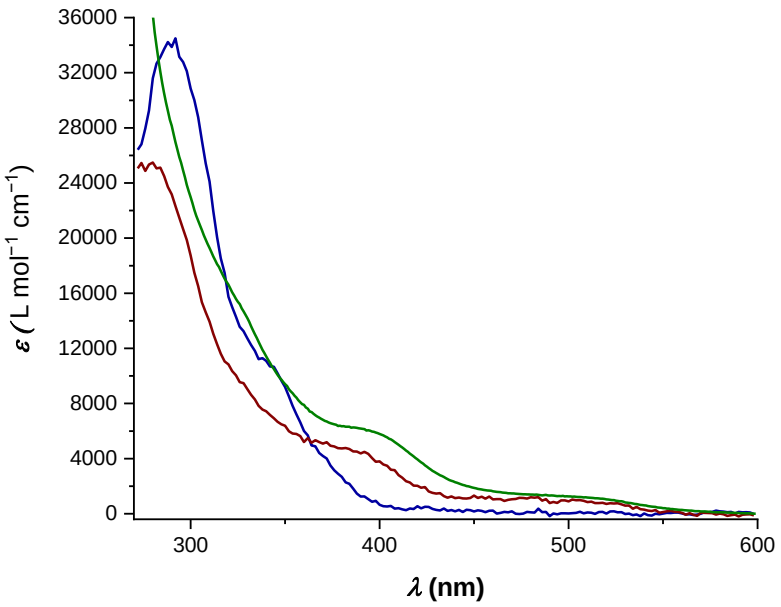

Figure 4. Blue: UV–vis spectrum of complex **1** in MeCN (0.1 M $TBAPF_6$). Bordeaux: UV–vis spectrum of electrogenerated species in MeCN (0.1 M $TBAPF_6$). Green: UV–vis spectrum from reacting complex **1** with 2 equivalents of cobaltocene in MeCN.

Neither Amatore's methodology nor thin–layer UV–SEC allowed us to determine the number of electrons involved at the second or third redox events, due to non–diffusive processes involved beyond –1 V *vs* SCE.

Fortunately, CV analysis of **1** in dry DMF exhibits three diffusion controlled redox events observed at –0.79 ($R1_{Ar}^{DMF}$), –1.18 ($R2_{Ar}^{DMF}$) and –1.40 ($R3_{Ar}^{DMF}$) V *vs* SCE, with a 2:1:2 ratio (Figure 3, solid blue). Potentiostatic coulometry of complex **1** in DMF confirmed the consumption of 5 electrons in a 2:1:2 process when the potential applied was –1.62 V (Figure S33). To understand solvation effects, we added increasing amounts of MeCN to a solution of **1** (0.5 mM) in DMF (0.1 M $TBAPF_6$) and *vice versa*. We observed that while solutions of **1** in DMF were not affected by consecutive additions of MeCN, solutions of **1** in MeCN evolve gradually with the addition of DMF, generating the same CV as if recorded in DMF (Figure S32). This observation sheds light into the redox events $R1_{Ar}^{SOLV}$, $R2_{Ar}^{SOLV}$ and $R3_{Ar}^{SOLV}$(for SOLV = DMF or MeCN), reflecting a different electrochemical response due to solvent coordination to the bimetallic complex and the corresponding reduced form.[46]

Being the redox event at $R2_{Ar}^{SOLV}$ suggestive of a reduction event centered on the ligand platform (Figure 3).[31,32,34,35] To gain further insight into this process, the analogous Zn complex **2** was synthesized and characterized. CV of **2** in DMF or MeCN under similar conditions exhibited a cathodic wave, which falls between $R2_{Ar}^{SOLV}$ and $R3_{Ar}^{SOLV}$ for complex **1** (Figure 3, dashed curves). These results, along with previous studies regarding transition metal complexes bearing terpy fragments,[31,32,34,35] indicates that $R2_{Ar}^{SOLV}$ may corresponds to a one electron reduction at the ligand platform. Thus, we have tentatively assigned $R2_{Ar}^{SOLV}$ for complex **1** to a one electron the reduction occurring at the ligand. Finally, based on the potentiostatic coulometry of complex **1** in DMF (*vide supra*) the cathodic wave $R3_{Ar}^{SOLV}$ was assigned to a two–electron reduction process.

Electrochemical studies under CO_2.

Under CO_2 atmosphere complex **1** exhibits irreversibility at the first redox event, $R1_{CO2}$, when the cathodic wave $R4_{CO2}$ is reached and the slight current increase observed at the third cathodic wave ($R3_{CO2}$,) is due to presence of traces of water, *vide infra* (Figure 5, Left).[47] A catalytic current enhancement is observed at potentials ca. –1.55 V, with a peak at ca. –1.90 V ($R4_{CO2}$,). When $R4_{CO2}$ is reached, a new anodic wave at

0.28 V appears in the CV, which has been assigned to cobalt CO–containing species, since CVs performed under CO atmosphere resembled the same anodic event (Figures S46–S48).

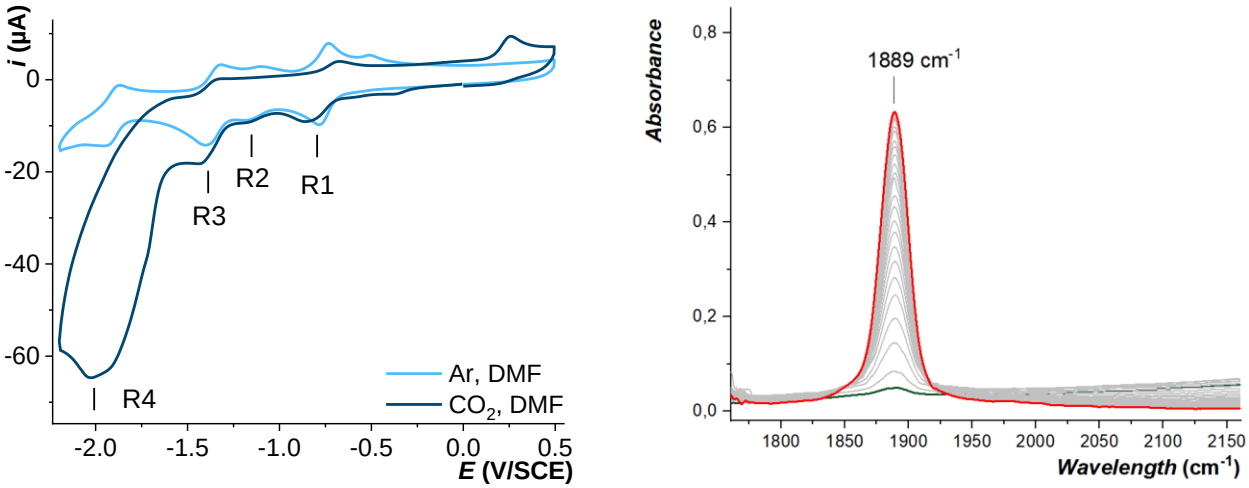

Figure 5. **Left**, CVs of complex **1** (0.5 mM) in anhydrous DMF with 0.1 M of $TBAPF_6$, at 20 °C and scan rate of 0.1 $V \cdot s^{-1}$, under argon (light blue) and CO_2 atmosphere (dark blue). **Right**, FT–IR−SEC spectra of a 0.5 M $TBAPF_6$/DMF solution of **1** (6 mM) under CO_2 at – 1.6 V *vs* Ag wire.

To obtain *in situ* information during the electroreduction of CO_2, infrared spectroelectrochemistry (IR–SEC) was performed from –1 to –2 V (*vs* Ag wire) to solutions of complex **1** in DMF under CO_2 atmosphere. The spectra obtained from IR–SEC experiments at –1.6 V *vs* Ag wire exhibited a new IR band at 1889 cm^{-1}, assigned to a CO–containing dicobalt complex (Figure 5, Right). This band is not observed when complex **1** is dissolved in DMF and its IR measured under CO atmosphere. However, if a potential of –1 V *vs* Ag wire is applied to this solution, the IR band at 1889 cm^{-1} is generated (Figure S50). Thus, we presume that the band corresponds to a reduced dicobalt carbonyl complex. This also agrees with the observed anodic wave at 0.28 V *vs* SCE in DMF, *vide supra* (Figure 5, Left). To gain further knowledge on the electrocatalytic activity, controlled potential electrolysis (CPE) of **1** (0.5 mM) in DMF (−2.05 V *vs.* SCE) was conducted using a glassy carbon plate as the working electrode. The gaseous headspace of the sealed

electrolysis cells was analyzed after the experiment, exhibiting to our surprise non−substantial amounts of CO gas produced in DMF. During the first 15 minutes of CPE, the chronoamperogram exhibited rapid current inhibition. CV of the remaining DMF solution generated a similar current as prior to the CPE, indicating that the current decrease during CPE is due to electrode surface passivation (Table S3).

Electrochemical studies in the presence of Brønsted acids.

Weak Brønsted acids have been reported to promote the catalytic electroreduction of CO_2,[48] by stabilizing the electrogenerated [M–CO_2] adduct and facilitating the cleavage of the C−O bond during the conversion to CO.[49] Since CO was detected during the electroreduction of CO_2 by **1**, we investigated the effects that different weak Brønsted acids such as water, phenol (PhOH) or TFE could have in the electroreduction of CO_2.[47] Water addition during CV studies of **1** in DMF ($TBAPF_6$, 0.1 M) under CO_2 atmosphere shifted by in 100 mV the cathodic wave $R1_{CO2}^{Water}$ to more negative potentials, indicating water coordination to the Co–centers (Figure 6A).[35] Additionally, a new fivefold current increase in the electrocatalytic wave $R2_{DMF}^{Water}$ with respect to $R1_{CO2}^{Water}$ at ca. –1.35 V was observed.[50] During a 3 h CPE, under saturated CO_2 atmosphere at –1.4 V, 4 TONs of CO and 5 TONs of H_2 were generated (0.5 mM of **1**, 0.5 M $TBAPF_6$ and 5 M water in DMF). CV analysis of the solution before and after CPE exhibited different redox behavior and rinse test analysis from the glassy carbon plate used during the CPE exhibited electrocatalytic activity (Table S4). Thus, heterogeneous catalysis arising from complex **1** derivatization/decomposition cannot be ruled out during CPE performance.[51]

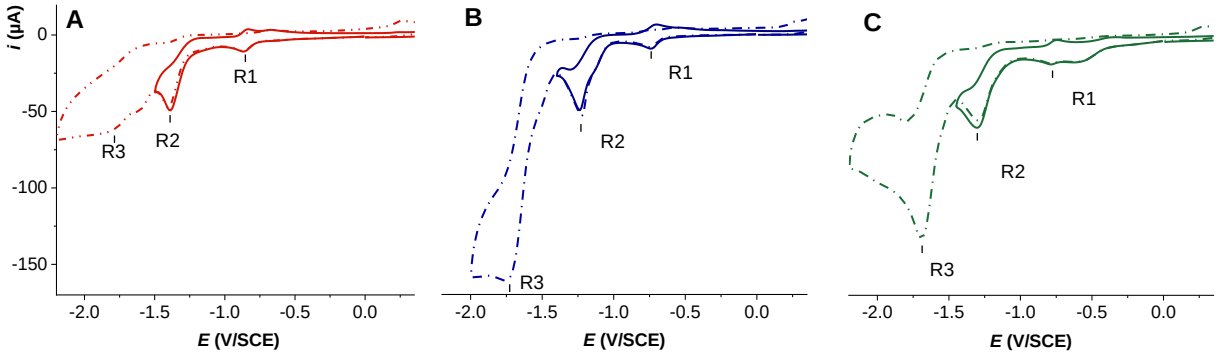

Figure 6. CVs of complex **1** (0.5 mM) under CO_2 atmosphere, in anhydrous DMF with 0.1 M of $TBAPF_6$, at 20 °C and can rate of 0.1 V·s⁻1, in the presence of 1.94 M of water (red), **A**; 3 M of PhOH (blue), **B**; and 1.47 M of TFE (green), **C**.

Later, we investigated the addition of PhOH to solutions of **1**, which generated a new electrocatalytic wave, $R2_{CO2}^{PhOH}$, at less negative potentials (ca. –1.23 V) and observing reversibility at the redox event $R1_{CO2}^{PhOH}$ (Figure 6B). CPEs performed at ca. –1.3 V in the presence of 3 M PhOH, yielded higher CO TONs (12) and less H_2 TONs (3), than when water was present. CV analysis of the remaining solution showed higher current than before CPE, due to the formation of electrocatalytically active material deposited on the electrode surface during CPE (Table S5). Thus, although the electrocatalytic response under the new conditions did improve, heterogeneous pathways for electrocatalysis rising form complex **1** derivatization under the reaction conditions cannot be ruled out. Moreover, in the presence of PhOH a second large electrocatalytic wave ($R3_{CO2}^{PhOH}$) at ca. –1.75 V is observed in the CV (Figure 7B). A 3 h CPE under the same previous conditions but at –1.8 V applied potential generated more hydrogen (13 TONs) keeping similar amounts of CO formed (12 TONs). The higher H_2 formation may rise from competitive reactivity favored at more negative potentials such as hydrogen evolution reaction,[52,53] and decomposition process.[51] Finally, addition of TFE to solutions of **1** generated a new pre–wave for $R1_{CO2}^{TFE}$ at ca. –0.55 V, with $R1_{CO2}^{TFE}$ exhibiting at slightly more positive potentials, plus an electrocatalytic wave $R2_{CO2}^{TFE}$ at ca. –1.3 V (Figure 6C). We were pleased to find that a 3 h CPE performed at –1.35 V (1.47 M TFE) yielded higher selectivity

for CO conversion compared to water or PhOH (94 %, 17 TONs of CO and 1 TON of H_2). Moreover, using same conditions, CPE performed under $^{13}CO_2$ atmosphere generated ^{13}CO (Figure S62). From its rinse test analysis, CV before and after CPE and shape of the chronoamperogram, we conclude that complex **1** presents higher stability under these last conditions. This becomes clearer from CPE performed for 1 hour, in which the CVs before and after CPE remain almost identical (Table S11).

Table 1. Electrochemical response from CPE experiments.

Bronsted Acid	CO		H_2		Selectivity (CO formation)	Potential (V)
	TON	FE(%)	TON	FE(%)		
5M Water	4	18	5	21	44 %	–1.40
3M PhOH	12	41	3	11	80 %	–1.30
3M TFE	17	39	1	2	94 %	–1.35

Conditions: 3h CPE, 0.5 mM **1**, 0.5 M $TBAPF_6$, CO_2, dry DMF. Working electrode: 2 cm^2 glassy carbon plate; counter electrode: platinum grid; reference electrode: SCE.

Although selectivity towards CO formation and TON increased with increasing acidity of the weak Brønsted acid, and the overpotential remains rather low (390 mV),[34,54] the overall faradaic efficiency did not overpass 50 % in any case (Table 1). Besides analyzing the gas space, after each CPE we analyzed the liquid phase by GC–MS, ionic chromatography, and NMR with different solvents (including DCl 37% in D_2O) without detecting other products arising from CO_2 reduction, solvent or supporting electrolyte degradation. Studies under CO atmosphere indicate electrocatalytic activity inhibition of **1** (Figure S49). Thus, considering that electrocatalytic inhibition could arise from CO binding to cobalt centers, we performed electrochemistry experiments under irradiation with 60 blue LED lamps (470 nm),[55] keeping the temperature of the cell controlled at 20 ºC. These attempts did not improve the faradaic efficiency of the catalysis (Table S12), neither experiments performed at higher temperature (Table S9).

From our studies we propose that during the electrocatalytic reduction of CO_2, both Co centers participate independently from each other, as two separate metal centers attached to a same ligand platform. For reactions taking place in DMF in the presence of Brønsted acids, in a first stage a two–electron reduction generates the monocationic complex $\mathbf{Co_2^+}$ (Scheme 2). Intermediate $\mathbf{Co_2^+}$ gets further reduced to generate the neutral complex intermediate, $\mathbf{Co_2}$, which will later undergo CO conversion from CO_2 in the presence of protons and electrons. After each catalytic cycle the complex is recovered, as reversibility of the redox event is observed after the catalytic cathodic curve by CV studies (Figure 6) and CPEs performed for 1 h in the presence of TFE (*vide supra*). Considering a single–site reactivity for the chemical transformation of CO_2, we assume that me mechanism proceeds similarly to previous reports.[32,34]

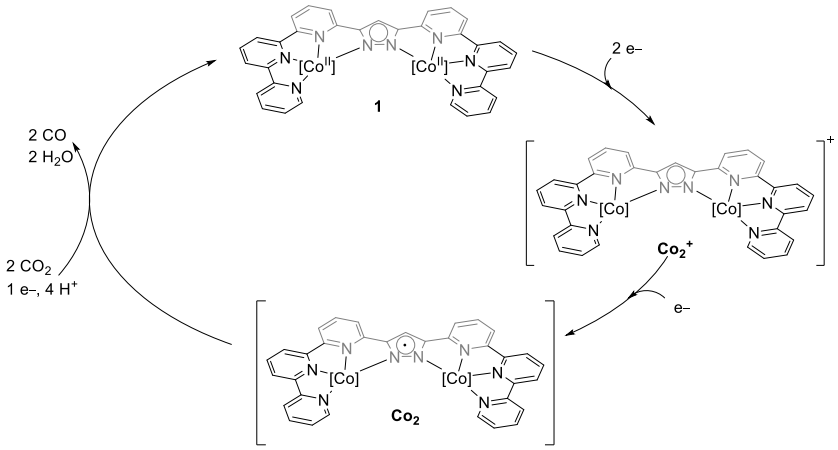

Scheme 2. Proposed mechanism for the conversion of CO_2 into CO by complex **1** in the presence of Brønsted acids.

Conclusion

We have described the synthesis of a new pyrazole–based ligand and formed a dinuclear cobalt (**1**) and zinc (**2**) complexes. Chemical, electrochemical and UV–vis–SEC studies of **1** confirmed a first 2 electron reduction process followed by 1 electron ligand–centered reduction. From IR–SEC studies and electrocatalytic reduction of CO_2 in the presence of Brønsted acids to generate CO, single–site reactivity

seems to occur with no cooperativity between metals. From electrocatalytic studies in the presence of different weak acids, the highest TONs (17) and selectivity (94%) where obtained when 1.47 M TFE were present, at –1.35 V *vs* SCE in DMF (0.39 V overpotential). As observed in previous works,[32,34] the participation of the ligand framework containing terpyridine groups may facilitate the reduction of the overpotential. The low FEs obtained (<50%) can be attributed to the formation of CO–containing cobalt complexes during the electrocatalytic process, which inhibit the reduction of CO_2, or secondary reactions with partial decomposition. Electrocatalytic studies of supported complex **1** over modified cathodes are currently under investigation to analyse their electrocatalytic performance in flow-cell electrolysers to avoid the accumulation of CO–containing cobalt species.

Experimental Section

General specifications

All manipulations unless stated otherwise were performed using Schlenk or glovebox techniques under dry argon or nitrogen atmosphere, respectively. THF was dried over Na/benzophenone, freshly distilled prior to use and stored under nitrogen atmosphere over molecular sieves (4Å). Anhydrous deuterated solvents were purchased from Eurisotop and stored over 4Å molecular sieves. All chemicals unless noted otherwise were purchased from major commercial suppliers (TCI, Sigma–Aldrich, Across Organics) and used as received.

Cyclic voltammetry

The electrochemical experiments were performed under argon flow in a three−electrode cell. The working electrode was a steady glassy carbon electrode of approximately 0.07 cm^2 surface area, the counter electrode was a platinum wire, and the reference was a saturated calomel electrode separated from the solution by a bridge. The cyclic voltammograms (CVs) were recorded in dry *N*,*N*−dimethylformamide (DMF) and CH_3CN from Across Organics, using an AUTOLAB (Metrohm) PGSTAT100N potentiostat run with Nova

2.1.4 software. The electrolyte salt, tetrabutylammonium hexafluorophosphate ($TBAPF_6$) for electrochemical analysis, was purchased from Sigma−Aldrich and all the glassware was carefully dried before use.

Controlled Potential Electrolysis

Controlled potential electrolysis were conducted using a PARSTAT 4000A potentiostat (Princeton Applied Research). Preparative scale controlled potential electrolysis (CPE) experiments were performed in an electrolysis cell with a working compartment (4 mL liquid volume) and counter compartment (2 mL liquid volume) separated by an ultrafine glass frit, the total volume of the sealed cell is 39 mL, all CPEs were performed at +20 °C. A 2 cm² glassy carbon plate was used as the working electrode, a platinum grid was used as the auxiliary electrode, and a Saturated Calomel Electrode in a tipped glass tube filled with electrolyte ($TBAPF_6$, 0.5 M in DMF or CH_3CN) was used as a reference electrode. Both compartments were sealed to be gastight. A second glassy carbon electrode (0.03 cm² area) was added in the working compartment to perform CV scan before and after the CPE measurement. The working compartment was sparged with CO_2 for 10 min before adding the solutions. The electrolyte solution was constantly stirred during the CPE experiment with a 1 cm stirring bar. No iR compensation was applied. The electrolysis experiments were then conducted at constant potential for the specified amount of time. After this period, the headspace of the cell was immediately analyzed by gas chromatography (GC).

Gas detection

GC analyses of gas sampled from the headspace during the electrolysis were performed with an Agilent Technologies 7820A GC system equipped with a thermal conductivity detector. CO and H_2 production was quantitatively detected using a CP–CarboPlot P7 capillary column (27.46 m in length and 25 μm internal diameter). Temperature was held at 150 °C for the detector and 34 °C for the oven. The carrier gas was argon flowing at 9.5 mL/min at constant pressure of 0.4 bars. Injection was performed via a 250–μL gas–tight (Hamilton) syringe previously degassed with CO_2. Conditions allowed detection of both H_2, O_2, N_2,

CO, and CO_2. Calibration curves for H_2 and CO were determined separately by injecting known quantities of pure gas. Detection limits for CO and H_2 are $5.2 \cdot 10^{-10}$ mol and $1.6 \cdot 10^{-10}$ mol, respectively.

UV–visible spectroelectrochemistry

This technique allows the *in situ* UV−vis characterization of intermediate species that are produced in the diffusion layer of an electrode. To do so, it is necessary to use a special cell, to which can be integrated three electrodes of the classical CV set−up, and that can be at the same time mounted in the spectrophotometer. The electrochemical cell is mounted in a special transparent Dewar−type support inside the spectrophotometer. The former consists of a 0.2 cm quartz UV−vis−NIR cell surmounted by a glass compartment. The Dewar was cooled, if needed, by a Julabo circulation cryostat. In this case, all experiments were conducted at 20 °C. We used the same set−up as previously described,[56,57] using a Toray carbon paper as working electrode with holes that allow light to pass through, connected with golden thread. This carbon material has a behavior much closer to the GC electrode than platinum, so the CV analysis can be directly correlated with the results in the spectroelectrochemical experiment. The reference electrode is a carbon/Teflon pseudoreference that is very stable for several hours, avoiding Ag^+ leaks in the solution that can be detrimental for electrochemistry experiments. Finally, a thin GC electrode has been integrated in the set−up, allowing the recording of CVs inside the cell. As a counter electrode, we use a platinum grid protected in a glass frit (SI, Figure S1). Absorbance spectra were collected using an Agilent Cary 60 UV–vis instrument.

Infrared spectroelectrochemistry

An optically transparent thin–layer electrode (OTTLE) cell, equipped with a CaF_2 window, Pt minigrid as working electrode, Pt microwire as counter electrode, and Ag microwire as a pseudo–reference electrode. For studies performed under CO_2 atmposphere, the blank solutions consist on the solution of **1** (6 mM) in DMF (0.5 M $TBAPF_6$) which later was used to substract the solvent signals. For experiments under CO

atmosphere, the blank solutions was only electrolyte solution used to perform solvent subtractions. FT–IR spectra were measured using Perkin–Elmer FT–IR spectrometer.

NMR spectrometry

NMR spectra were measured on a Bruker Avance II 400 MHz spectrometer. The following abbreviations are used for describing NMR spectra: s (singlet), d (doublet), t (triplet), td (triplet of doublets), ddd (doublet of doublets of doublets), vd (virtual doublet), vt (virtual triplet), br (broad). Chemical shifts (δ_H, δ_C) were quoted in parts per million (ppm) and were referenced to the residual solvent peak.

Electrospray Ionization Mass Spectrometry (ESI–MS)

The samples were solubilized in methanol or MeCN and then injected in direct introduction (infusion) in the mass spectrometer. A Bruker mass spectrometer, model micrOTOF−Q II was used with an electrospray source (ESI).

X−Ray crystallography

The data for **1** were collected at 100(2) K on a Bruker D8 Quest diffractometer equipped with an Incoatec Microfocus Source (IμS 3.0 Mo) and a PHOTON III area detector, and operated through the APEX3 software.[58] The data were processed with SAINT[59] and absorption effects were corrected for empirically with SADABS.[60,61] The structure was solved by intrinsic phasing with SHELXT[62] and refined by full−matrix least−squares on F^2 with SHELXL,[63] using the ShelXle interface.[64] All non−hydrogen atoms were refined with anisotropic displacement parameters. The hydrogen atoms were introduced at calculated positions and were treated as riding atoms with an isotropic displacement parameter equal to 1.2 times that of the parent atom (1.5 for CH_3). The molecular plot was drawn with ORTEP−3.[65]

Acknowledgements

The authors greatly acknowledge the financial support from the *Investissement l'Avenir*, specifically through the *MOPGA* call Nº ANR–18–MPGA–0012.

Keywords: Bimetallic • Electrocatalysis • Carbon Dioxide • Spectro–electrochemistry • Cobalt

References

[1] The Intergovernmental Panel on Climate Change., **2021**.
[2] Make Our Planet Great Again, is an initiative of the President of the Republic of France Emmanuel Macron, Launched on 1st June 2017 following the decision of the United States to leave the Paris Agreement on the climate, **2017**.
[3] T. R. Cook, D. K. Dogutan, S. Y. Reece, Y. Surendranath, T. S. Teets, D. G. Nocera, *Chem. Rev.* **2010**, *110*, 6474–6502.
[4] J. H. Clark, T. J. Farmer, L. Herrero-Davila, J. Sherwood, *Green Chem.* **2016**, *18*, 3914–3934.
[5] A. Talaei, Md. Ahiduzzaman, A. Kumar, *Energy* **2018**, *153*, 231–247.
[6] J.-M. Savéant, *Chem. Rev.* **2008**, *108*, 2348–2378.
[7] N. W. Kinzel, C. Werlé, W. Leitner, *Angew. Chem. Int. Ed.* **2021**, *60*, 11628–11686.
[8] N. Wolff, O. Rivada-Wheelaghan, D. Tocqueville, *ChemElectroChem* **2021**, celc.202100617.
[9] P. De Luna, C. Hahn, D. Higgins, S. A. Jaffer, T. F. Jaramillo, E. H. Sargent, *Science* **2019**, *364*, eaav3506.
[10] Y. Kawamata, P. S. Baran, *Joule* **2020**, *4*, 701–704.
[11] C. Kingston, M. D. Palkowitz, Y. Takahira, J. C. Vantourout, B. K. Peters, Y. Kawamata, P. S. Baran, *Acc. Chem. Res.* **2020**, *53*, 72–83.
[12] K. E. Dalle, J. Warnan, J. J. Leung, B. Reuillard, I. S. Karmel, E. Reisner, *Chem. Rev.* **2019**, *119*, 2752–2875.
[13] Y. Zhao, G. Yu, F. Wang, P. Wei, J. Liu, *Chem. Eur. J.* **2019**, *25*, 3726–3739.
[14] Q. J. Bruch, G. P. Connor, N. D. McMillion, A. S. Goldman, F. Hasanayn, P. L. Holland, A. J. M. Miller, *ACS Catal.* **2020**, *10*, 10826–10846.
[15] X.-J. Su, M. Gao, L. Jiao, R.-Z. Liao, P. E. M. Siegbahn, J.-P. Cheng, M.-T. Zhang, *Angew. Chem. Int. Ed.* **2015**, *54*, 4909–4914.
[16] G. Passard, A. M. Ullman, C. N. Brodsky, D. G. Nocera, *J. Am. Chem. Soc.* **2016**, *138*, 2925–2928.
[17] C. Di Giovanni, C. Gimbert-Suriñach, M. Nippe, J. Benet-Buchholz, J. R. Long, X. Sala, A. Llobet, *Chem. Eur. J.* **2016**, *22*, 361–369.
[18] B. M. Lindley, R. S. van Alten, M. Finger, F. Schendzielorz, C. Würtele, A. J. M. Miller, I. Siewert, S. Schneider, *J. Am. Chem. Soc.* **2018**, *140*, 7922–7935.
[19] H. Chen, L. Chen, G. Chen, M. Robert, T. Lau, *ChemPhysChem* **2021**, cphc.202100330.
[20] C.-H. Wang, S. DeBeer, *Chem. Soc. Rev.* **2021**, *50*, 8743–8761.
[21] A. L. Gavrilova, B. Bosnich, *Chem. Rev.* **2004**, *104*, 349–384.
[22] I. G. Powers, C. Uyeda, *ACS Catal.* **2017**, *7*, 936–958.
[23] M. E. Ahmed, S. Adam, D. Saha, J. Fize, V. Artero, A. Dey, C. Duboc, *ACS Energy Lett.* **2020**, *5*, 3837–3842.

[24] R. Angamuthu, P. Byers, M. Lutz, A. L. Spek, E. Bouwman, *Science* **2010**, *327*, 313–315.
[25] W. Yang, S. Sinha Roy, W. C. Pitts, R. L. Nelson, F. R. Fronczek, J. W. Jurss, *Inorg. Chem.* **2018**, *57*, 9564–9575.
[26] S. Trofimenko, in *Progress in Inorganic Chemistry*, John Wiley & Sons, Ltd, **1986**, pp. 115–210.
[27] J. Klingele, S. Dechert, F. Meyer, *Coordination Chemistry Reviews* **2009**, *253*, 2698–2741.
[28] A. Srinivasan, J. Campos, N. Giraud, M. Robert, O. Rivada-Wheelaghan, *Dalton Trans.* **2020**, *49*, 16623–16626.
[29] E. Boutin, L. Merakeb, B. Ma, B. Boudy, M. Wang, J. Bonin, E. Anxolabéhère-Mallart, M. Robert, *Chem. Soc. Rev.* **2020**, *49*, 5772–5809.
[30] A. Brinkmeier, K. E. Dalle, L. D'Amore, R. A. Schulz, S. Dechert, S. Demeshko, M. Swart, F. Meyer, *J. Am. Chem. Soc.* **2021**, DOI 10.1021/jacs.1c08645.
[31] J. S. Derrick, M. Loipersberger, R. Chatterjee, D. A. Iovan, P. T. Smith, K. Chakarawet, J. Yano, J. R. Long, M. Head-Gordon, C. J. Chang, *J. Am. Chem. Soc.* **2020**, *142*, 20489–20501.
[32] M. Loipersberger, D. G. A. Cabral, D. B. K. Chu, M. Head-Gordon, *J. Am. Chem. Soc.* **2021**, *143*, 744–763.
[33] S. Hooe, J. Moreno, D. Dickie, C. Machan, **2021**, DOI 10.33774/chemrxiv-2021-lplvt.
[34] C. Cometto, L. Chen, P.-K. Lo, Z. Guo, K.-C. Lau, E. Anxolabéhère-Mallart, C. Fave, T.-C. Lau, M. Robert, *ACS Catal.* **2018**, *8*, 3411–3417.
[35] C. Cometto, L. Chen, E. Anxolabéhère-Mallart, C. Fave, T.-C. Lau, M. Robert, *Organometallics* **2019**, *38*, 1280–1285.
[36] L. Chen, G. Chen, C.-F. Leung, C. Cometto, M. Robert, T.-C. Lau, *Chem. Soc. Rev.* **2020**, *49*, 7271–7283.
[37] J. Pons, X. López, E. Benet, J. Casabó, F. Teixidor, F. J. Sánchez, *Polyhedron* **1990**, *9*, 2839–2845.
[38] D. H. Grant, *J. Chem. Educ.* **1995**, *72*, 39.
[39] S. I. G. Dias, A. I. S. Neves, S. Rabaça, I. C. Santos, M. Almeida, *Eur. J. Inorg. Chem.* **2008**, *2008*, 4728–4734.
[40] S. Alvarez, *Chem. Rev.* **2015**, *115*, 13447–13483.
[41] S. Mandal, S. Shikano, Y. Yamada, Y.-M. Lee, W. Nam, A. Llobet, S. Fukuzumi, *J. Am. Chem. Soc.* **2013**, *135*, 15294–15297.
[42] C. Amatore, M. Azzabi, P. Calas, A. Jutand, C. Lefrou, Y. Rollin, *Journal of Electroanalytical Chemistry and Interfacial Electrochemistry* **1990**, *288*, 45–63.
[43] A. J. Bard, L. R. Faulkner, *Electrochemical Methods: Fundamentals and Applications, 2nd Edition*, Willey, **2001**.
[44] A. J. Bard, E. Garcia, S. Kukharenko, V. V. Strelets, *Inorg. Chem.* **1993**, *32*, 3528–3531.
[45] M. M. MacInnes, S. Hlynchuk, S. Acharya, N. Lehnert, S. Maldonado, *ACS Appl. Mater. Interfaces* **2018**, *10*, 2004–2015.
[46] D. A. Kurtz, D. Dhar, N. Elgrishi, B. Kandemir, S. F. McWilliams, W. C. Howland, C.-H. Chen, J. L. Dempsey, *J. Am. Chem. Soc.* **2021**, *143*, 3393–3406.
[47] Although, the electrochemical and electrocatalytic studies of complex 1 were performed in MeCN and DMF solutions. Due to non-diffusive effects and electrochemical adsoroption at the electrode surface when MeCN was used. The studies in MeCN solution have been located at the supporting information without further description., **n.d.**
[48] I. Bhugun, D. Lexa, J.-M. Savéant, *J. Am. Chem. Soc.* **1996**, *118*, 1769–1776.

[49] C. Costentin, S. Drouet, G. Passard, M. Robert, J.-M. Savéant, *J. Am. Chem. Soc.* **2013**, *135*, 9023–9031.
[50] J.-M. Savéant, C. Costentin, *Elements of Molecular and Biomolecular Electrochemistry: An Electrochemical Approach to Electron Transfer Chemistry*, Willey, **2019**.
[51] K. J. Lee, B. D. McCarthy, J. L. Dempsey, *Chem. Soc. Rev.* **2019**, *48*, 2927–2945.
[52] R. Francke, B. Schille, M. Roemelt, *Chem. Rev.* **2018**, *118*, 4631–4701.
[53] J. R. McKone, S. C. Marinescu, B. S. Brunschwig, J. R. Winkler, H. B. Gray, *Chem. Sci.* **2014**, *5*, 865–878.
[54] I. Azcarate, C. Costentin, M. Robert, J.-M. Savéant, *J. Am. Chem. Soc.* **2016**, *138*, 16639–16644.
[55] J. Lloret-Fillol, S. L. Fernández, S. Cañellas, F. Franco, J. M. Luis, M. À. Pericàs, *ChemElectroChem* **n.d.**, *n/a*, DOI 10.1002/celc.202100859.
[56] N. Kostopoulos, F. Banse, C. Fave, E. Anxolabéhère-Mallart, *Chem. Commun.* **2021**, *57*, 1198–1201.
[57] N. Kostopoulos, C. Achaibou, J.-M. Noël, F. Kanoufi, M. Robert, C. Fave, E. Anxolabéhère-Mallart, *Inorg. Chem.* **2020**, *59*, 11577–11583.
[58] Bruker AXS, *Bruker AXS. APEX3. Version 2019.1−0. Madison, Wisconsin, USA, 2019.*, **n.d.**
[59] *Bruker Nano, Inc. SAINT. Version 8.40A. Madison, Wisconsin, USA, 2019*, **n.d.**
[60] *Bruker AXS. SADABS. Version 2016/2. Madison, Wisconsin, USA, 2016*, **n.d.**
[61] L. Krause, R. Herbst-Irmer, G. M. Sheldrick, D. Stalke, *J Appl Cryst* **2015**, *48*, 3–10.
[62] G. M. Sheldrick, *Acta Cryst A* **2015**, *71*, 3–8.
[63] G. M. Sheldrick, *Acta Cryst C* **2015**, *71*, 3–8.
[64] C. B. Hübschle, G. M. Sheldrick, B. Dittrich, *J Appl Cryst* **2011**, *44*, 1281–1284.
[65] L. J. Farrugia, *J Appl Cryst* **2012**, *45*, 849–854.

Supporting Information

Electrocatalytic CO_2 reduction with a binuclear cobalt complex

Antoine Bohn,[a] Juan José Moreno,[b] Pierre Thuéry,[c] Marc Robert,[a,d] and Orestes Rivada–Wheelaghan*[a]

[a] Dr. A. Bohn, Prof. M. Robert and Dr. O. Rivada–Wheelaghan
Laboratoire d'Electrochimie Moléculaire (LEM)
Université de Paris, CNRS
F–75006 Paris, France
E–mail: orestes.rivada@u–paris.fr

[b] Dr. J. J. Moreno
Instituto de Investigaciones Químicas (IIQ), Departamento de Química Inorgánica and Centro de Innovación en Química Avanzada (ORFEO–CINQA)
Consejo Superior de Investigaciones Científicas (CSIC) and University of Sevilla
Avenida Américo Vespucio 49, 41092 Sevilla (Spain)

[c] Dr. P. Thuéry
NIMBE
Université Paris–Saclay, CEA, CNRS,
91191 Gif–sur–Yvette, France.

[d] Prof. M. Robert
Institut Universitaire de France (IUF)
F–75005 Paris, France.

Table of contents

1 Experimental details 4
1.1 Materials 4
1.2 Chemicals 4
2 Synthesis and characterization 5
2.1 3,5–bis{6–(2,2':6',2''–terpyridine)}pyrazole, L–H 5
2.1.1 General procedure 5
2.1.2 6–Methyl–2,2':6',2''–terpyridine carboxylate, D 5
2.1.3 6–Acetyl 2,2':6',2''–terpyridine, E 9
2.1.4 3,5-bis{6-(2,2':6',2''-terpyridine)}pyrazole (L-H) 12
2.2 Complex $[Co^{II}_2(L)(CH_3CN)_4][BF_4]_3$ (1) 15
2.2.1 General procedure 15
2.2.2 X–Ray diffraction structure 16
2.2.3 ESI–MS 17
2.2.4 UV–vis spectroscopy 18
2.2.5 Measurement of magnetic moment by the Evans method 18
2.2.6 Nuclear magnetic resonance 20
2.3 Complex $[Zn_2(L)(OTf)_3(CH_3CN)]$ (2) 21
2.3.1 General procedure 21
2.3.2 Nuclear Magnetic Resonnance 21
3 Electrochemical studies of complex 1 under argon 25
3.1 Study in CH_3CN 25
3.1.1 Comparison with $[Zn^{II}_2(L)(CH_3CN)_4][OTf]_3$ (2) 31
3.2 Study in DMF 32
3.2.1 Comparison with $[Zn^{II}_2(L)(CH_3CN)_4][OTf]_3$ (2) 36
4 *In–situ* characterization of complex $[Co^{I}_2(L)](BF_4)$ (3) 37
4.1.1 UV–vis spectro–electrochemical analysis. Electroreduction of complex 1. 37
4.1.2 UV–vis analysis through chemical reduction of complex 1. 39
5 Electrochemical study of complex 1 under CO_2 40
5.1 In CH_3CN 40
5.2 In DMF 41
5.2.1 By cyclic voltammetry 41
5.2.2 By FT–IR−SpectroElectroChemistry (SEC) 41
6 Study of complex 1 under CO 44
6.1 In CH_3CN 44
6.1.1 By cyclic voltammetry 44

6.2 In DMF 45
6.2.1 By cyclic voltammetry 45
6.2.2 By FT–IR−SpectroElectroChemistry (SEC) 48
7 Effect of a proton source under CO_2 atmosphere 49
7.1 In CH_3CN 49
7.1.1 Effect of water as a proton source 49
7.1.2 Effect of phenol as a proton source 50
7.1.3 Effect of 2,2,2–Trifluoroethanol as a proton source 50
7.2 In DMF 51
7.2.1 Effect of water as a proton source 51
7.2.2 Effect of phenol as a proton source 52
7.2.3 Effect of 2,2,2–Trifluoroethanol as a proton source 53
8 Controlled Potential Electrolyses (CPE) 55
8.1 CPE under CO_2 55
8.2 CPE under CO_2 in the presence of water 56
8.3 CPE under CO_2 in the presence of phenol 58
8.4 CPE under CO_2 in the presence of phenol and CF_3CH_2OH at the second cathodic wave 60
8.5 CPE under CO_2 in the presence of 2,2,2–Trifluoroethanol 61
8.5.1 Comparison CH_3CN/DMF 61
8.5.2 CPE in DMF: use of labelled $^{13}CO_2$ and without catalyst (blank) 63
8.5.3 CPE in DMF: variation of the temperature 63
8.5.4 CPE in DMF: change in the quantity of catalyst 65
8.5.5 CPE in DMF: change in duration 66
8.5.6 CPE in DMF: influence of a source of light 67
8.5.7 CPE in DMF: activity of $CoCl_2$ and L–H 69
9 References 73

1 Experimental details

1.1 Materials

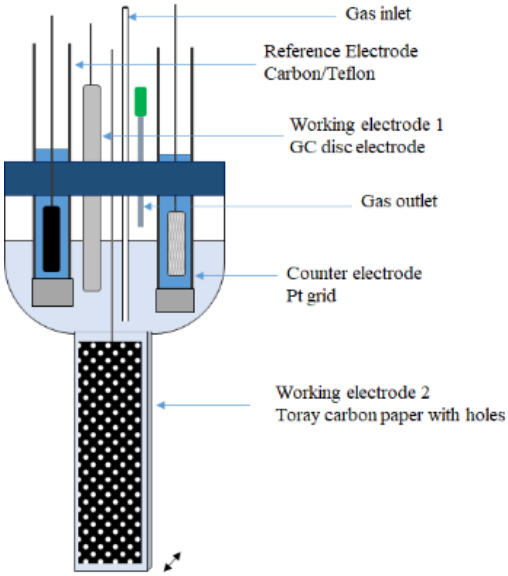

Figure S1. UV–vis SEC cell used for this study.

Figure S2. Picture of IR SEC cell.

1.2 Chemicals

Unless otherwise noted, reagents and solvents were purchased from commercial suppliers (TCI, Sigma–Aldrich or Acros Organics) and used without further purification.

2 Synthesis and characterization

2.1 3,5–bis{6–(2,2':6',2''–terpyridine)}pyrazole, L–H

2.1.1 General procedure

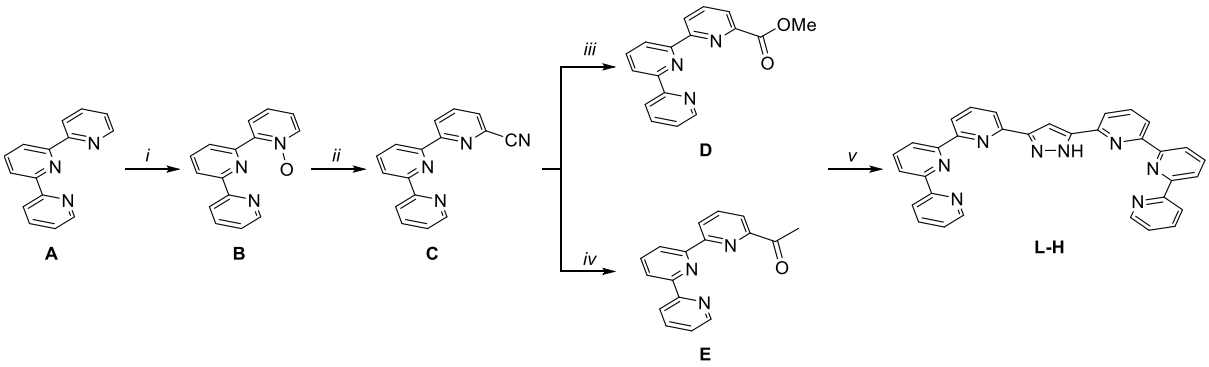

Scheme 1. Synthesis of ligand **L–H**. *i*, formation of N–oxide (B);[1] *ii*, carbonitrile formation (C);[1] *iii*, ester formation (**D**);[2] *iv*, ketone formation (**E**);[2] *v*, pyrazole ring formation (**L–H**).[2]

Compounds **B** and **C** were synthesized following reported procedures starting from commercially available terpyridine (**A**).[1] Compounds **D** and **E** were synthesized from slight modified reported procedure.[2] Inside the glovebox, 50 mg of Na (2.1 mmol) were put to react in CH_3OH (12 mL). Due to the exothermic nature of the reaction, Na was added cautiously to cold CH_3OH. Once Na had dissolved, 240 mg of **C** were added (0.9 mmol) and the reaction was left stirring for 24h. Compound **D** was obtained pure after work up obtaining comparable yield values to previous reports.[2] Synthesis of compound **E** was always obtained with lower yields than previous reports (<50%).[2] To a solution of **C** (1.65 g, 6.37 mmol) in dry THF (20 mL) MeMgBr (3.0 M in Et_2O, 2.8 mL, 1.3 equiv, 8.29 mmol) was added dropwise at—20 °C. The reaction mixture was further stirred for 1 h at –20 °C and then for 2 h at room temperature to give an orange solution. Slow addition of a saturated NH_4Cl solution (20 mL) was followed by phase separation. The aqueous phase was extracted with THF (20 mL) and then CH_2Cl_2 (20 mL). The combined organic phases were washed with saturated NaCl (20 mL) and H_2O (20 mL) and then dried over $MgSO_4$. Evaporation of the filtrate in vacuo left an oil which was purified by column chromatography on silica gel, eluting a mixture of pentane–ethyl acetate (3:1) yielding **E** pure. Once **D** and **E** were obtained pure, ligand **L–H** was synthesized following reported procedures.[2]

2.1.2 6–Methyl–2,2':6',2''–terpyridine carboxylate, D

^{1}H NMR (400 MHz, 20 ºC, $CDCl_3$): 8.82 (dd, $^3J_{H,H}$ = 7.9, $^4J_{H,H}$ = 1.1 Hz, 1H, CH), 8.75 – 8.68 (m, 1H, CH), 8.65 – 8.56 (m, 2H, 2 CH), 8.49 (dd, $^3J_{H,H}$ = 7.8, $^4J_{H,H}$ = 1.0 Hz, 1H, CH), 8.16 (dd, $^3J_{H,H}$ = 7.7, $^4J_{H,H}$ = 1.1 Hz, 1H, CH), 7.99 (m, 2H, 2 CH), 7.86 (td, $^3J_{H,H}$ = 7.7, $^4J_{H,H}$ = 1.8 Hz, 1H, CH), 7.34 (ddd, $^3J_{H,H}$ = 7.5, $^3J_{H,H}$ = 4.8, $^4J_{H,H}$ = 1.2 Hz, 1H, CH), 4.05 (s, 3H, OCH_3) ppm.

$^{13}C\{^{1}H\}$ NMR (101 MHz, 20 ºC, $CDCl_3$: 166.05 (C=O), 156.66 (C), 156.22 (C), 155.57 (C), 154.58 (C), 149.33 (CH_{ar}), 147.71 (C), 138.22 (CH_{ar}), 137.95 (CH_{ar}), 137.02 (CH_{ar}), 125.19 (CH_{ar}), 124.49 (CH_{ar}), 123.98 (CH_{ar}), 121.75 (CH_{ar}), 121.67 (CH_{ar}), 121.28 (CH_{ar}), 53.00 (OCH_3) ppm.

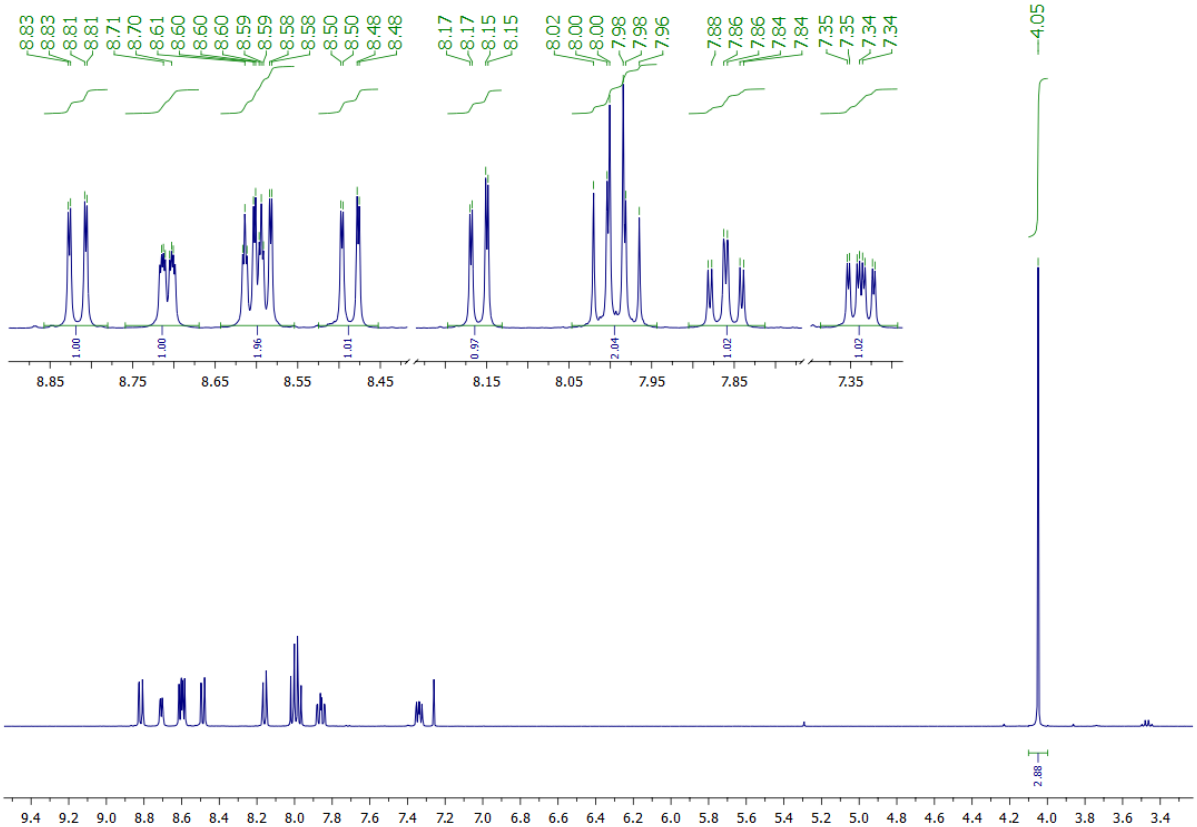

Figure S3. ^{1}H NMR spectrum (400 MHz) of **D** in $CDCl_3$ solution.

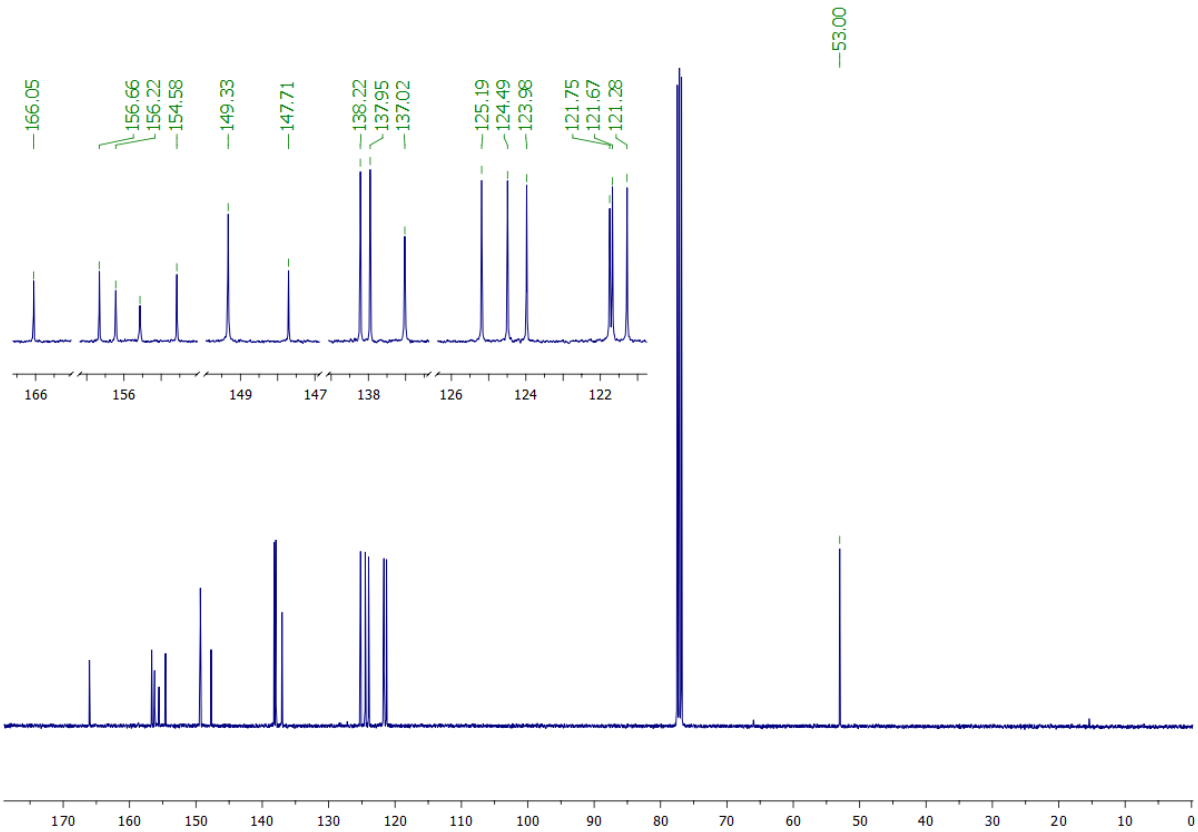

Figure S4. $^{13}C\{^{1}H\}$ spectrum (101 MHz) of **D** in $CDCl_3$ solution .

ESI-HRMS (m/z pos): Found (Calc): $C_{17}H_{13}N_3NaO_2^+$ 314.0901 (314.0905).

Experimental mass spectrum

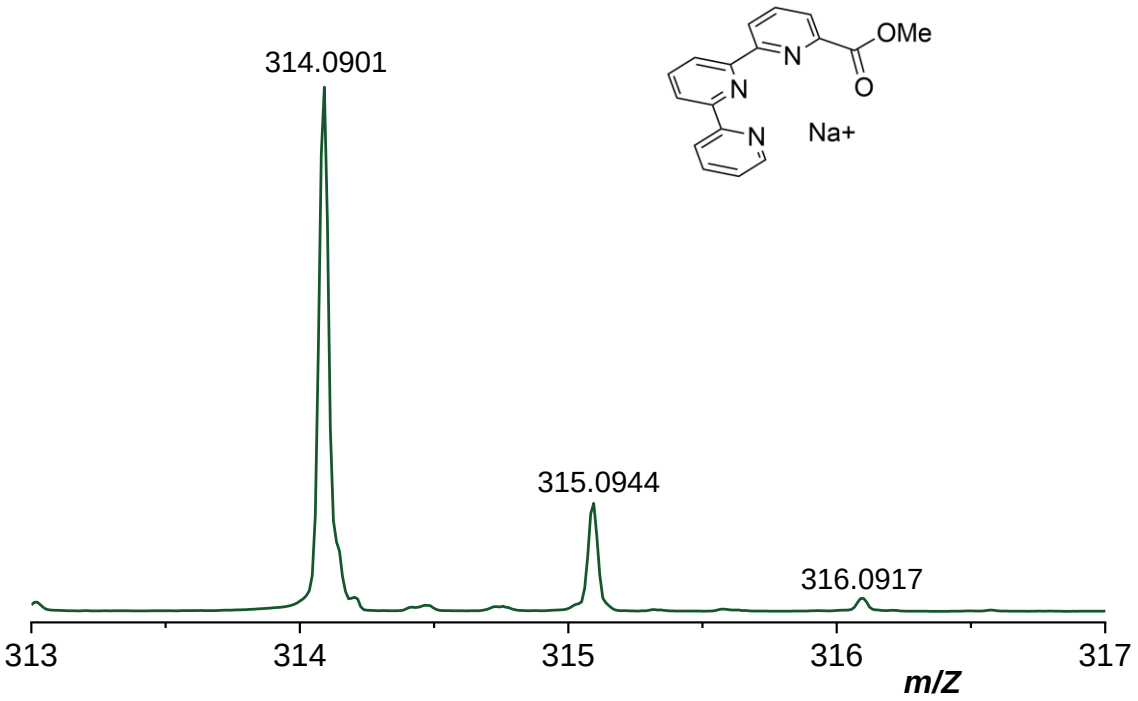

Simulated mass spectrum

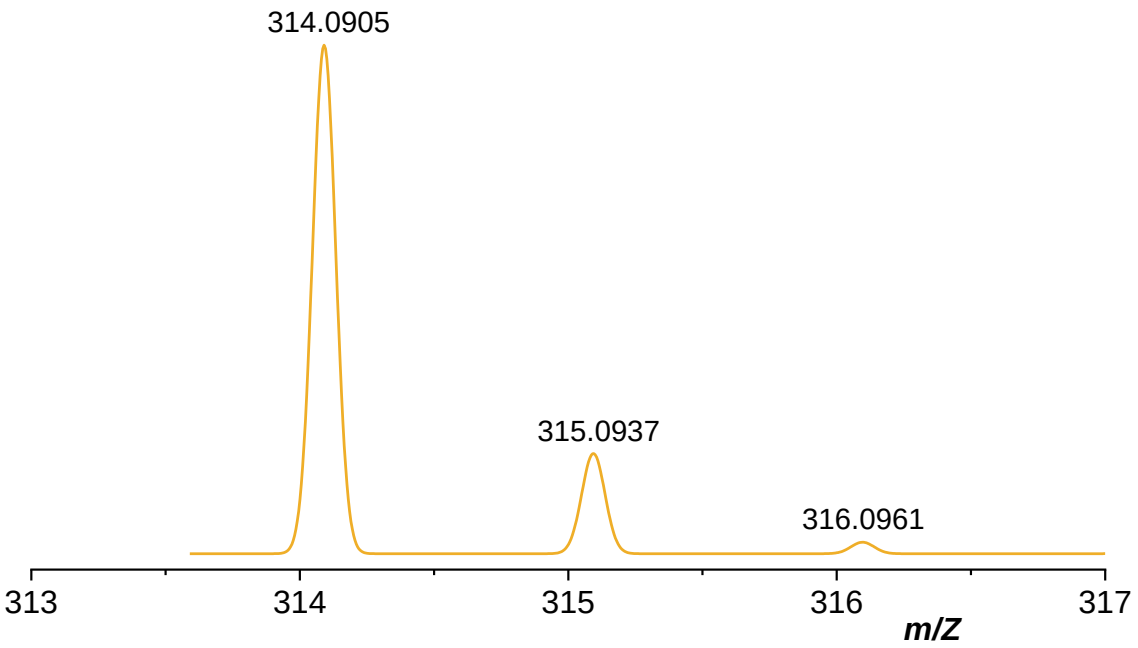

Figure S5. Experimental ESI–MS spectrum of 6–Methyl–2,2':6',2''–terpyridine carboxylate (**D**), (top) and simulated ESI–MS spectrum using mMass software (bottom).

2.1.3 6–Acetyl 2,2':6',2''–terpyridine, E

^{1}H NMR (400 MHz, 20 ºC, $CDCl_3$): 8.76 (dd, $^{3}J_{H,H}$ = 7.8, $^{4}J_{H,H}$ = 1.2 Hz, 1H, CH), 8.65 (ddd, $^{3}J_{H,H}$ = 4.8, $^{4}J_{H,H}$ = 1.8, $^{4}J_{H,H}$ = 0.9 Hz, 1H, CH), 8.56 (dt, $^{3}J_{H,H}$ = 8.0, $^{4}J_{H,H}$ = 1.1 Hz, 1H, CH), 8.51 (dd, $^{3}J_{H,H}$ = 7.8, $^{4}J_{H,H}$ = 1.1 Hz, 1H, CH), 8.43 (dd, $^{3}J_{H,H}$ = 7.8, $^{4}J_{H,H}$ = 1.0 Hz, 1H, CH), 8.02 (dd, $^{3}J_{H,H}$ = 7.7, $^{4}J_{H,H}$ = 1.2 Hz, 1H, CH), 7.93 (td, $^{3}J_{H,H}$ = 7.8, $^{4}J_{H,H}$ = 1.8 Hz, 2H, CH), 7.81 (td, $^{3}J_{H,H}$ = 7.7, $^{4}J_{H,H}$ = 1.8 Hz, 1H, CH), 7.28 (dd, $^{3}J_{H,H}$ = 7.42, $^{3}J_{H,H}$ = 4.71, $^{4}J_{H,H}$ = 1.10 Hz, 1H, CH), 2.80 (s, 3H, CH_3) ppm.

^{13}C{^{1}H} NMR (101 MHz, 20 ºC, $CDCl_3$) δ 200.4 (C=O), 156.0 (C), 155.5 (C), 154.6 (C), 152.9 (C), 149.2 (CH), 138.0 (CH), 137.8 (CH), 136.9 (CH), 124.4 (CH), 123.9 (CH), 121.5 (CH), 121.4 (CH), 121.2 (CH), 121.1 (CH), 25.8 (CH_3) ppm.

A quaternary carbon signal could not be reliably detected, which could be due to broadened signal or overlap.

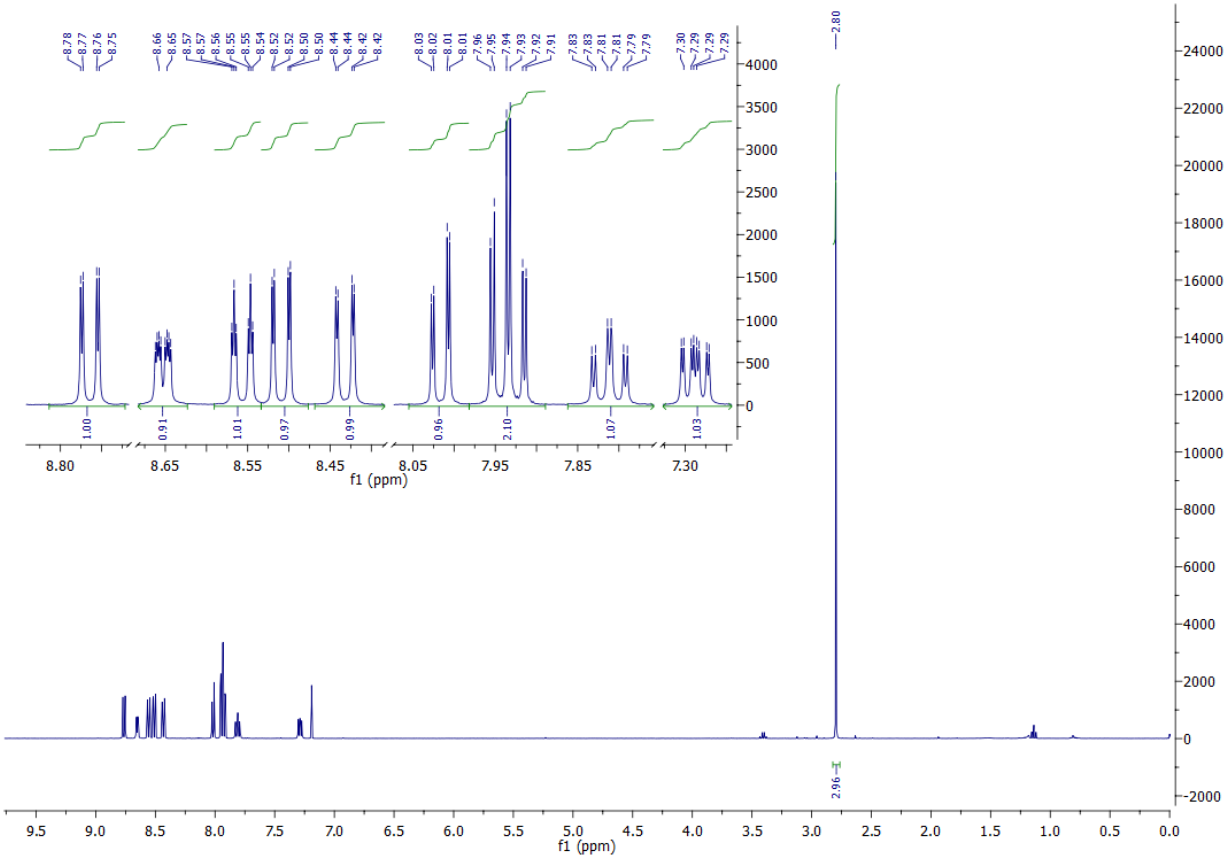

Figure S6. ^{1}H NMR spectrum (400 MHz) of **E** in $CDCl_3$ solution .

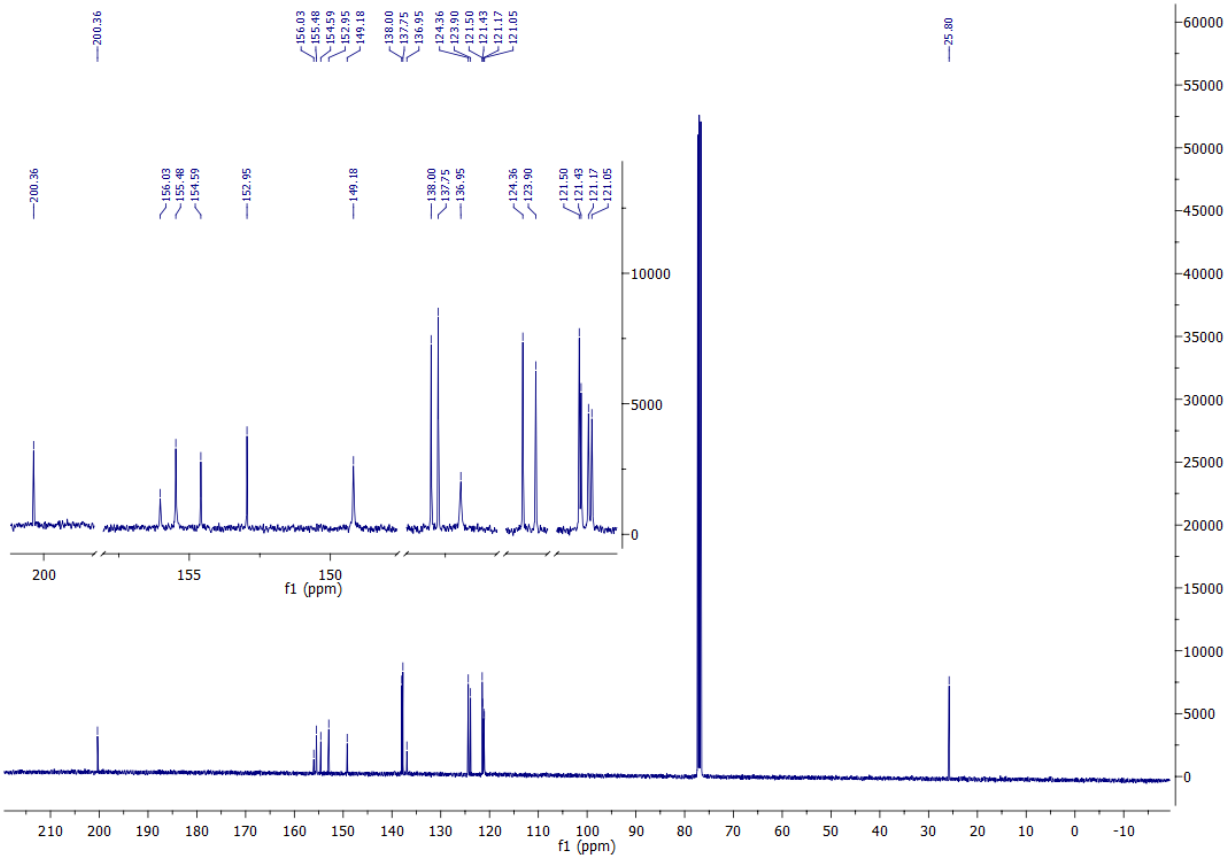

Figure S7. $^{13}C\{^{1}H\}$ spectrum (101 MHz) of **E** in $CDCl_3$ solution.

ESI-HRMS (m/z pos): Found (Calc): $C_{17}H_{13}N_3NaO^+$ 298.0919 (298.0956).

Experimental mass spectrum

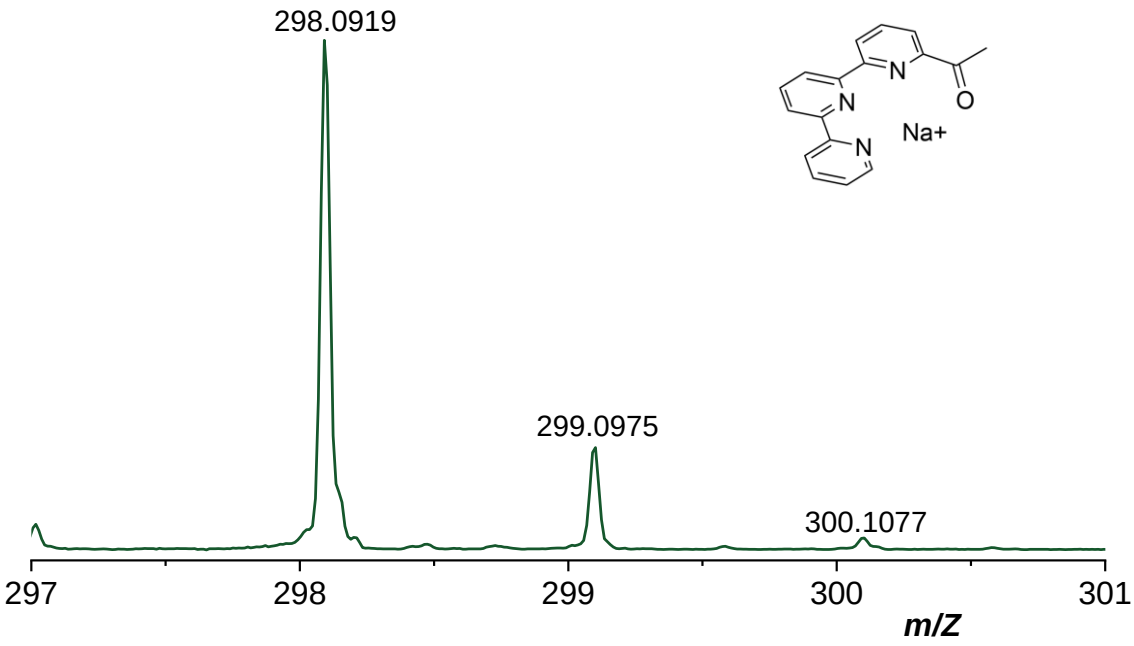

Simulated mass spectrum

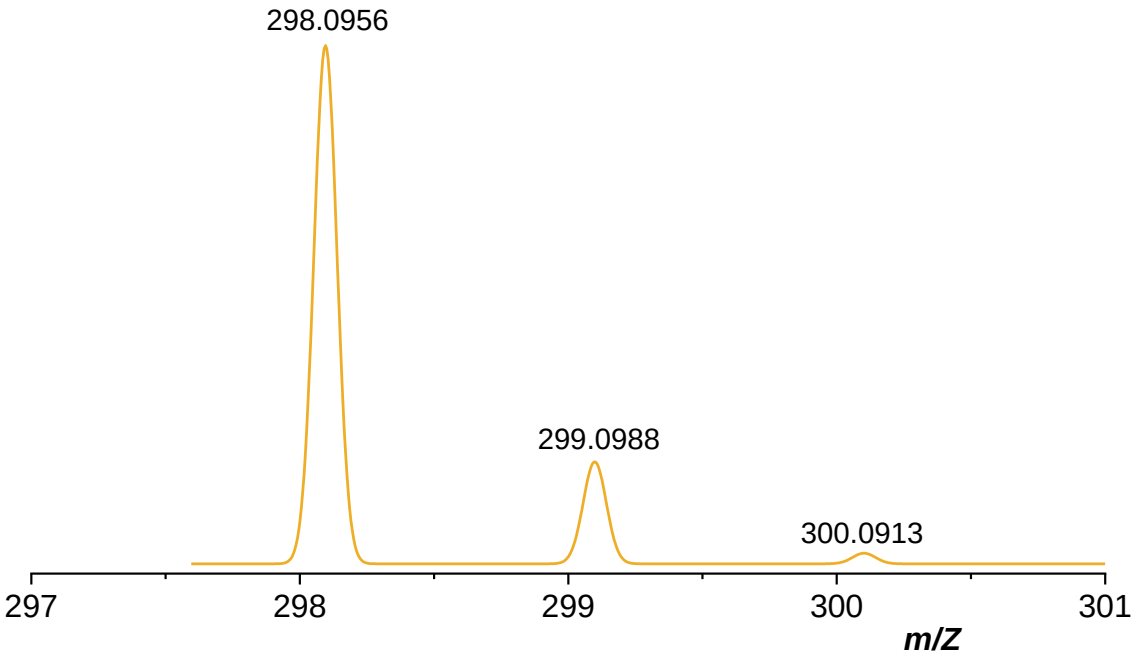

Figure S8. Experimental ESI–MS spectrum of 6–Acetyl 2,2':6',2''–terpyridine (**E**), (top) and simulated ESI–MS spectrum using mMass software (bottom).

2.1.4 3,5-bis{6-(2,2':6',2''-terpyridine)}pyrazole (L-H)

Nuclear Magnetic Resonance

^{1}H NMR (400 MHz, 20 ºC, DMSO–d$_6$): 8.90 (d, $^{3}J_{H,H}$ = 7.3 Hz, 2H), 8.75 (d, $^{3}J_{H,H}$ = 4.1 Hz, 2H), 8.68 (d, $^{3}J_{H,H}$ = 7.9 Hz, 2H), 8.62 (d, $^{3}J_{H,H}$ = 7.2 Hz, 2H), 8.51 (d, $^{3}J_{H,H}$ = 7.7 Hz, 2H), 8.16 (m, 6H), 8.04 (dt, $^{3}J_{H,H}$ = 10.9, 4.5 Hz, 2H), 7.84 (s, 1H), 7.52 (dd, $^{3}J_{H,H}$ = 6.7, 5.3 Hz, 2H) ppm.

^{13}C{^{1}H} NMR (101 MHz, 20 ºC, DMSO–d$_6$): 155.6, 155.2, 155.1, 149.8, 138.9, 138.9, 137.9, 124.9, 121.9, 121.3, 121.2, 120.7, 120.0, 103.1 ppm.

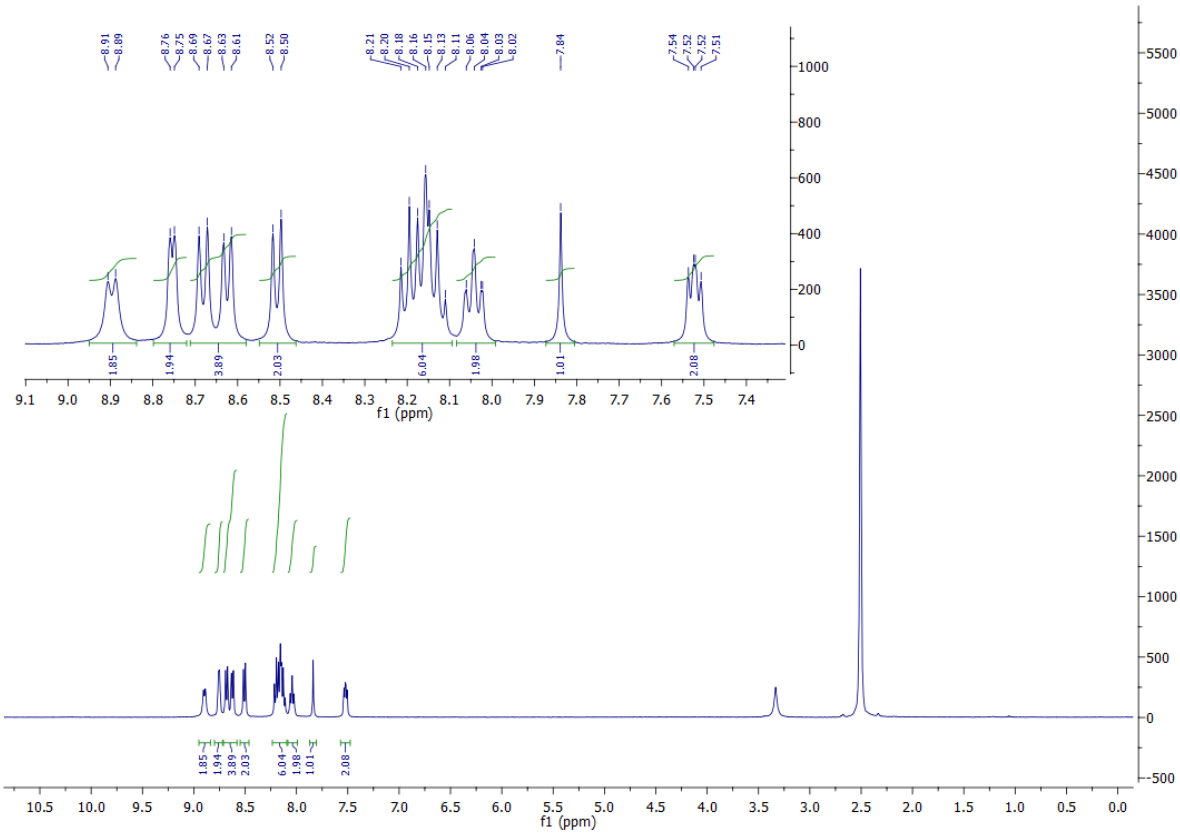

Figure S9. ^{1}H NMR spectrum (400 MHz) of ligand **L–H** in DMSO–d$_6$ solution.

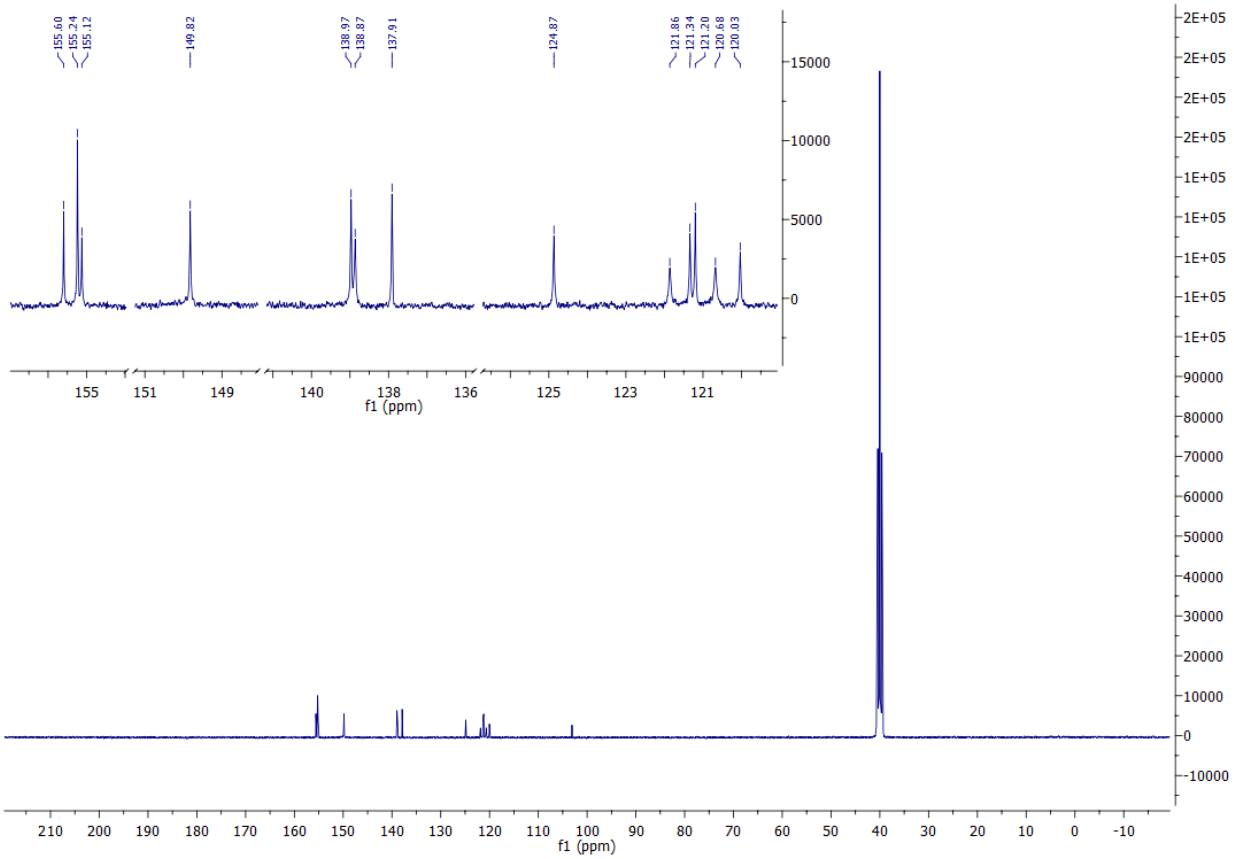

Figure S10. $^{13}C\{^{1}H\}$ spectrum (101 MHz) of **L–H** in DMSO–d_6 solution.

ESI–MS

ESI-HRMS (m/z pos): Found (Calc): $C_{33}H_{23}N_8^+$ 531.2014 (531.2046).

Experimental mass spectrum

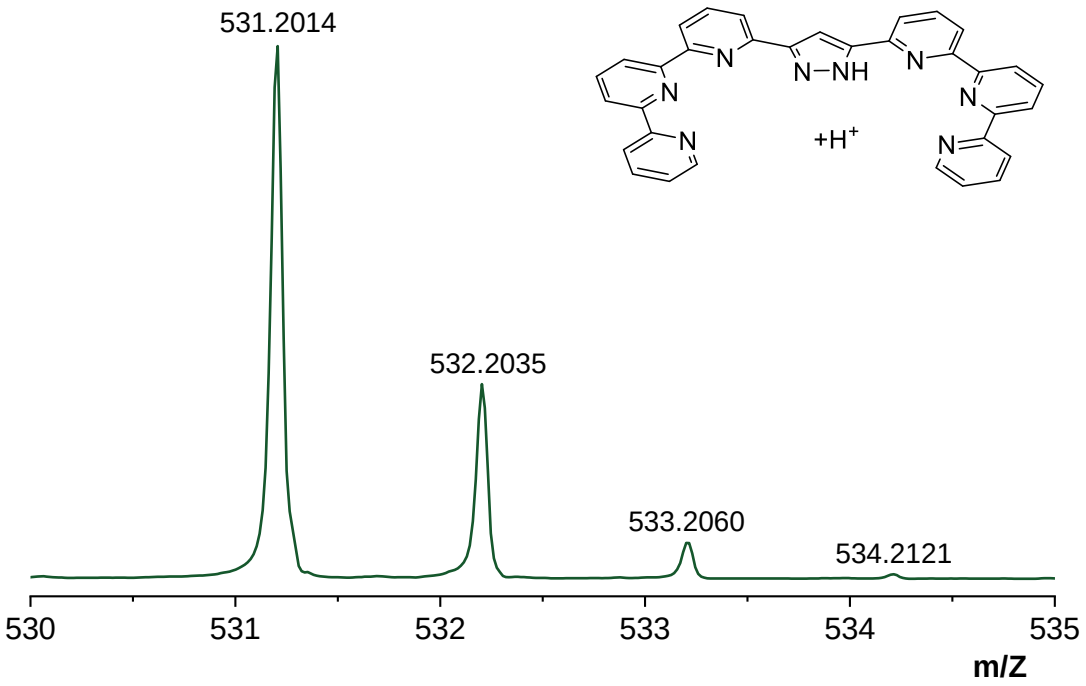

Simulated mass spectrum

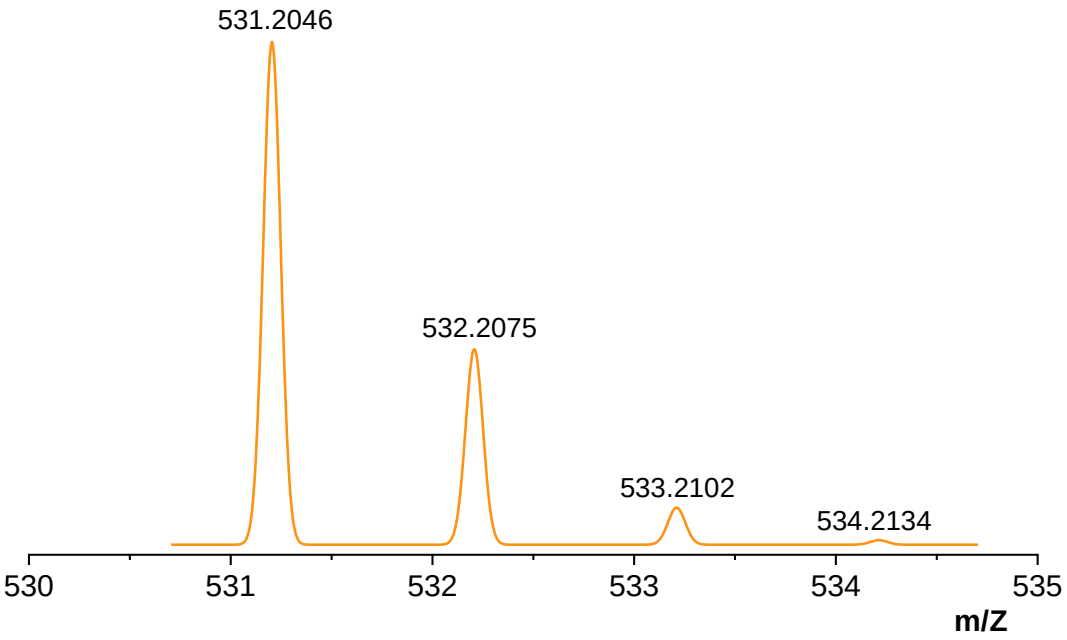

Figure S11. Experimental ESI–MS spectrum of the ligand **L–H** (top) and simulated ESI–MS spectrum using mMass software (bottom).

Cyclic voltammetry

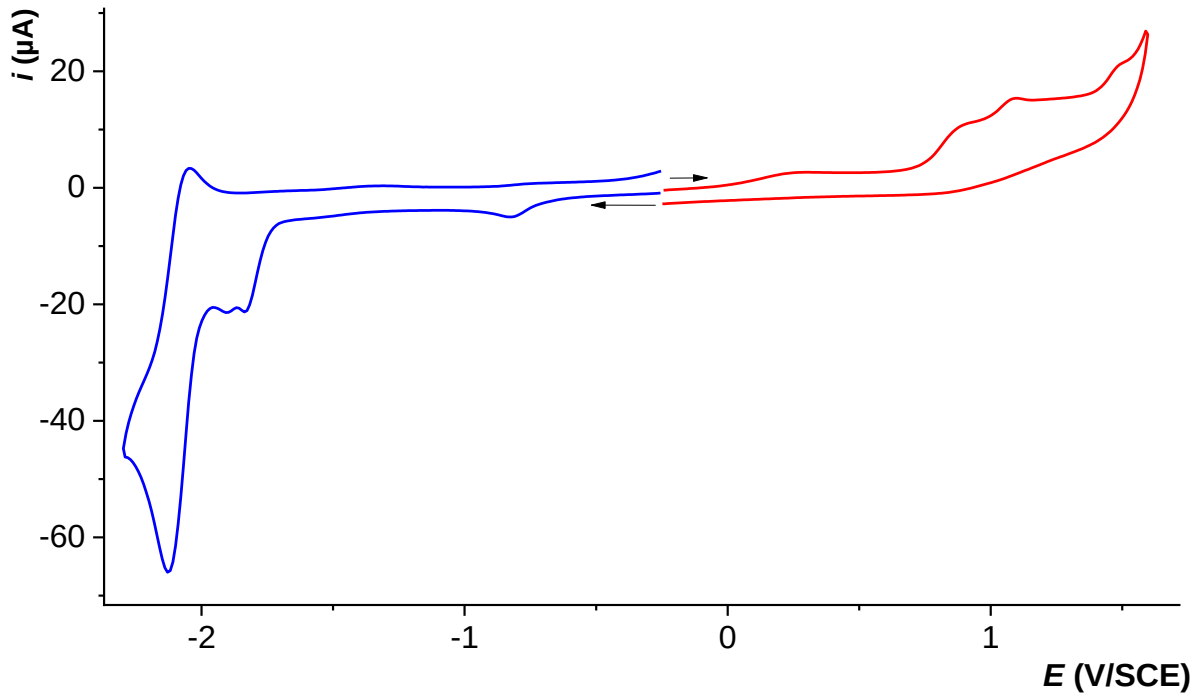

Figure S12. CV of the ligand **L–H** (1 mM) under argon in DMF with 0.1 M of $TBAPF_6$. Scan rate of 0.1 $V \cdot s^{-1}$.

2.2 Complex $[Co^{II}_2(L)(CH_3CN)_4][BF_4]_3$ (1)

2.2.1 General procedure

Ligand **L–H** (100 mg, 0.19 mmol) and ^{t}BuOK (25 mg, 0.22 mmol) were dissolved in dry THF (10 mL) and stirred for 1 h until no precipitated was observed and orange–yellow coloration appears. Later, 49 mg of $CoCl_2$ (0.38 mmol) were added, which made the solution dark along with blue precipitate from unreacted $CoCl_2$. After 1 h stirring, 185 mg of $AgBF_4$ (0.94 mmol) and 15 mL CH_3CN were added to the solution and the reaction flask was protected from light and let stir for 12 h. The crude solution was later filtered through celite inside the glove box and the solid washed with dry CH_3CN. After the solvent was removed under vacuum, the remaining solid was thoroughly washed with THF to remove excess of Ag salts. The remaining solid was dissolved in CH_3CN and passed through a 0.2 μm PTFE filter. Toluene was added to the solution and big, dark orange crystals were obtained by slow evaporation of CH_3CN from the solvent mixture. 90 % yield. *Crystallization was necessary to remove Ag^+ traces which were observed during electrochemical analysis.*

Elemental Analysis. Found: 41.50 C, 3.34 H, 11.73N. Theoretical for $[Co_2(L)(CH_3CN)_4][BF_4]_3$: 45.93 C, 3.10 H, 15.68 N.

The disparity between the theoretical and experimental values of the elemental analysis can be explained by the substitution of CH_3CN molecules by water molecules (samples meassured under air). Theoretical for $[Co_2(L)(H_2O)_{3.5}(CH_3CN)_{0.5}][BF_4]_3$: 41.19 C, 3.00 H, 12.01N.

ESI-HRMS (m/z pos): Found (Calc): $C_{33}H_{21}Co_2N_8^{3+}$ 215.6832 (215.6846).

2.2.2 X–Ray diffraction structure

$C_{45}H_{39}B_3Co_2F_{12}N_{14}$: M = 1154.19, orthorhombic, space group $Fdd2$, a = 35.3296(9), b = 13.5443(4), c = 20.8782(6) Å, V = 9990.5(5) Å^3, Z = 8, D_c = 1.535 g cm^{-3}, μ = 0.759 mm^{-1}, F(000) = 4672. Refinement of 348 parameters on 6452 independent reflections out of 154818 measured reflections (R_{int} = 0.047) led to R_1 = 0.025, wR_2 = 0.061, S = 1.045, $\Delta\rho_{max}$ = 0.46, $\Delta\rho_{min}$ = –0.22 e Å^{-3}, Flack parameter –0.004(10).

The Cambridge Crystallographic Data Centre (CCDC) contains the supplementary crystallographic data of complex **1**. These data can be obtained free of charge from via www.ccdc.cam.ac.uk/data_request/cif.

Atoms	Bond lengths [Å]	Atoms	Angles [°]
Co_1–N_1	2.123	N_1–Co_1–N_2	76.31
Co_1–N_2	2.101	N_2–Co_1–N_3	73.27
Co_1–N_3	2.112	N_3–Co_1–N_4	74.75
Co_1–N_4	2.149	N_5–Co_1–N_1	88.79
Co_1–N_5	2.167	N_5–Co_1–N_2	105.93
Co_1–N_6	2.149	N_6–Co_1–N_2	89.91
Co_1^i–N_1^i	2.123	N_1^i–Co_1^i–N_2^i	76.31
Co_1^i–N_2^i	2.101	N_2^i–Co_1^i–N_3^i	73.27
Co_1^i–N_3^i	2.112	N_3^i–Co_1^i–N_4^i	74.75
Co_1^i–N_4^i	2.149	N_5^i–Co_1^i–N_1^i	88.79
Co_1^i–N_5^i	2.167	N_5^i–Co_1^i–N_2^i	105.93
Co_1^i–N_6^i	2.149	N_6^i–Co_1^i–N_2^i	89.91

Table S1. Selected bond lengths [Å] and angles [°] for complex **1**.

2.2.3 ESI–MS

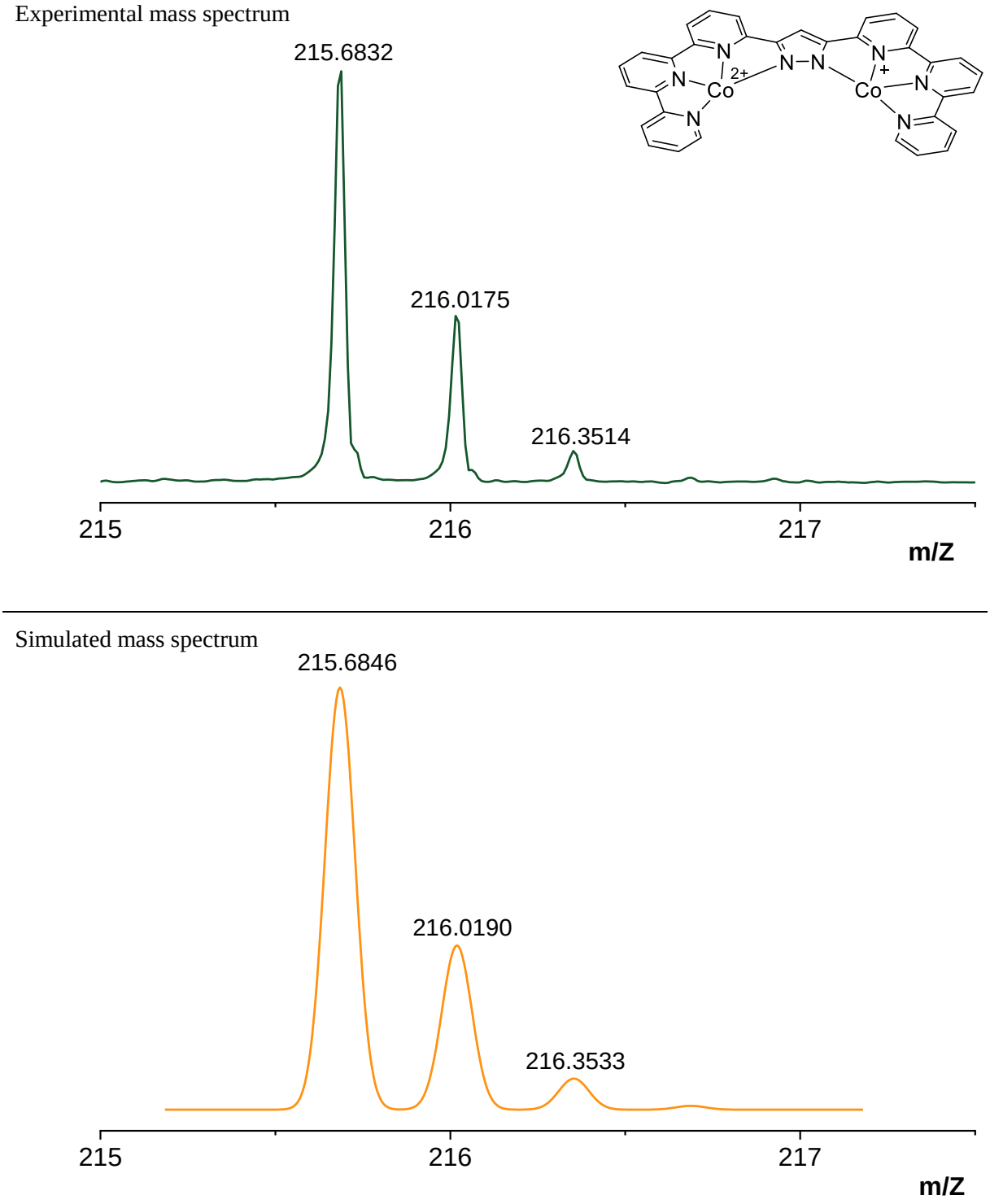

Figure S13. Experimental ESI–MS spectrum of complex **1** in CH_3OH (top) and simulated ESI–MS spectrum using mMass software (bottom).

2.2.4 UV–vis spectroscopy

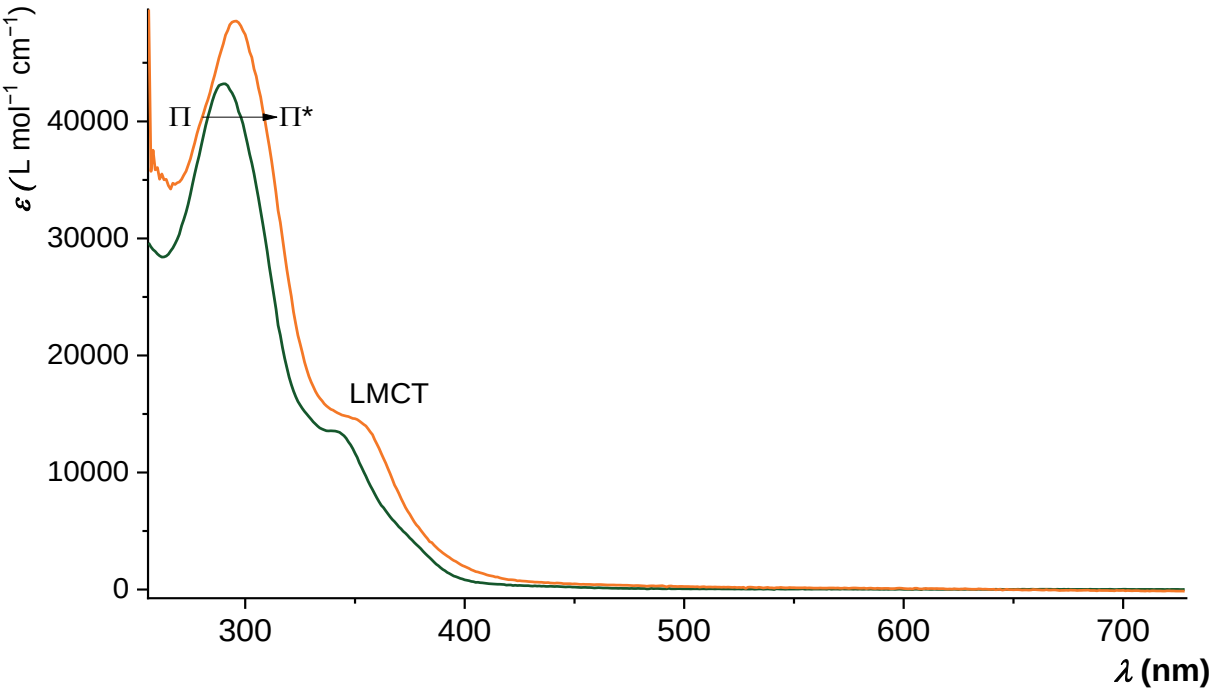

Figure S14. UV–visible spectra of complex **1** in CH_3CN (0.5 mM, green) and in DMF (0.3 mM, orange) with 0.1 M of $TBAPF_6$, the thickness of the quartz cell is 1 mm.

2.2.5 Measurement of magnetic moment by the Evans method

Equation (1):

$$\chi_g = \chi_0 \cdot \frac{3000 \cdot \Delta\upsilon}{4 \cdot \pi \cdot \upsilon_0 \cdot c \cdot M} + \frac{\chi_0 \cdot (\rho_0 - \rho_s)}{c} \qquad (1)$$

Where:

χ_g = mass susceptibility of the solute

χ_0 = mass susceptibility of the solvent

$\Delta\upsilon$ = observed frequency shift of the reference resonance (Hz)

υ_0 = spectrometer frequency (Hz)

c = concentration of the substance in mol/L

ρ_0 = density of the pure solvent

ρ_s = density of the solution

M = molecular weight

Assuming that $\rho_0 - \rho_s$ is zero and then multiplying by M simplifies to give Equation (2):

$$\chi_M = \frac{3000 \cdot \Delta\upsilon}{4 \cdot \pi \cdot \upsilon_0 \cdot c} \qquad (2)$$

Where χ_M = molar susceptibility of the solute ($cm^3 \cdot mol^{-1}$).

The uncorrected effective magnetic moment, μ_{eff}, has been calculated from the molar susceptibility using equation (3) without considering the diamagnetic contributions:

$$\mu_{eff} = 2.828 \cdot \sqrt{\chi_M \cdot T} \qquad (3)$$

Mass of **1** = 7.4 mg

M = 1072 g/mol

Solvent = 0.5 mL of CD_3CN solution containing THF and mesitylene as internal standards.

$\Delta\upsilon$ = 379 Hz for both signals of mesitylene.

$\Delta\upsilon$ = 310 and 350 Hz for THF signals.

υ_0 = 400 MHz

c = 0.0138 mol/L

T = 298 K

Using mesitylene signal shifts:

χ_M = 0.016 $cm^3 \cdot mol^{-1}$

$\boldsymbol{\mu_{eff}}$ = 6.232 (BM)

If no spin interaction between both cobalt centers is considered, the $\boldsymbol{\mu_{eff}}$ value falls low as compared to high spin octahedral monometallic Co^{II} complexes ($\boldsymbol{\mu_{theo}}$ = 3.88 (BM)) and falls high compared to low spin monometallic octahedral Co^{II} complexes ($\boldsymbol{\mu_{theo}}$ = 1.73 (BM)).

2.2.6 Nuclear magnetic resonance

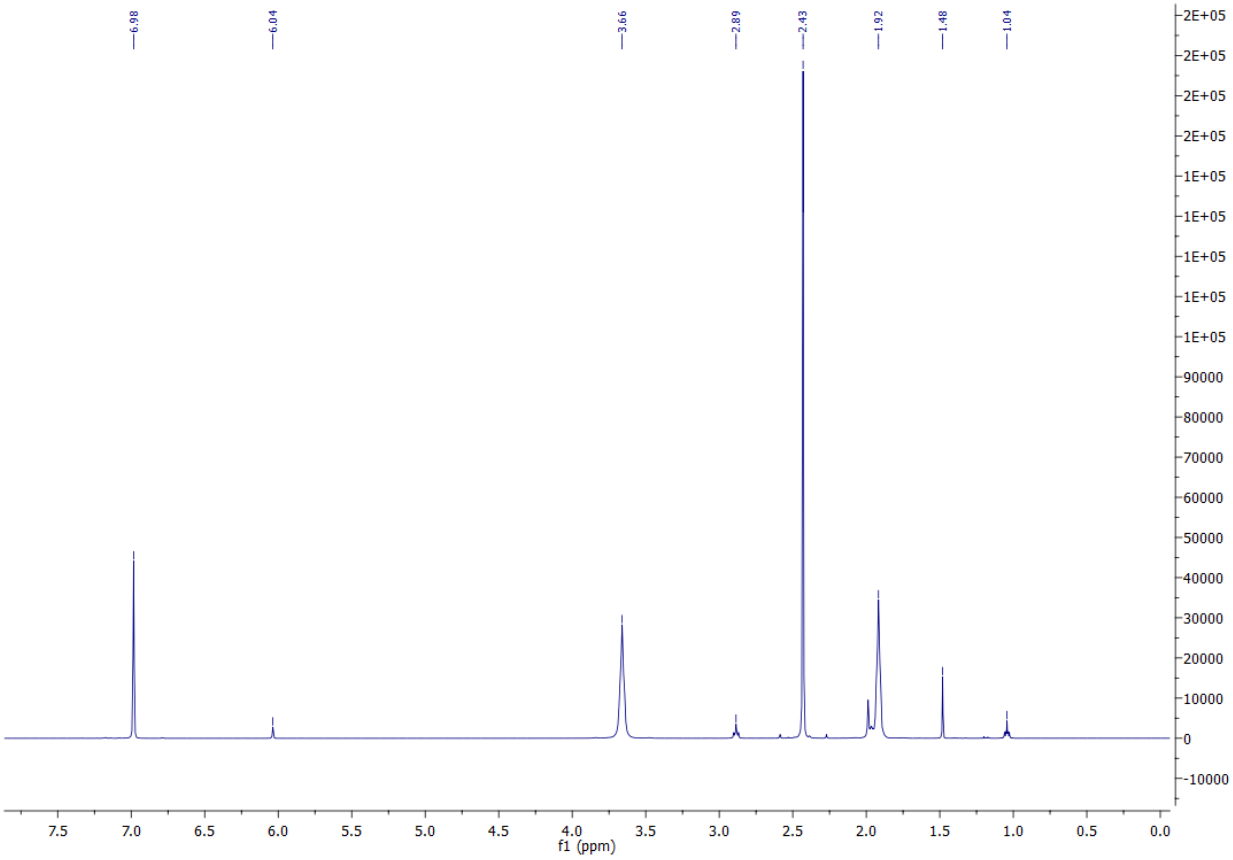

Figure S15. ^{1}H NMR spectrum (400 MHz) of a CD_3CN solution containing THF (3.66/2.89 and 1.92/1.04 ppm) and mesitylene (6.98/6.04 and 2.43/1.48 ppm) as internal standards and complex **1** (14 mM).

2.3 Complex $[Zn_2(L)(OTf)_3(CH_3CN)]$ (2)

2.3.1 General procedure

Ligand **L–H** (20 mg, 0.04 mmol) and ^{t}BuOK (5 mg, 0.05 mmol) were dissolved in dry THF (5 mL) and stirred for 30 min till no precipitated was observed and yellow coloration appears. Later, 20 mg of $ZnOTf_2$ (0.08 mmol) were added, which made the solution colorless and turbid. 10 minutes later, 5 mL of CH_3CN were added and the solution was left to stir for 12 h. The solvent was removed under vacuum and the crude, after adding 4 mL of CH_3CN, was passed through a 0.2 µm PTFE filter. To the solution, 10 mL of toluene were added, and colorless crystals were grown by slow evaporation of CH_3CN from the solvent mixture. 80% yield.

Elemental Analysis. Found: 35.46 C, 2.24 H, 9.03 N, 9.20 S. Theoretical for $[Zn_2(L)(OTf)_3(CH_3CN)]$: 39.74 C, 2.11 H, 10.98 N, 8.37 S.

The disparity between the teoretical and experimental values of the elemental analysis can be explained by contamiation of 1 molecule of trific acid coordinated to water molecules (samples meassured under air).

Theoretical for $[Zn_2(L)(OTf)_3(CH_3CN)][H_2O{\cdot}HOTf]$: 35.58 C, 2.07 H, 9.57 N, 9.74 S.

Theoretical for $[Zn_2(L)(OTf)_3(CH_3CN)][(H_2O)_2{\cdot}HOTf]$: 35.10 C, 2.19 H, 9.45 N, 9.61 S.

ESI-HRMS (m/z pos): Found (Calc): $C_{33}H_{21}Zn_2N_8^{3+}$ 219.0152 (219.0144).

2.3.2 Nuclear Magnetic Resonnance

^{1}H NMR (400 MHz, 20 ºC, $CH_3CN–d_3$): 9.10 (ddd, $^3J_{H,H}$ = 5.1, $^4J_{H,H}$ = 1.5, $^4J_{H,H}$ = 0.8 Hz, 2H), 8.67 (d, $^3J_{H,H}$ = 8.1 Hz, 2H), 8.62 (dd, $^3J_{H,H}$ = 7.5, $^4J_{H,H}$ = 1.1 Hz, 2H), 8.59 – 8.49 (m, 24), 8.45 – 8.40 (m, 4H), 8.37 (dt, $^3J_{H,H}$ = 7.6, $^4J_{H,H}$ = 1.8 Hz, 2H), 8.14 (dd, $^3J_{H,H}$ = 6.1, $^4J_{H,H}$ = 2.4 Hz, 2H), 7.77 (s, 1H), 7.51 (ddd, $^3J_{H,H}$ = 7.6, $^3J_{H,H}$ = 5.1, $^4J_{H,H}$ = 1.1 Hz, 2H) ppm.

$^{13}C\{^1H\}$ NMR (101 MHz, 20 ºC, $CH_3CN–d_3$): 151.1 (CH), 150.4 (C), 149.1 (C), 149.1 (C), 149.0 (C), 148.2 (C), 146.9 (C), 144.3 (CH), 143.9 (CH), 142.6 (CH), 128.2 (CH), 124.3 (CH), 123.6 (CH), 123.5 (CH), 122.0 (CH), 121.0 (CH), 121.8 (CF_3, $^1J_{CF}$ = 320 Hz), 102.1(CH) ppm.

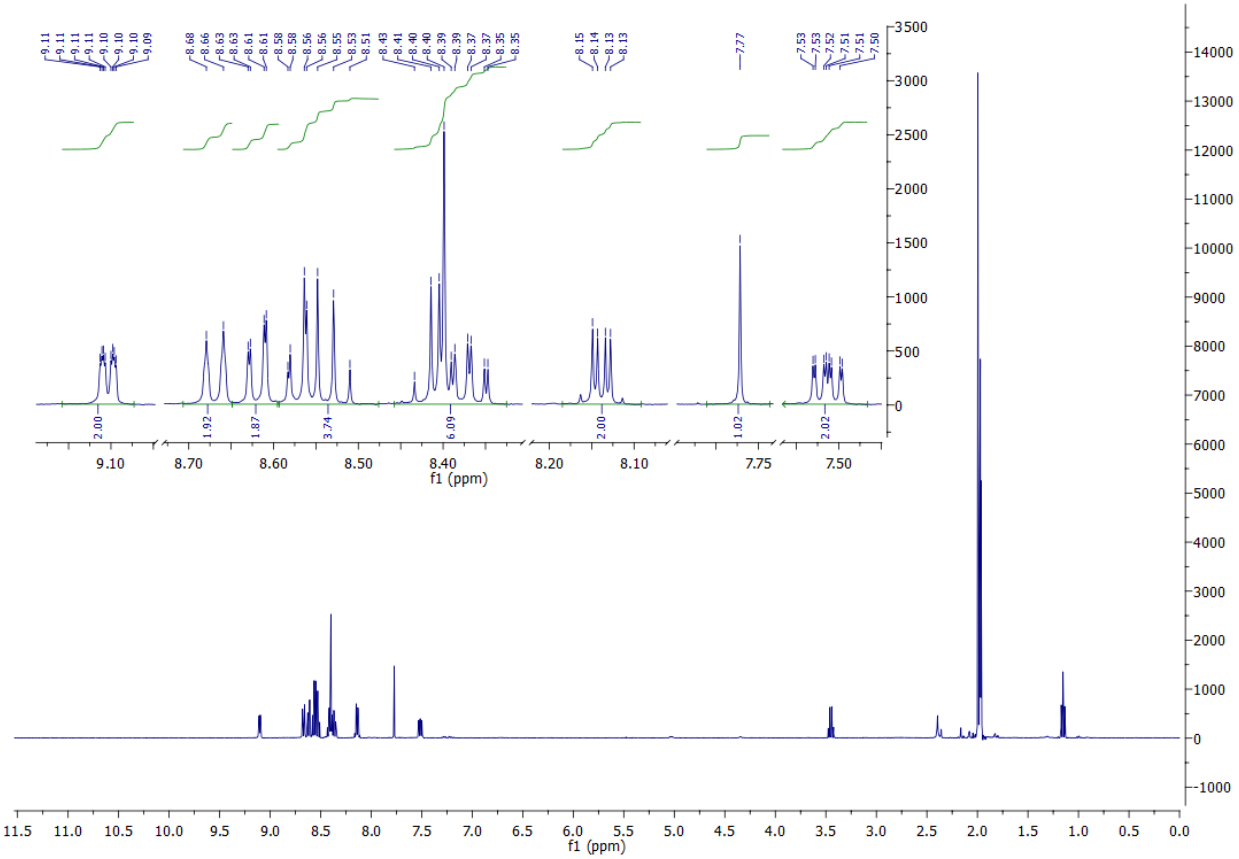

Figure S16. ^{1}H NMR spectrum (400 MHz) of **2** in $CH_3CN–d_3$ solution .

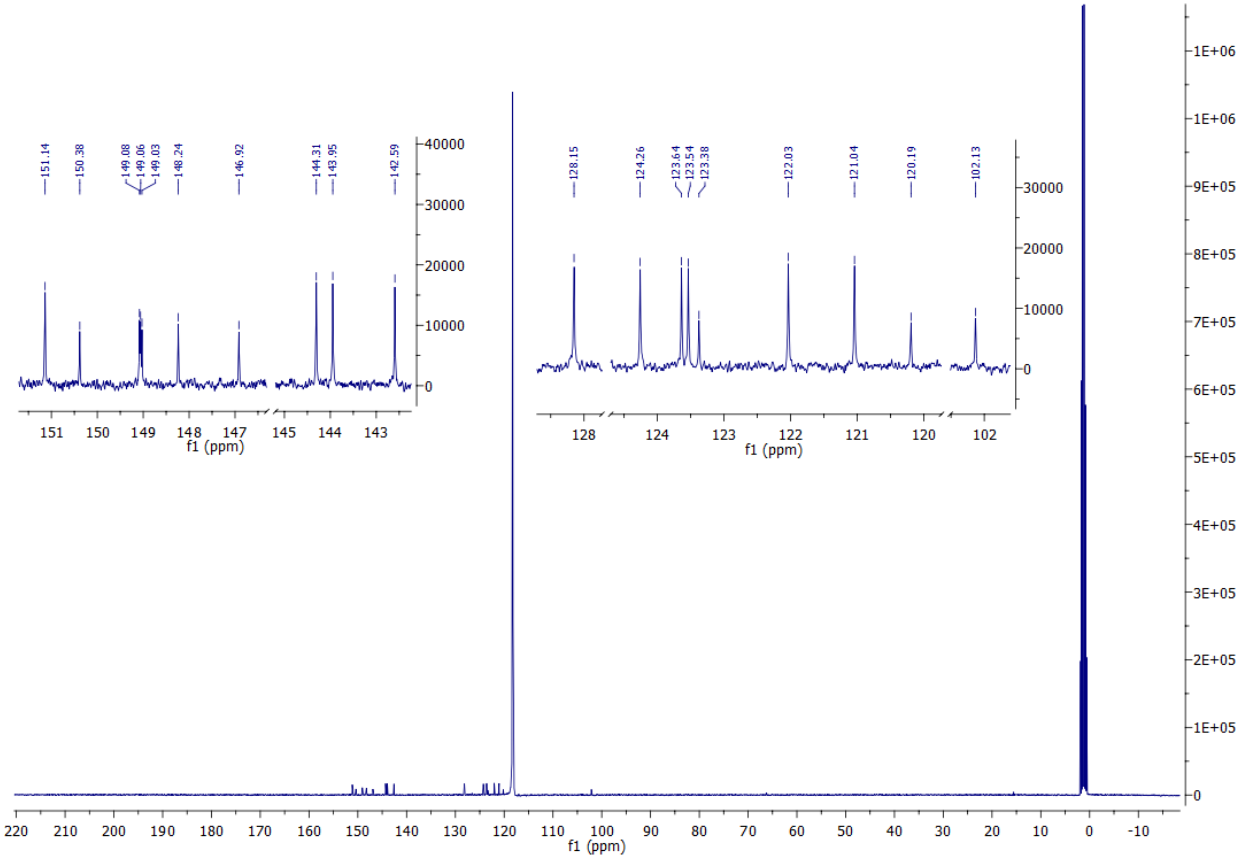

Figure S17. $^{13}C\{^{1}H\}$ spectrum (101 MHz) of **2** in $CH_3CN–d_3$ solution.

Experimental mass spectrum

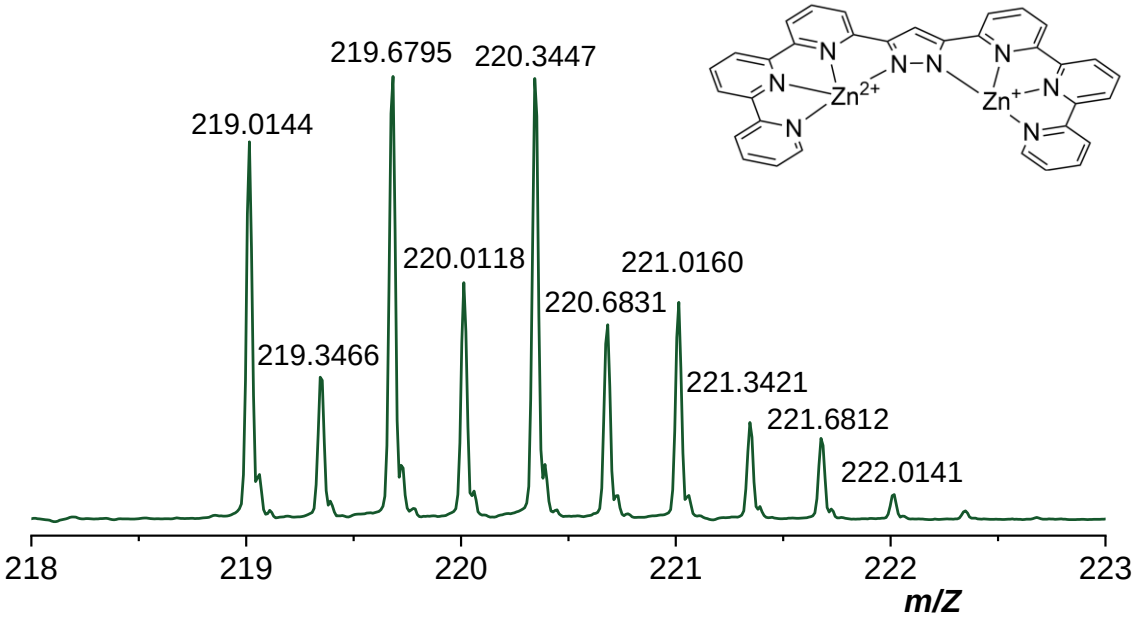

Simulated mass spectrum

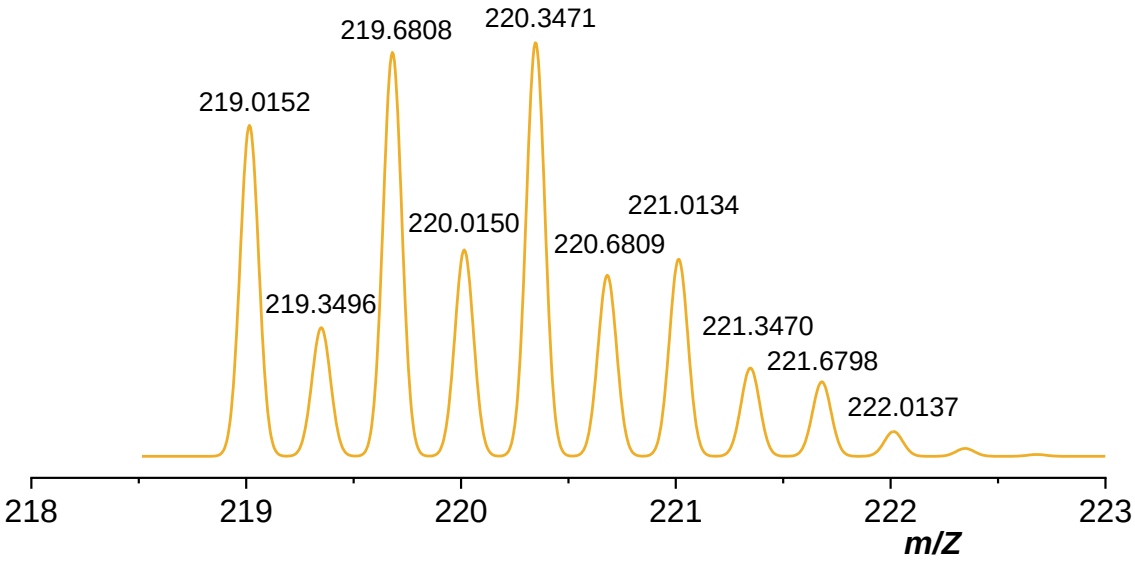

Figure S18. Experimental ESI–MS spectrum of **2**, (top) and simulated ESI–MS spectrum using mMass software (bottom).

3 Electrochemical studies of complex 1 under argon

3.1 Study in CH_3CN

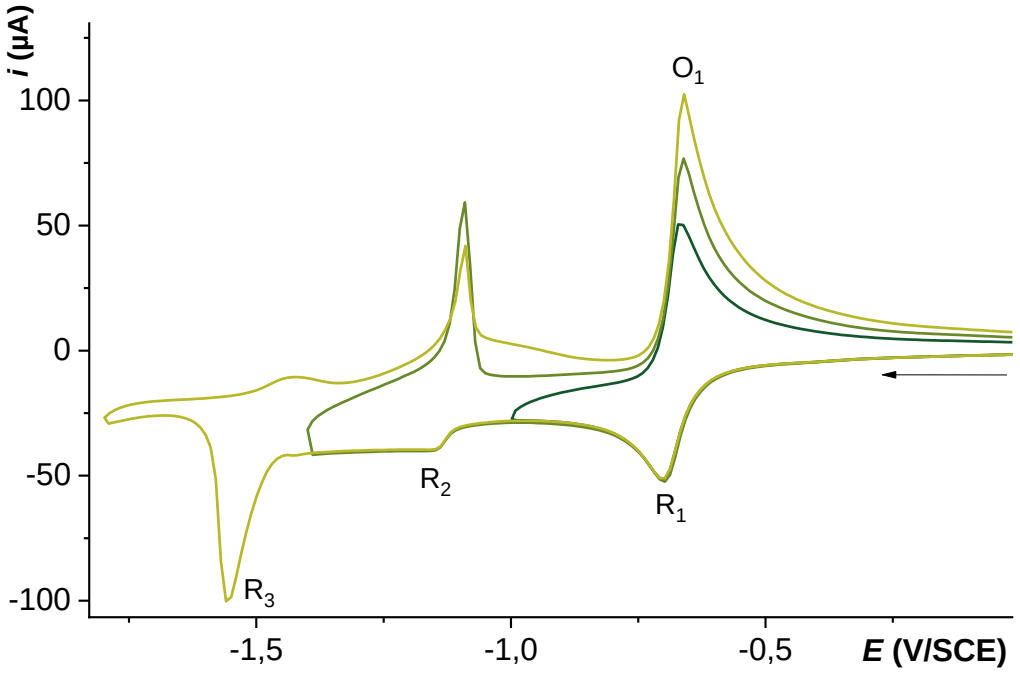

Figure S19. CVs of complex **1** (0.5 mM) under argon atmosphere in CH_3CN with 0.1 M of $TBAPF_6$. Scan rate of 0.5 $V \cdot s^{-1}$.

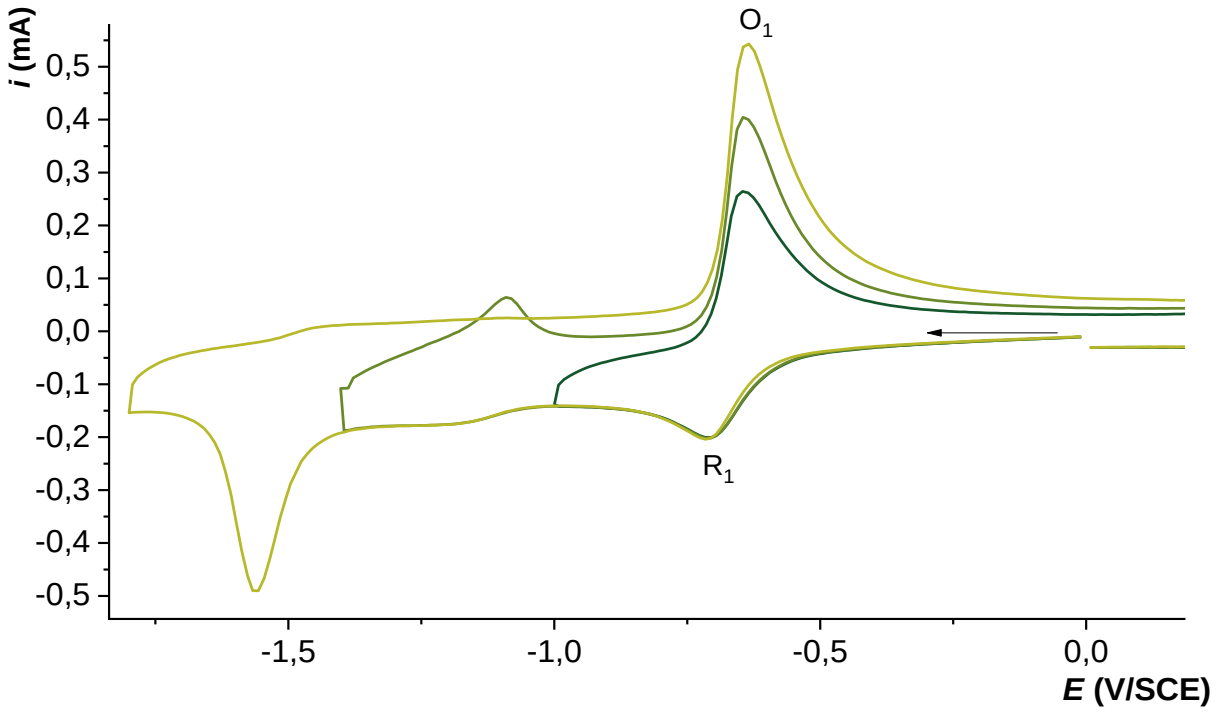

Figure S20. CVs of complex **1** (0.5 mM) in reduction under argon atmosphere in CH_3CN with 0.1 M of $TBAPF_6$. Scan rate of 10 $V \cdot s^{-1}$.

Complex **1** presents several redox waves, to assign their respective number of electrons involved the method developed by Amatore *et al*. was used.[3] Chronoamperometry using a micro electrode and Ultra Micro Electrode (UME) voltammograms were recorded on a 1 mM solution of complex **1** in the presence of ferrocene (1 mM) used as a reference.

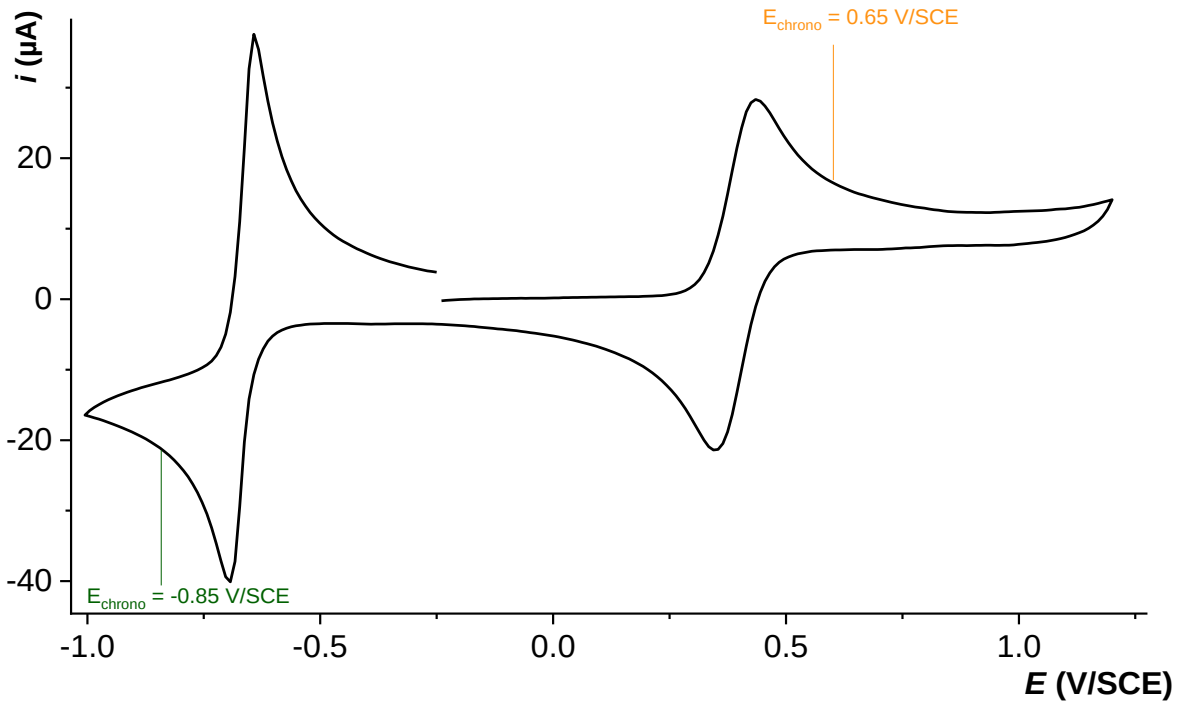

Figure S21. CV of complex **1** (1 mM) with ferrocene (1 mM) in reduction under argon atmosphere in CH_3CN with 0.1 M of $TBAPF_6$. Scan rate of 0.1 $V \cdot s^{-1}$. The working electrode was a steady glassy carbon electrode of 0.07 cm^2 surface area.

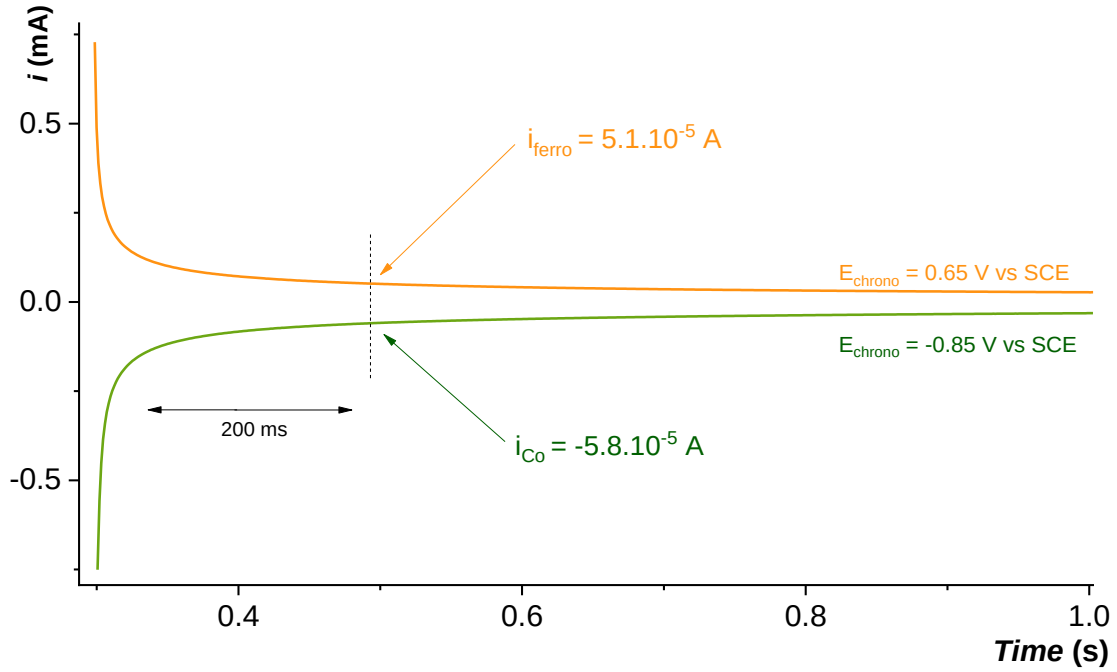

Figure S22. Chronoamperometry of complex **1** (1 mM) at –0.85 V vs SCE and ferrocene (1 mM) at 0.65 V vs SCE under argon atmosphere in CH_3CN with 0.1 M of $TBAPF_6$.The working electrode was a steady glassy carbon electrode of 0.07 cm² surface area.

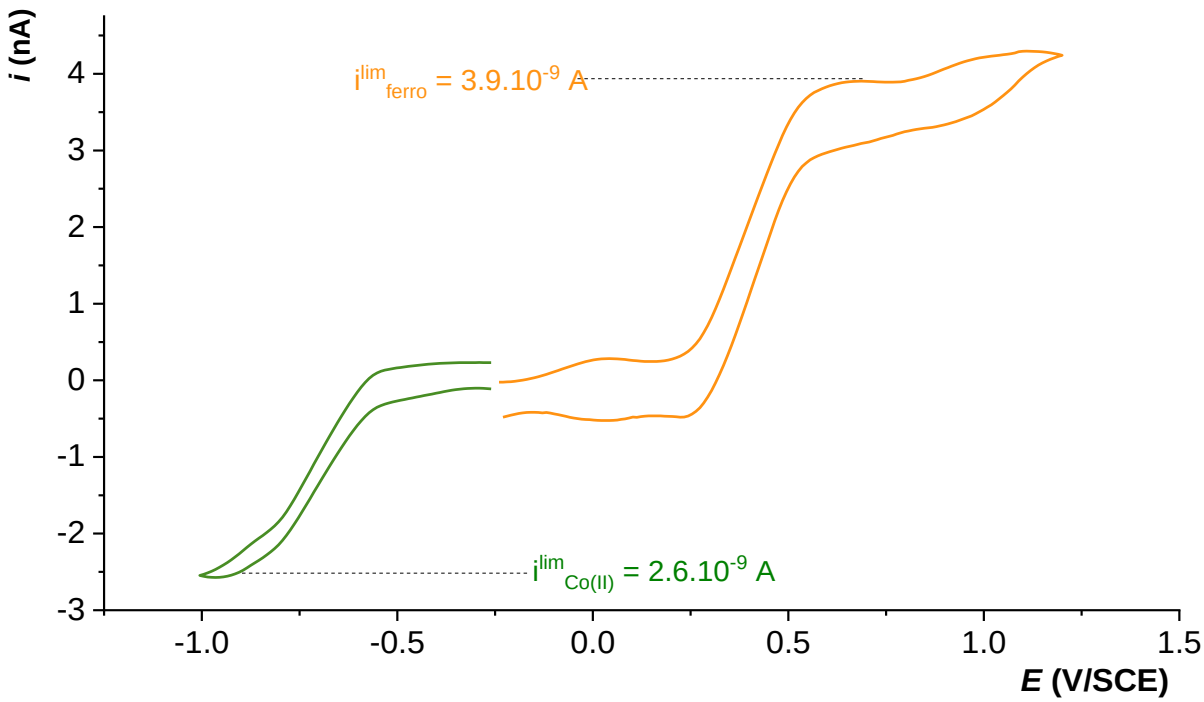

Figure S23. CVs of complex **1** (1 mM) with ferrocene (1 mM) in reduction under argon atmosphere in CH_3CN with 0.1 M of $TBAPF_6$. Scan rate of 0.1 $V \cdot s^{-1}$. The working electrode was a 7 µm diameter Ultra Micro Electrode.

Chronoamperometry and voltammograms on UME allow to measure respectively current values according to Coterell's and Randles Sevcik's laws for the cobalt complex and for ferrocene.

These different current values can be used to determine the number of electrons exchanged during the first reduction wave of the Co(II) complex. The equations are detailed in the table below.

Unknown parameter	$\mathbf{n_{Co(II)}}$
Known Parameters	$\mathbf{n_{ferro} = 1}$ $\mathbf{C_{ferro}, C_{Co(II)}}$ $\mathbf{C_{ferro} = C_{Co(II)}}$
Chronoamperometry (given by the Cottrell Law)	$\frac{i_{Co(II)}}{i_{ferro}} = \frac{n_{Co(II)} D_{Co(II)}^{\frac{1}{2}}}{n_{ferro} D_{ferro}^{\frac{1}{2}}} = A$
CVs on UME (given by the Randles–Sevcik equation)	$\frac{i_{Co(II)}^{lim}}{i_{ferro}^{lim}} = \frac{n_{Co(II)} D_{Co(II)}}{n_{ferro} D_{ferro}} = B$
Determination	$n_{Co(II)} = n_{ferro} \frac{A^2}{B}$

Table S2. Equations used to determine the number of electrons of the first cathodic wave of complex **1**. Cottrell law was used for chronoamperometry and Randles–Sevcik equation for CVs on UME.

As we know the $\mathbf{n_{ferro}}$ value (1), $\mathbf{n_{Co(II)}}$ = 1,9 (± 0.3) electrons for the first cathodic wave.

This result allows us to determine the diffusion coefficient of complex **1** thanks to the variation of the scan rate, results are presented below (**Figure S21**).

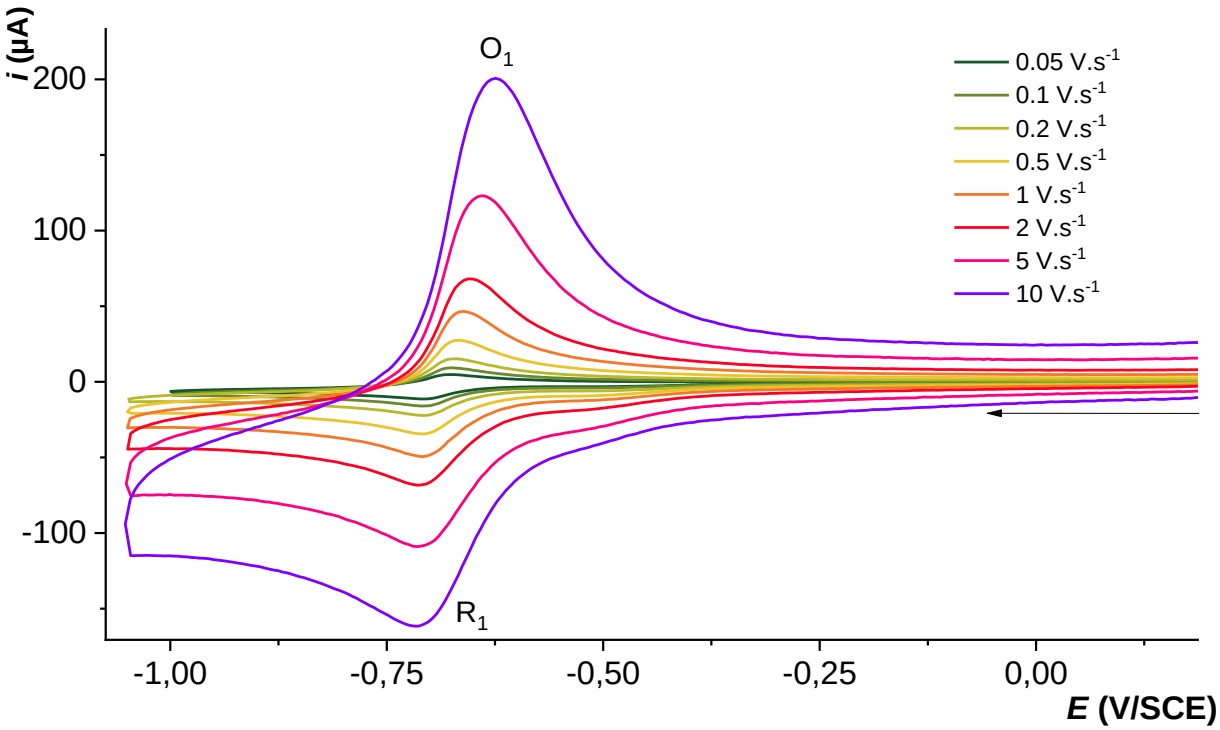

Figure S24. CVs of complex **1** (0.5 mM) under argon in anhydrous CH_3CN with 0.1 M of $TBAPF_6$, at 20 °C at variable scan rates.

By measuring the cathodic intensity at each scan rate, the diffusion coefficient of complex **1** can be calculated thanks to the Randles–Sevcik equation:

$$\mathrm{i} = \left(0{,}4463nFAC\sqrt{\frac{nF}{RT}}\right)\sqrt{D}\sqrt{v}$$

i = current maximum in amps

n = number of electrons transferred in the redox event (usually 1)

A = electrode area in cm^2

F = Faraday Constant in C mol^{-1}

D = diffusion coefficient in cm^2/s

C = concentration in mol/cm^3

v = scan rate in V/s

R = Gas constant in J K^{-1} mol^{-1}

T = temperature in K

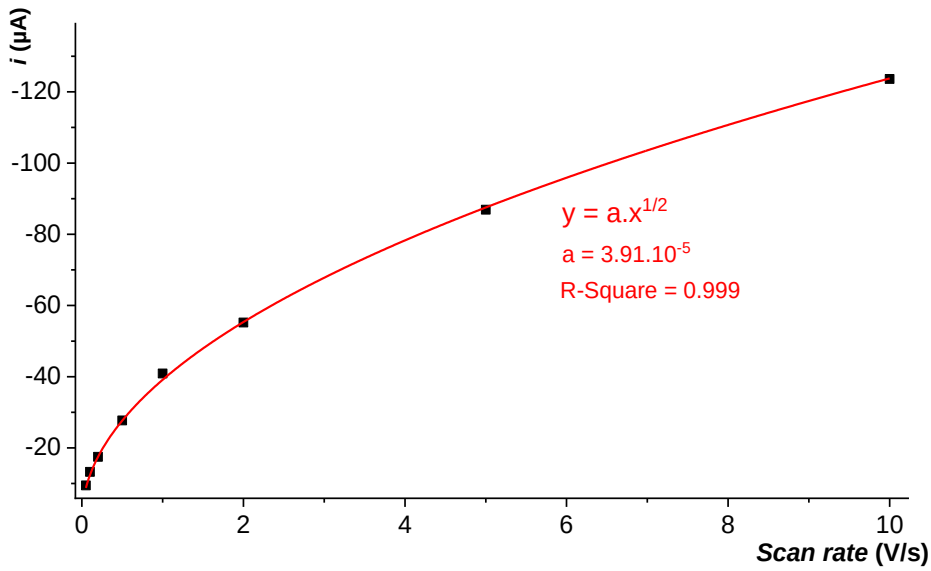

Figure S25. Maximum current (i_{pf}) of the cathodic wave R_1 of complex **1** in CH_3CN as a function of the scan rate.

For a two–electron cathodic wave : $\mathbf{D_{Co(II)} = 2.1 \cdot 10^{-6}\ cm^2 \cdot s^{-1}}$

By scanning to more negative potentials, the anodic wave O_1 become more intense (**Figure S19**) and seems to involve a process with more than two electrons.

For the O_1 anodic wave: $\mathbf{n_{e-} = 4.4\ e^-}$

The previous method could not be applied to determine the number of e– involved for R_2 and R_3 because of the passivation of the UME.

3.1.1 Comparison with $[Zn^{II}_2(L)(CH_3CN)_4][OTf]_3$ (2)

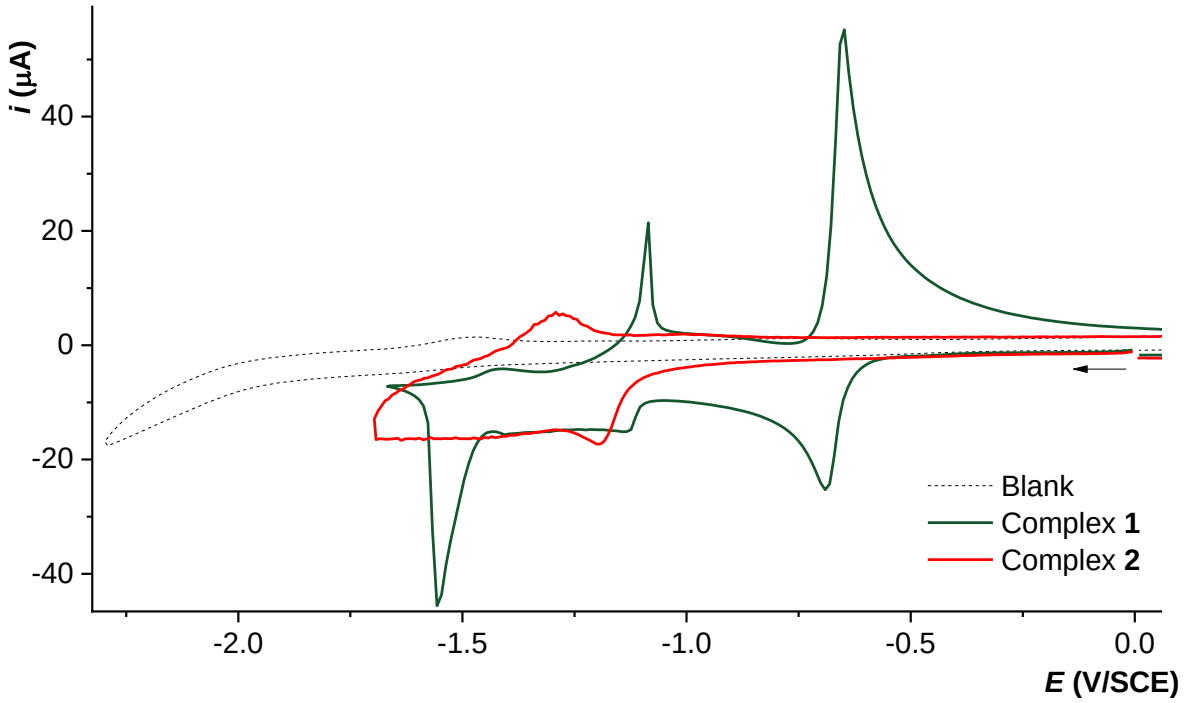

Figure S26. CVs of complex **1** (0.5 mM, green) and complex **2** (0.5 mM, red) under argon atmosphere in CH_3CN with 0.1 M of $TBAPF_6$. Scan rate of 0.1 $V \cdot s^{-1}$.

3.2 Study in DMF

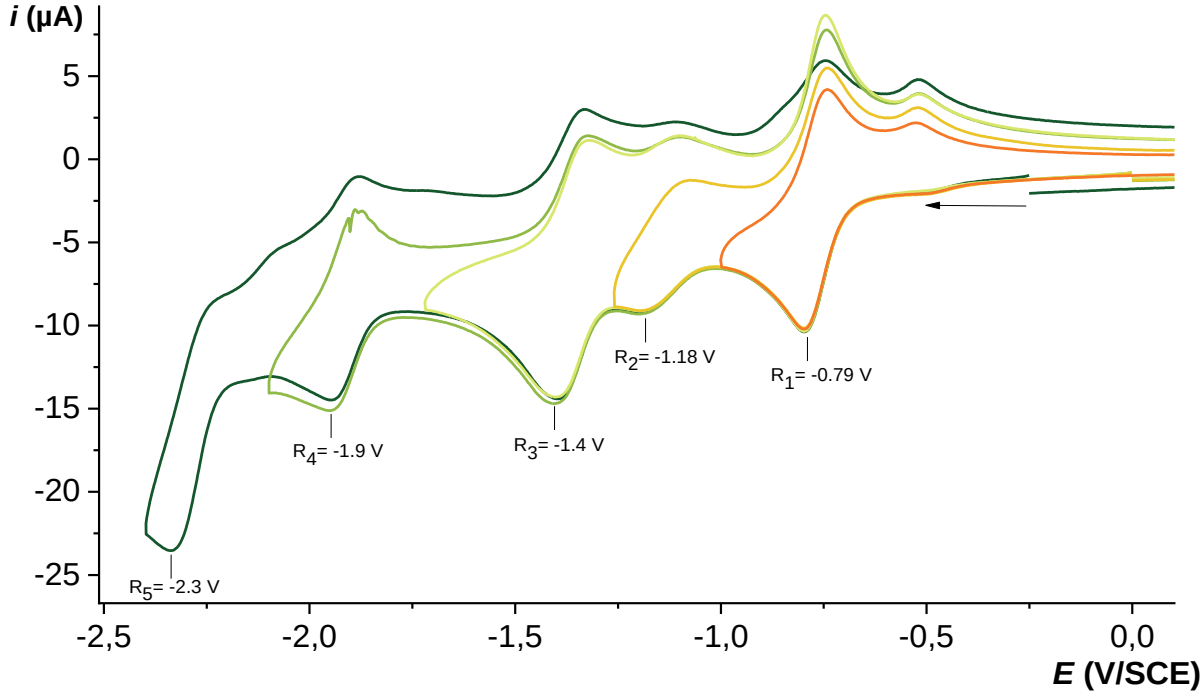

Figure S27. CVs of complex **1** (0.5 mM) under argon in anhydrous DMF with 0.1 M of $TBAPF_6$, at 20 °C, scan rate of 0.1 $V \cdot s^{-1}$

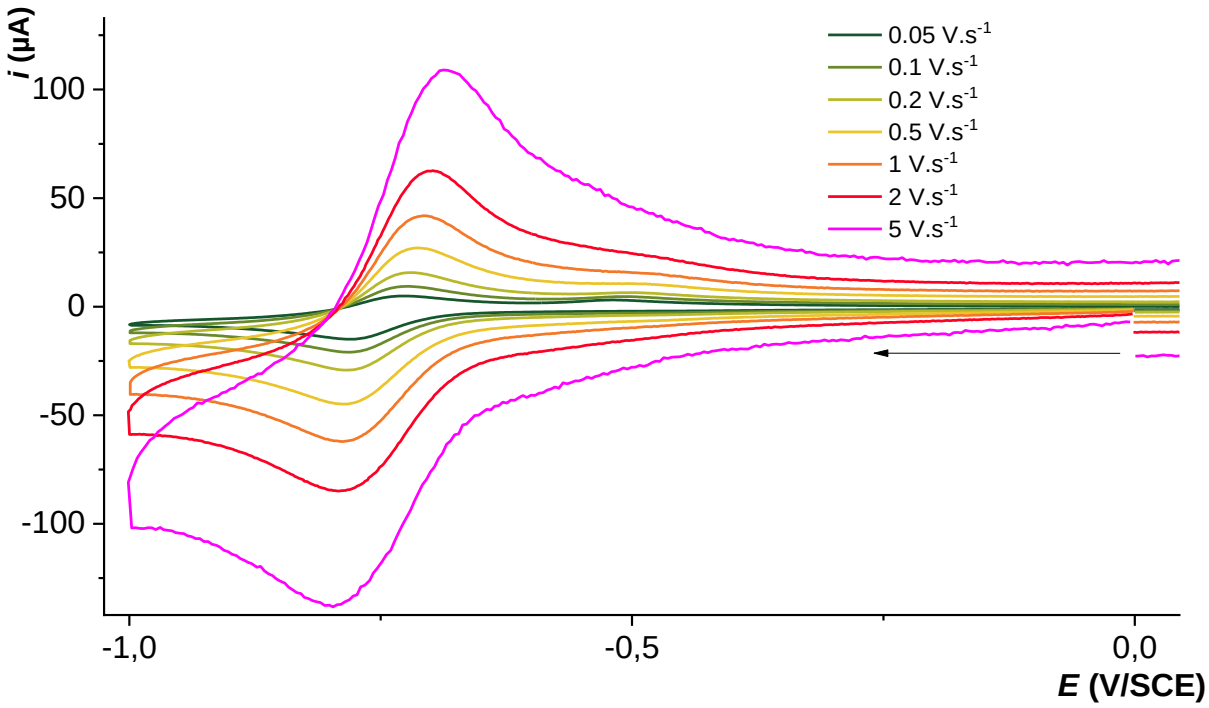

Figure S28. CVs of complex **1** (1 mM) under argon in anhydrous DMF with 0.1 M of $TBAPF_6$, at 20 °C at different scan rates.

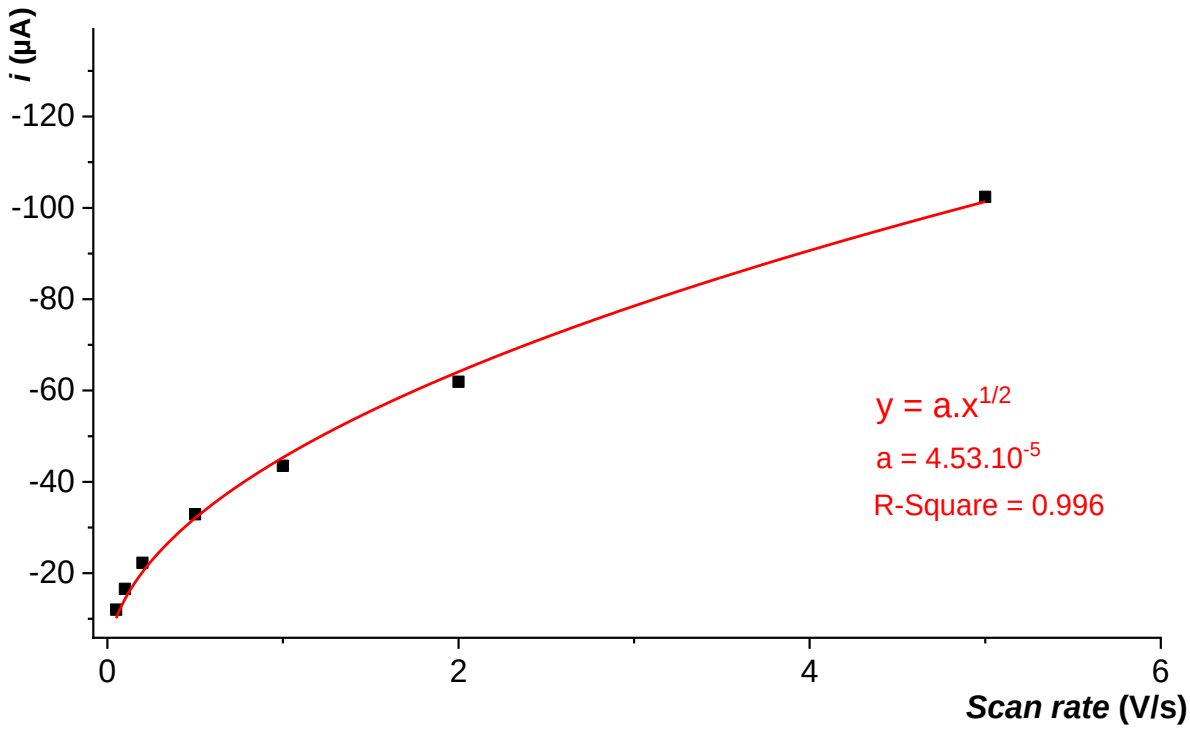

Figure S29. Maximum current (i_{pf}) of the cathodic wave R_1 of complex **1** in DMF as a function of the scan rate.

For a two–electron cathodic wave in DMF: $\mathbf{D_{Co(II)} = 7.1 \cdot 10^{-7}\ cm^2 \cdot s^{-1}}$

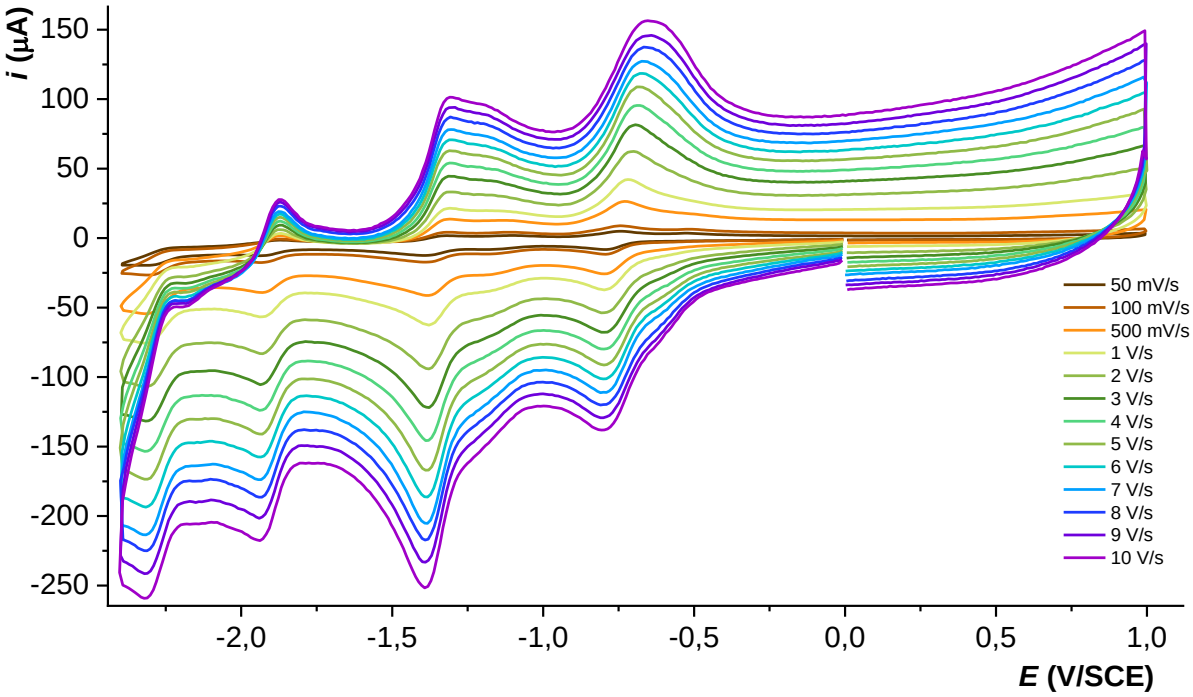

Figure S30. CVs of complex **1** (0.5 mM) under argon in anhydrous DMF with 0.1 M of $TBAPF_6$, at 20 °C at variable scan rates, CVs are normalized at 0.1 V s^{-1}.

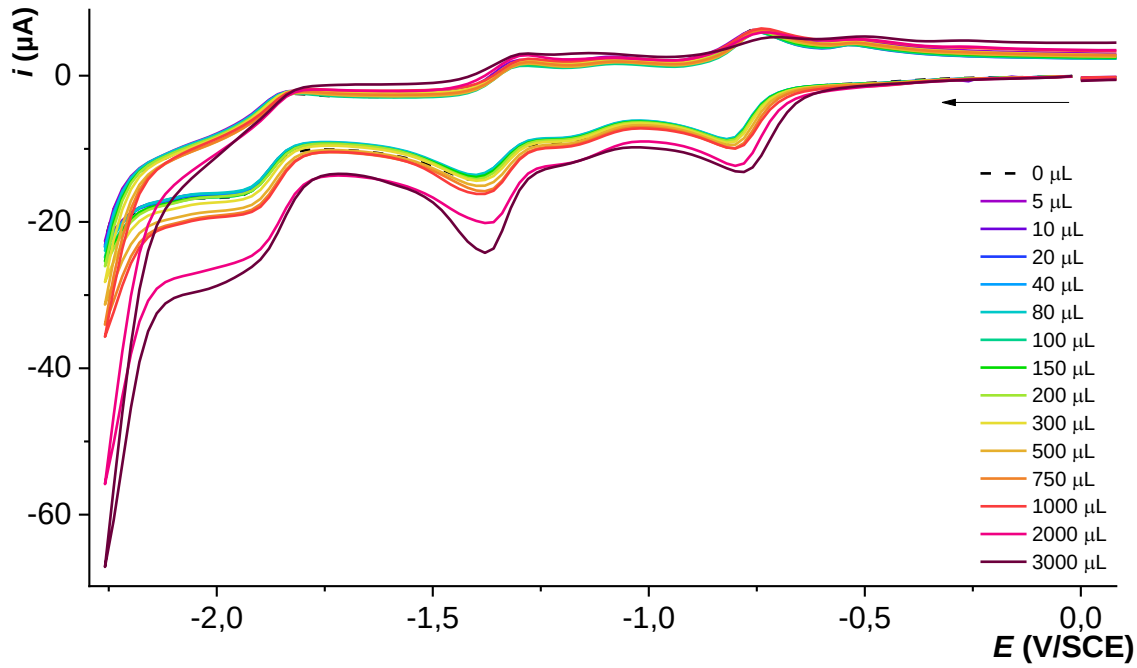

Figure S31. CVs of complex **1** (0.5 mM) under argon in DMF with increasing amount of CH_3CN with 0.1 M of $TBAPF_6$, at 20 °C, CVs are normalized to a concentration of 0.5 mM of complex.

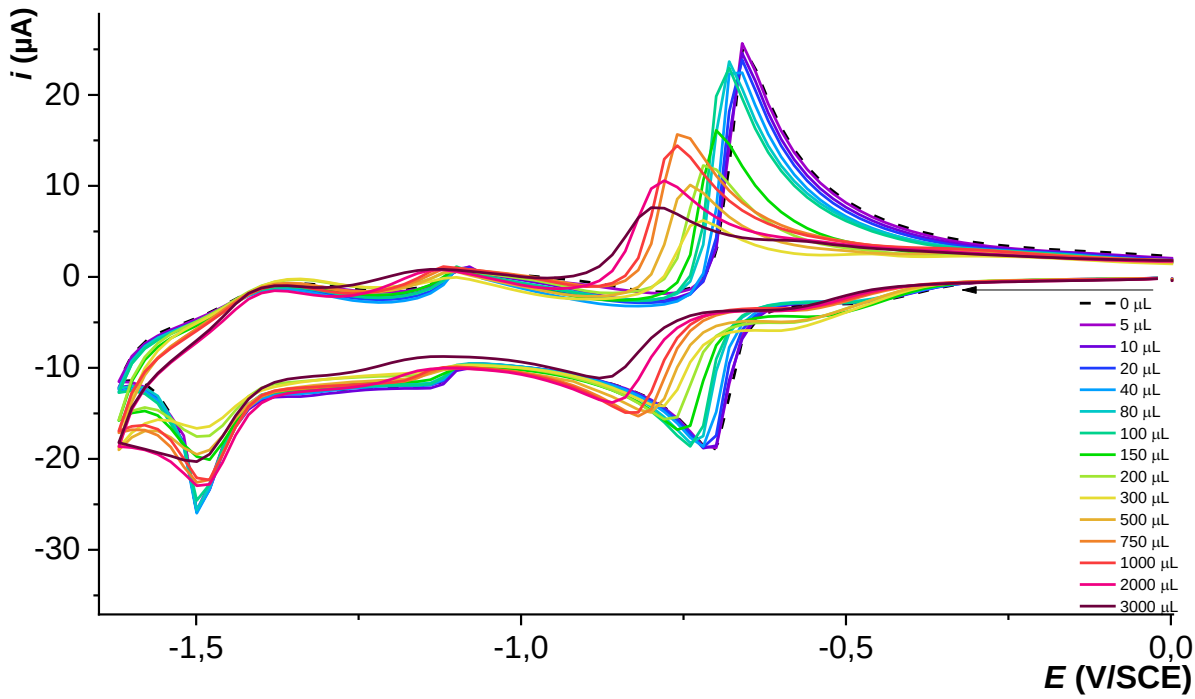

Figure S32. CVs of complex **1** (0.5 mM) under argon in CH_3CN with increasing amount of DMF with 0.1 M of $TBAPF_6$, at 20 °C, CVs are normalized to a concentration of 0.5 mM of complex.

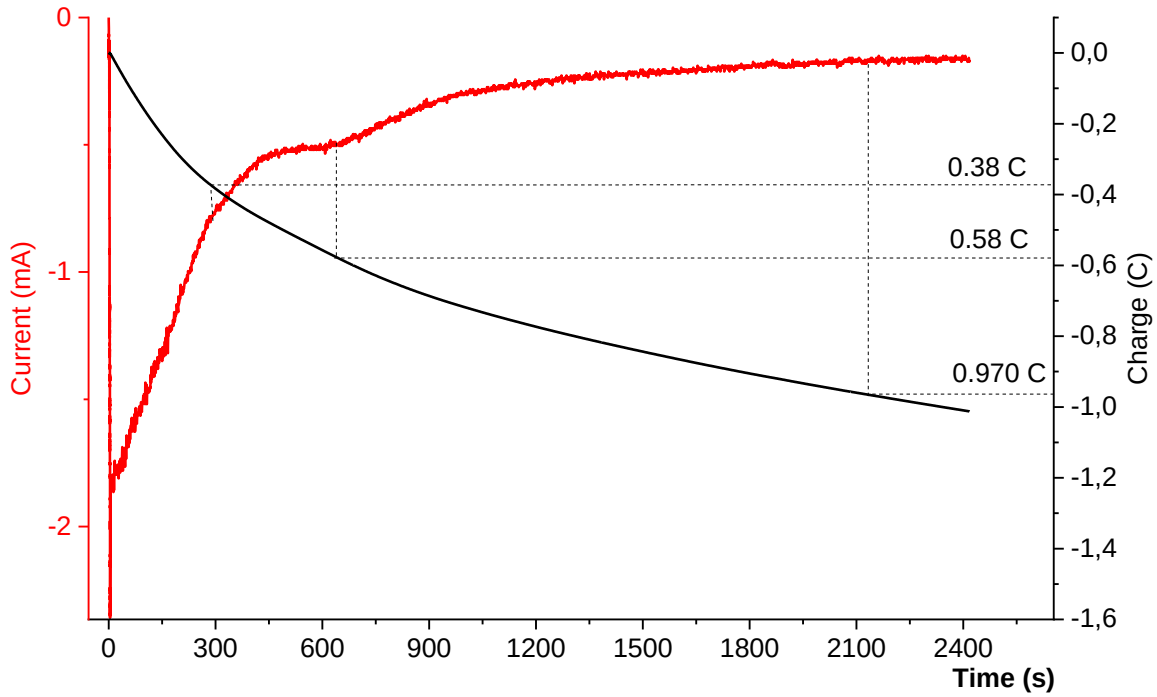

Figure S33. Current (red) and charge (black) overtime during potentiostatic coulometry of complex **1** (0.5 mM) under argon in DMF with 0.1 M of $TBAPF_6$, at 20 °C, potential applied at -1.6 V *vs* SCE (see Figure S27).

$Q = n_{e-} F$

n_{e-}= number of mol of electrons transferred in the redox event

F = Faraday Constant in C mol^{-1}

For 1 mM of e- (2 e-) involved in the reduction of **1**: Q = 0.38 C

For 1.5 mM of e- (2 + 1 e-) involved in the reduction of **1**: Q = 0.58 C

For 2.5 mM of e- (2 + 2 + 1 e-) involved in the reduction of **1**: Q = 0.97 C

3.2.1 Comparison with $[Zn^{II}_2(L)(CH_3CN)_4][OTf]_3$ (2)

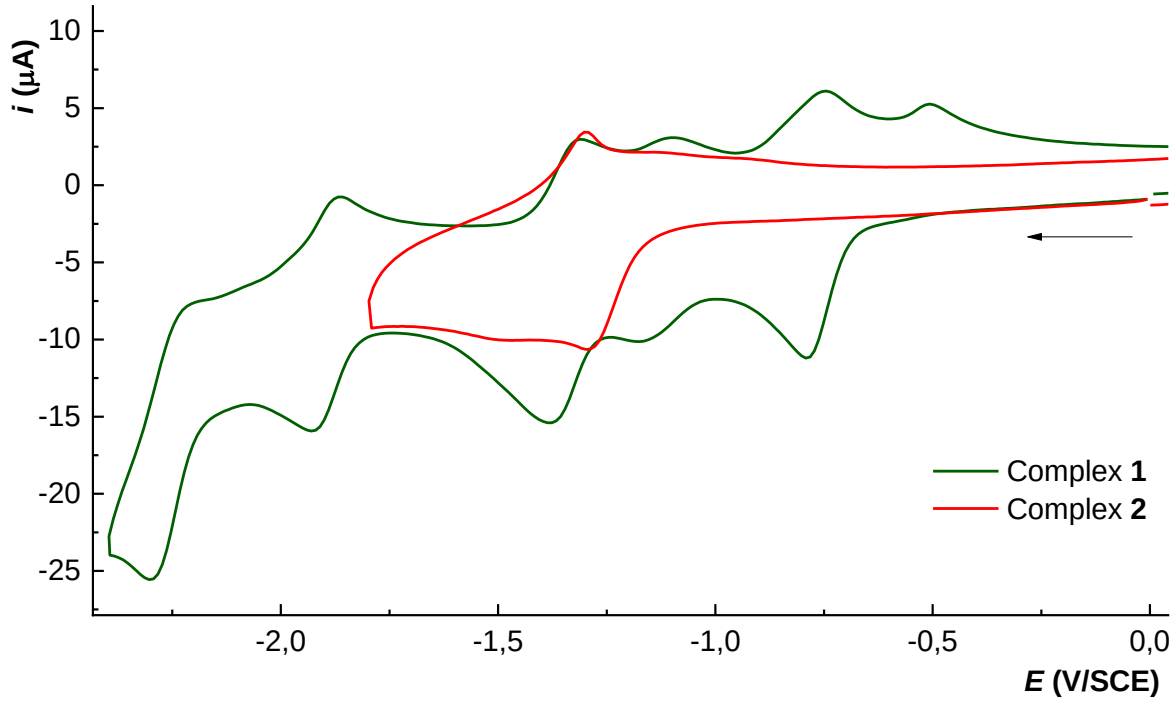

Figure S34. CVs of complex **1** (0.5 mM, green) and complex **3** (0.5 mM, red) under argon atmosphere in DMF with 0.1 M of $TBAPF_6$. Scan rate of 0.1 $V \cdot s^{-1}$.

4 *In–situ* characterization of complex $[Co^{I}_{2}(L)](BF_4)$ (3)

4.1.1 UV–vis spectro–electrochemical analysis. Electroreduction of complex 1.

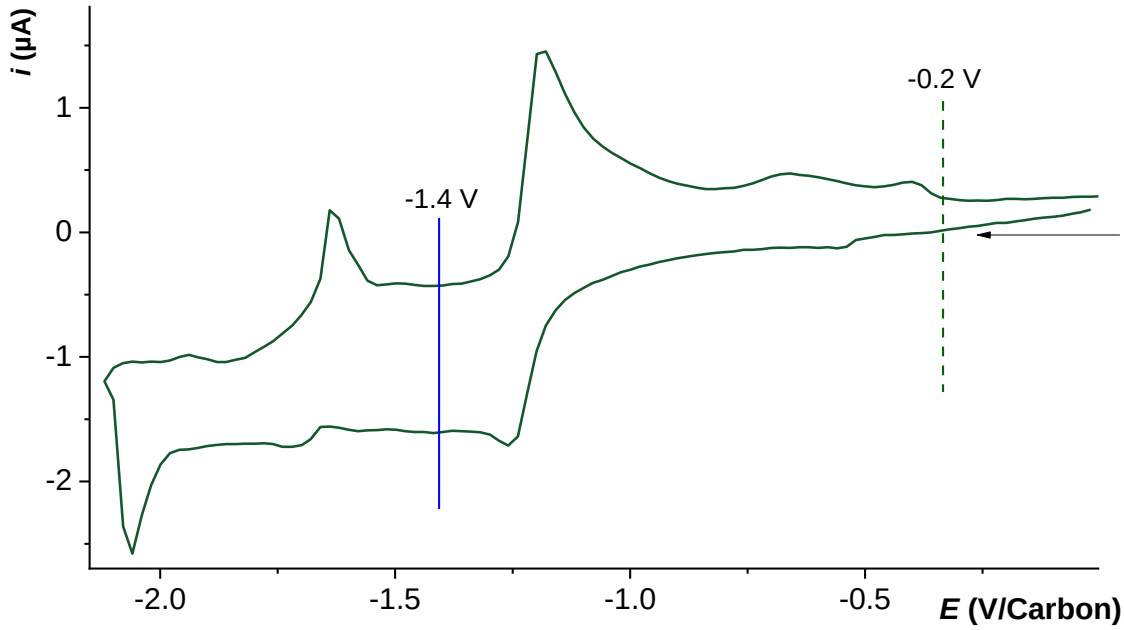

Figure S35. CV of complex **1** (0.5 mM) under argon in CH_3CN with 0.1 M of $TBAPF_6$ in a UV–vis spectro–electrochemical cell (**see Figure S1**). Scan rate of 0.1 $V \cdot s^{-1}$.

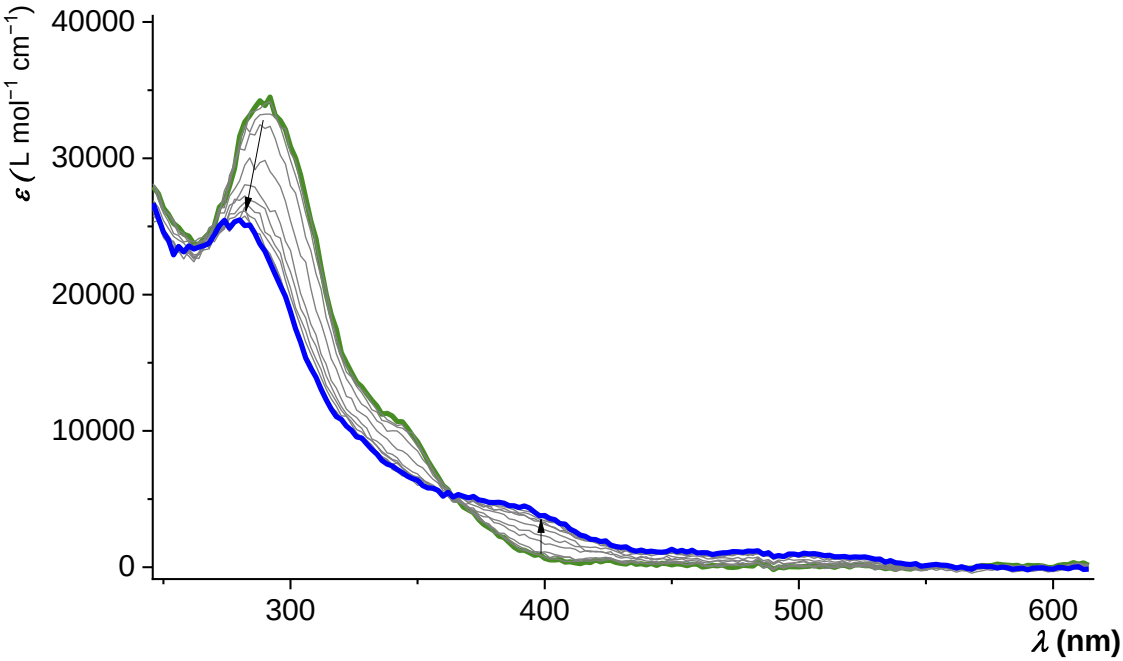

Figure S36. UV–visible spectra of 0.5 mM of complex **1** before CPE at –1.4 V (green curve), and after electrolysis at –1.4 V (blue). Spectra are recorded in CH_3CN with 0.1 M of $TBAPF_6$, in the spectro–electrochemistry cell shown in **Figure S1**.

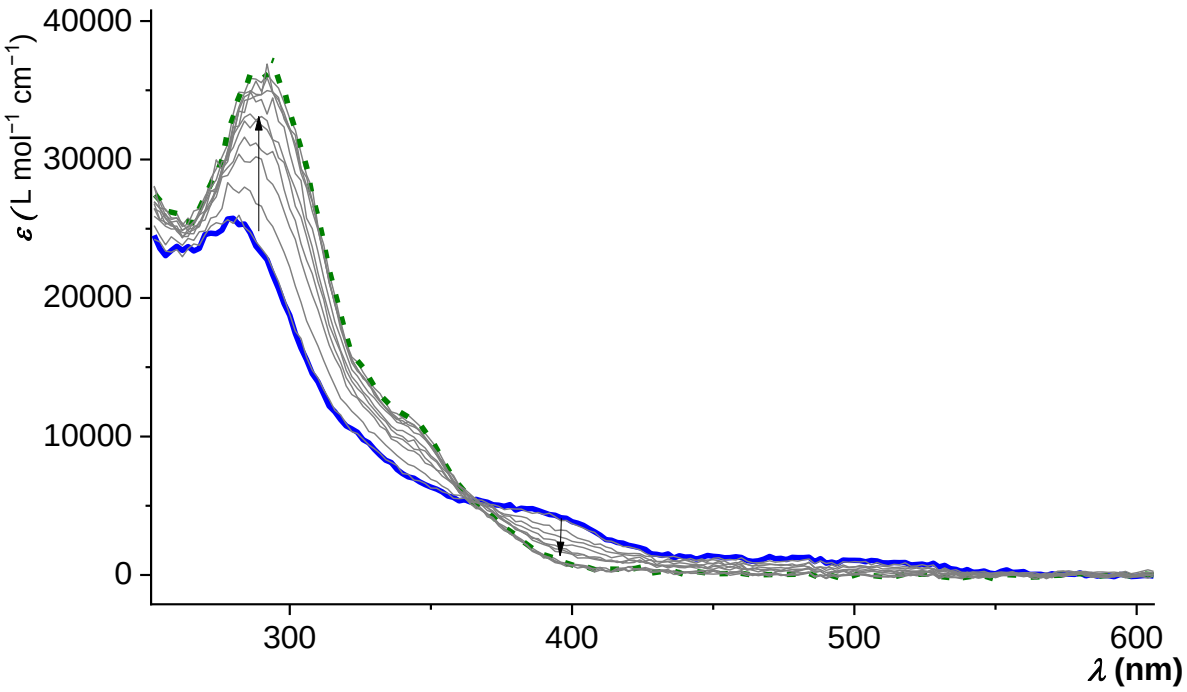

Figure S37. UV–visible spectra of 0.5 mM of complex **1** after CPE at –1.4 V (blue), and after CPE at –0.2 V (green dotted line). Spectra are recorded in CH_3CN with 0.1 M of $TBAPF_6$, in the spectro–electrochemistry cell shown in **Figure S1**.

4.1.2 UV–vis analysis through chemical reduction of complex 1.

Inside the glove box, a 0.5 mM solution of complex **1** in dry CH_3CN is prepared and placed in a sealed cuvette inside the glovebox. The cuvette is taken out and a UV–vis spectrum is recorded. Later, the cuvette is brought inside the glovebox and 1 equivalent of cobaltocene ($CoCp_2$) is added. The cuvette is again sealed and taken to measure by UV–vis. The same procedure is followed when added another equivalent of $CoCp_2$ to the sample. The results are shown in **Figure S38**.

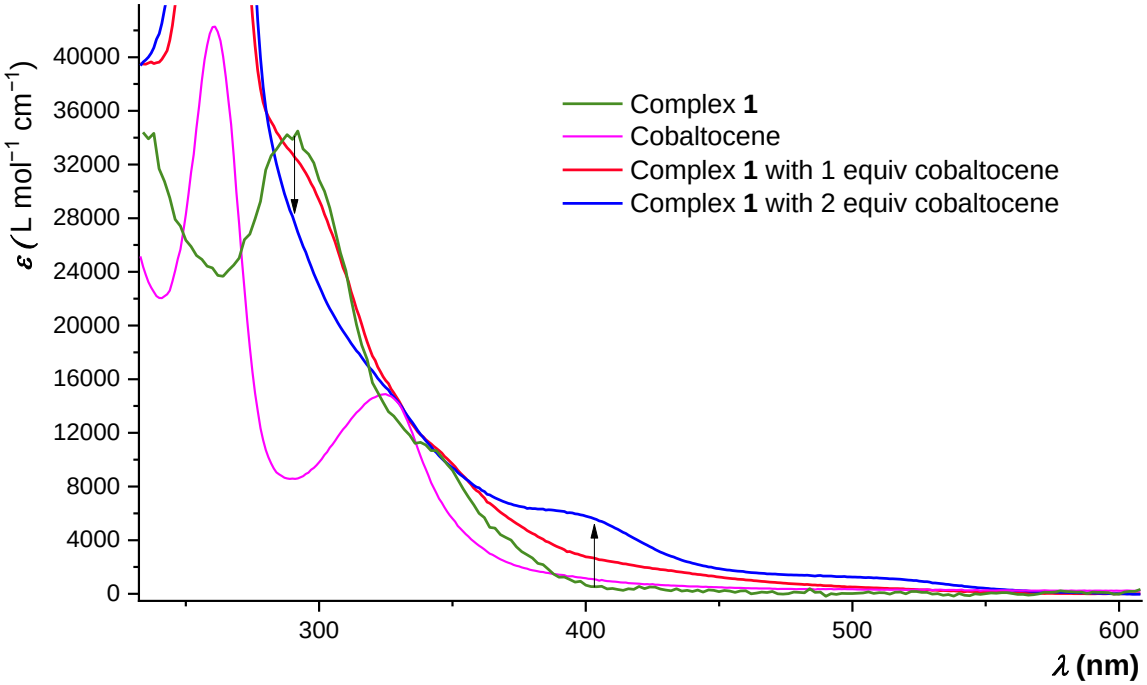

Figure S38. UV–visible spectra of 0.5 mM of complex **1** (green curve); with increasing amount of cobaltocene (1 equiv. red curve, 2 equiv. blue curve); 0.5 mM of $CoCp_2$ (purple curve). The intense band apearing for the red and blue curve corresponds to $CoCp_2^+$. All spectra are recorded in CH_3CN.

5 Electrochemical study of complex 1 under CO_2

5.1 In CH_3CN

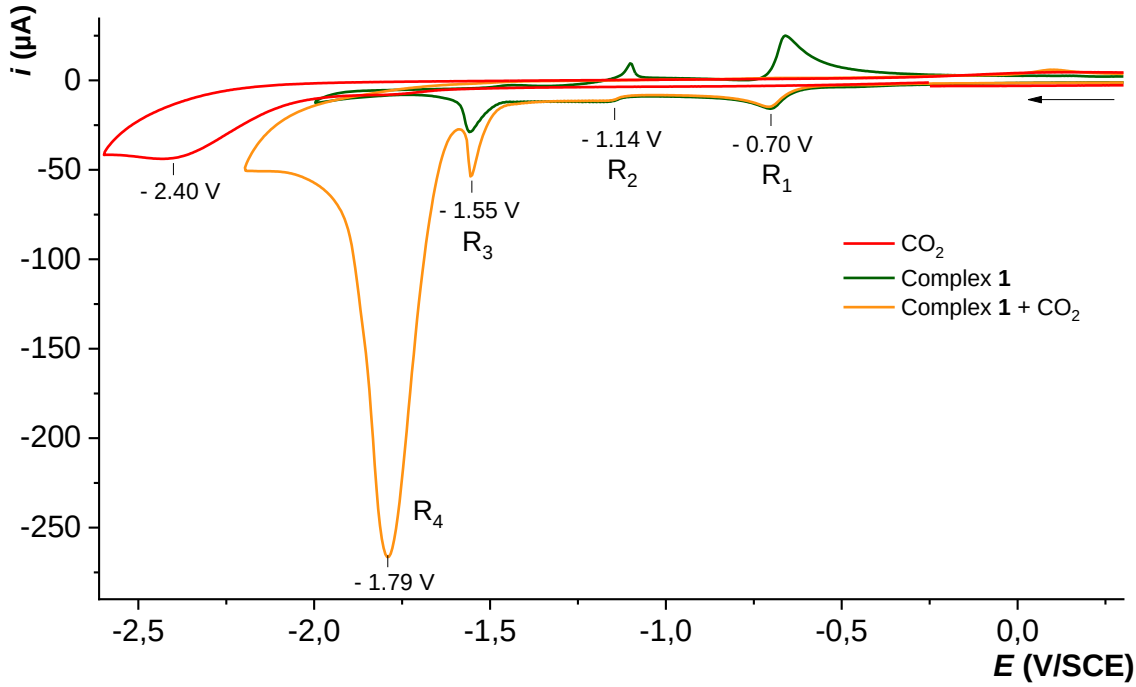

Figure S39. CVs of a saturated solution of CH_3CN with CO_2 (red), with 0.5 mM of complex **1** (orange) and under argon atmosphere (green) in CH_3CN with 0.1 M of $TBAPF_6$. Scan rate of 0.1 $V \cdot s^{-1}$.

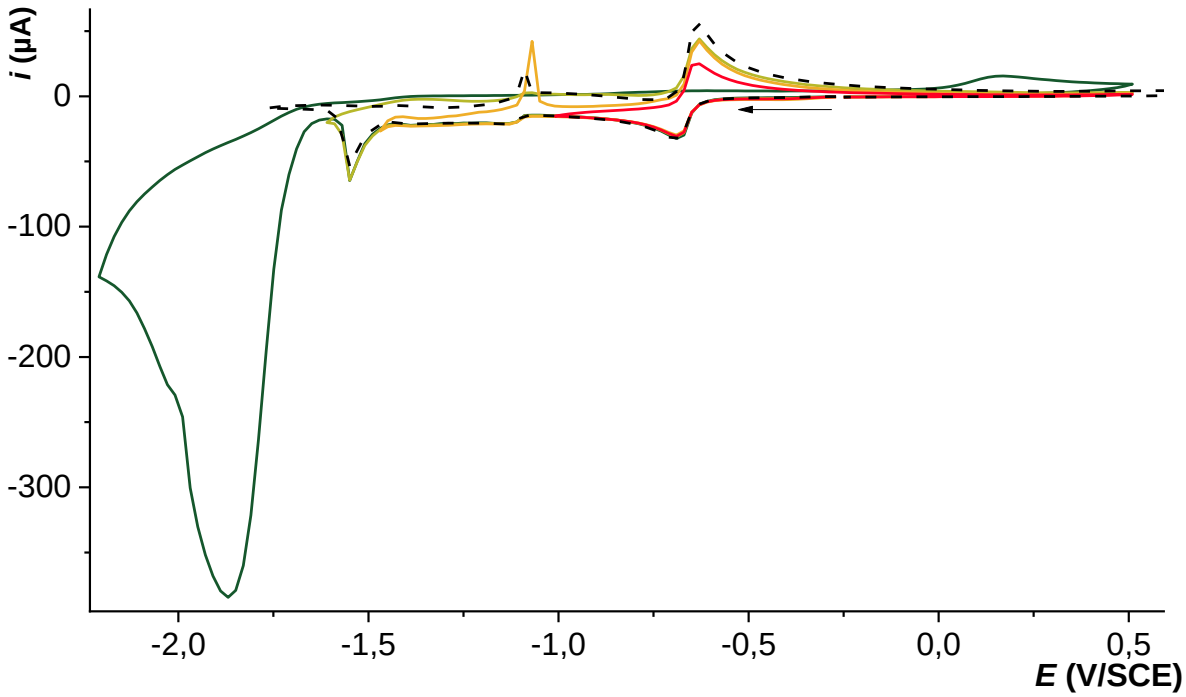

Figure S40. CVs of complex **1** (0.5 mM) under argon (dotted line) and CO_2 (green to red) in anhydrous CH_3CN with 0.1 M of $TBAPF_6$, at 20 °C, scan rate of 0.1 $V \cdot s^{-1}$.

5.2 In DMF

5.2.1 By cyclic voltammetry

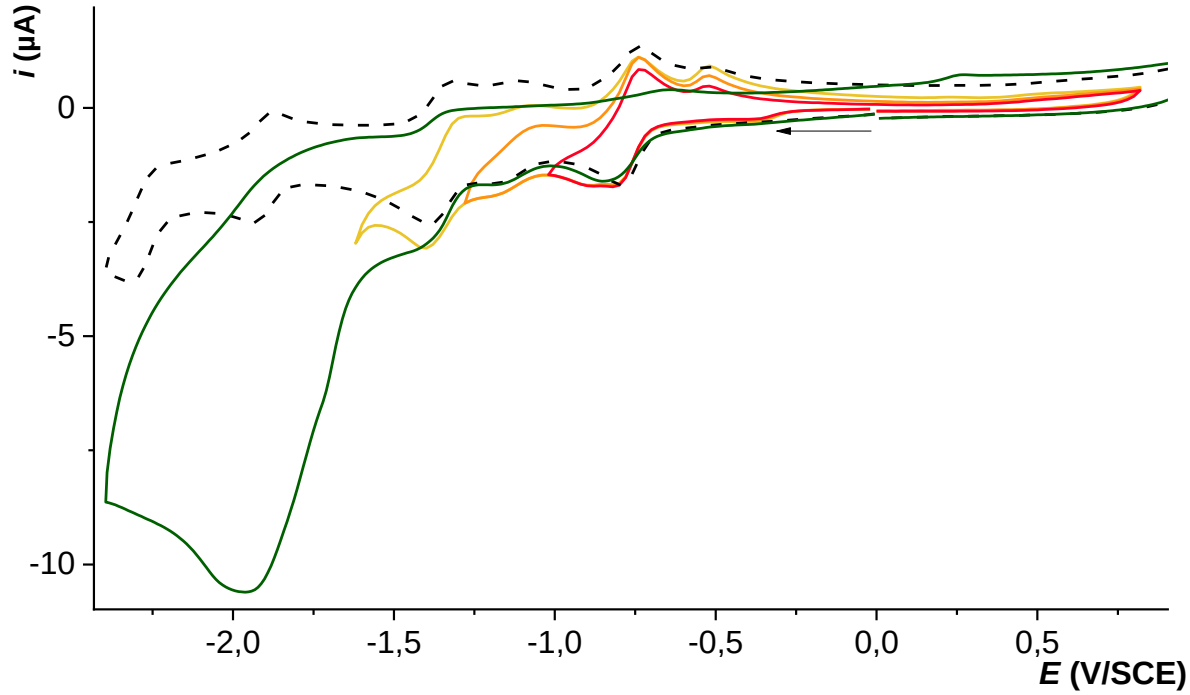

Figure S41. CVs of complex **1** (0.5 mM) under argon (dotted line) and CO_2 (green to red) in anhydrous DMF with 0.1 M of $TBAPF_6$, at 20 °C, scan rate of 0.1 $V \cdot s^{-1}$.

5.2.2 By FT–IR–SpectroElectroChemistry (SEC)

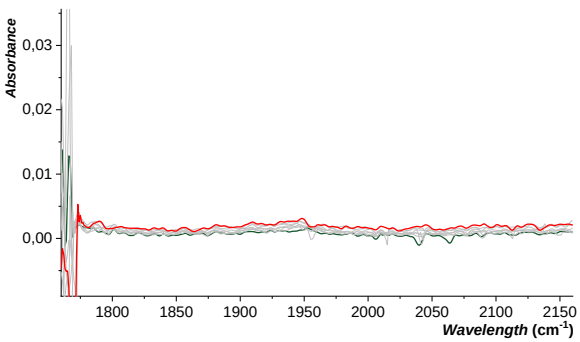

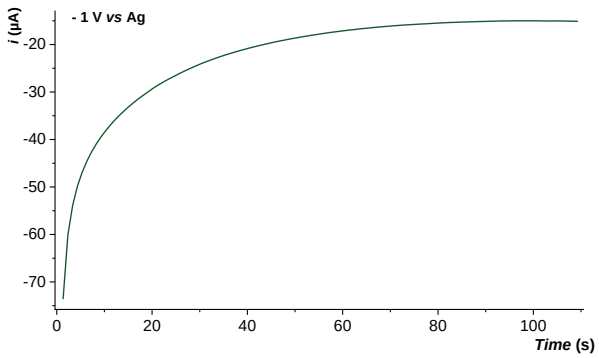

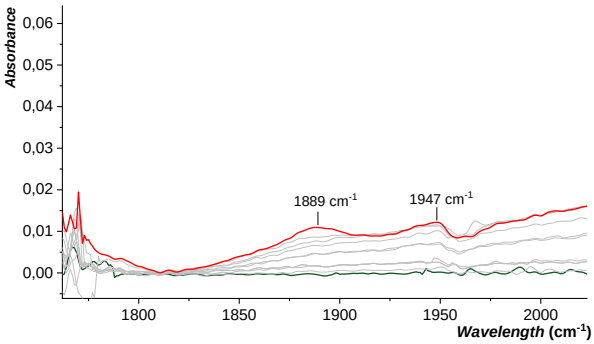
Absorbance
0,06
0,05
0,04
0,03
0,02
0,01
0,00
1889 cm-1
1947 cm-1
1800
1850
1900
1950
2000
Wavelength (cm-1)

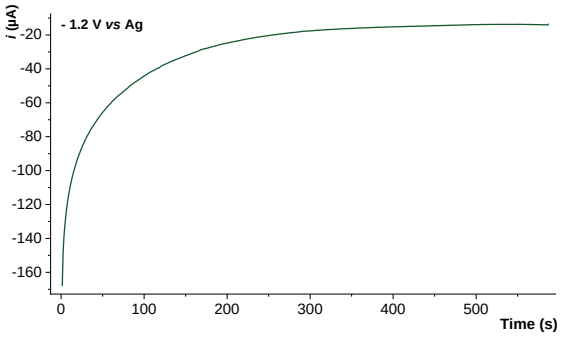
- 1.2 V vs Ag
i (µA)
-20
-40
-60
-80
-100
-120
-140
-160
0
100
200
300
400
500
Time (s)

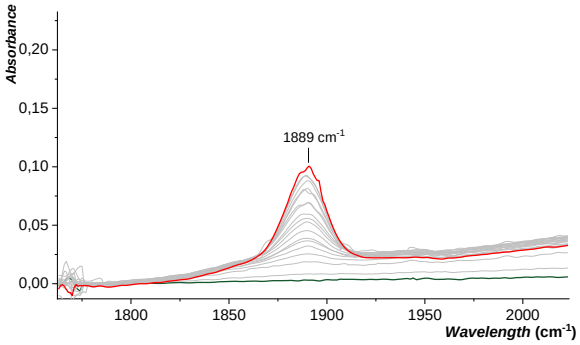
Absorbance
0,20
0,15
0,10
0,05
0,00
1889 cm-1
1800
1850
1900
1950
2000
Wavelength (cm-1)

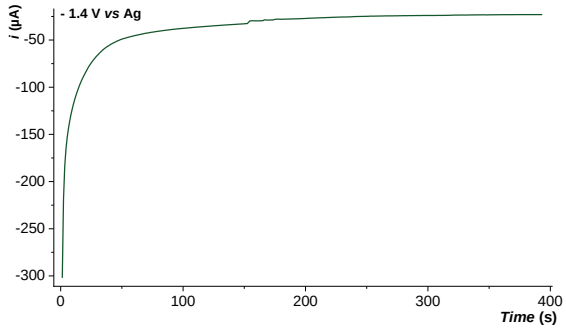
- 1.4 V vs Ag
i (µA)
-50
-100
-150
-200
-250
-300
0
100
200
300
400
Time (s)

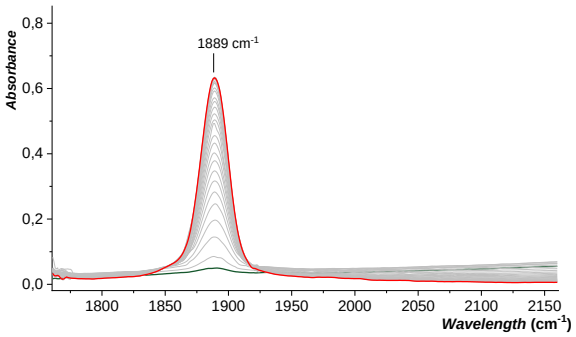
Absorbance
0,8
0,6
0,4
0,2
0,0
1889 cm-1
1800
1850
1900
1950
2000
2050
2100
2150
Wavelength (cm-1)

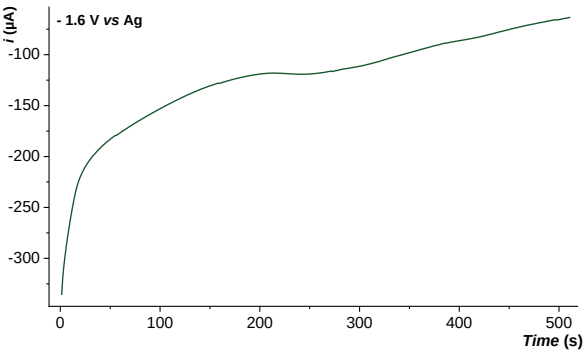
- 1.6 V vs Ag
i (µA)
-100
-150
-200
-250
-300
0
100
200
300
400
500
Time (s)

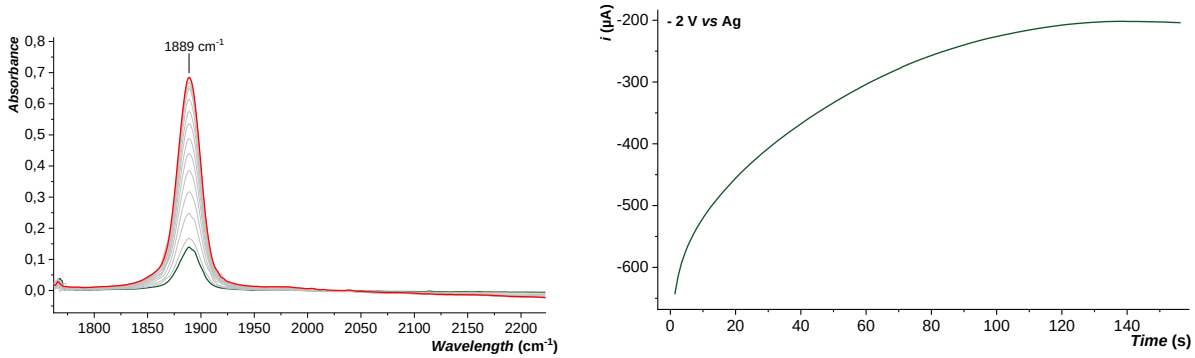

Figure S42. Experimental spectrum obtained by FT–IR–SEC of a 0.5 M $TBAPF_6$/DMF solution of **1** (6 mM) under CO_2 at ca. –1 V to –2 V *vs* Ag wire.

6 Study of complex 1 under CO

6.1 In CH_3CN

6.1.1 By cyclic voltammetry

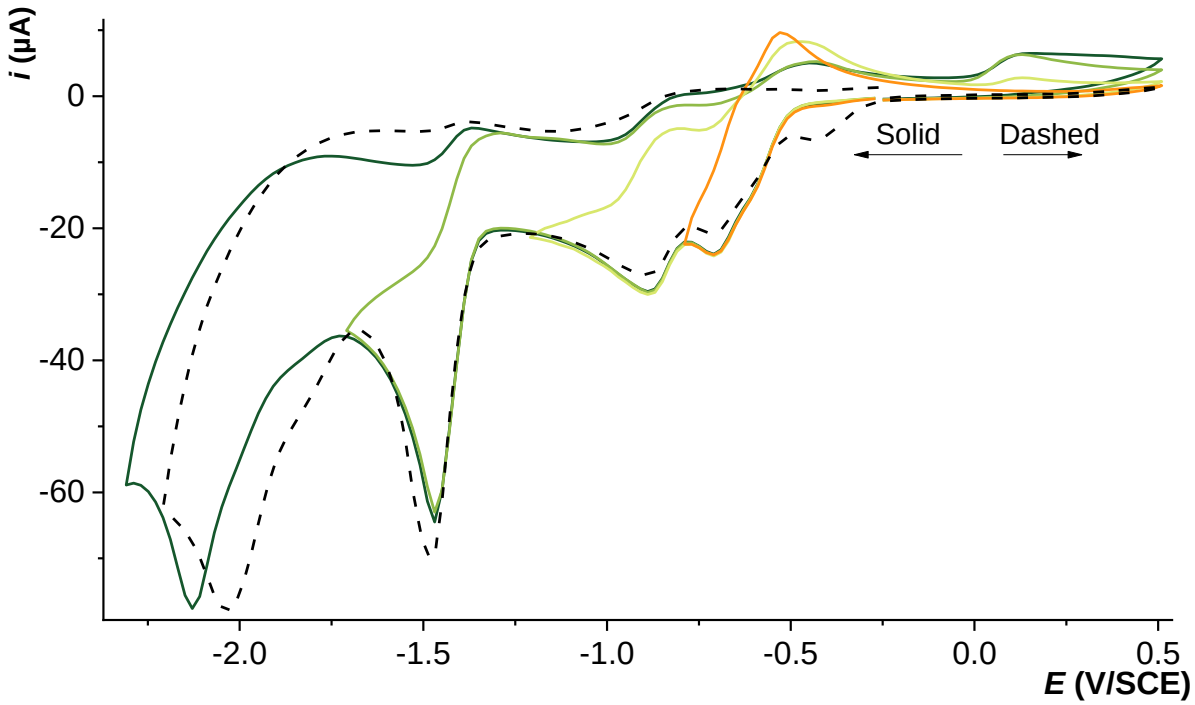

Figure S43. CVs of complex **1** (0.5 mM) under CO in anhydrous CH_3CN with 0.1 M of $TBAPF_6$, scan rate of 0.1 $V \cdot s^{-1}$.

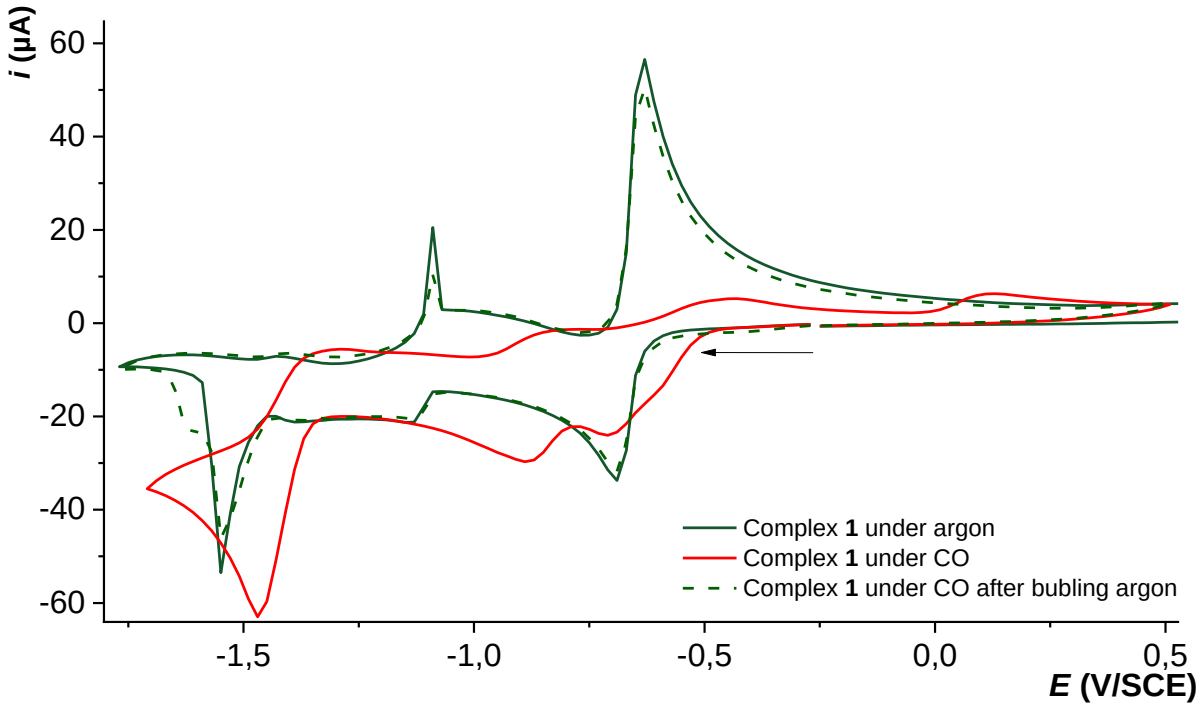

Figure S44. CVs of complex **1** (0.5 mM) under argon (green), under CO (red) and under argon again (dotted line) in anhydrous CH_3CN with 0.1 M of $TBAPF_6$, scan rate of 0.1 $V \cdot s^{-1}$.

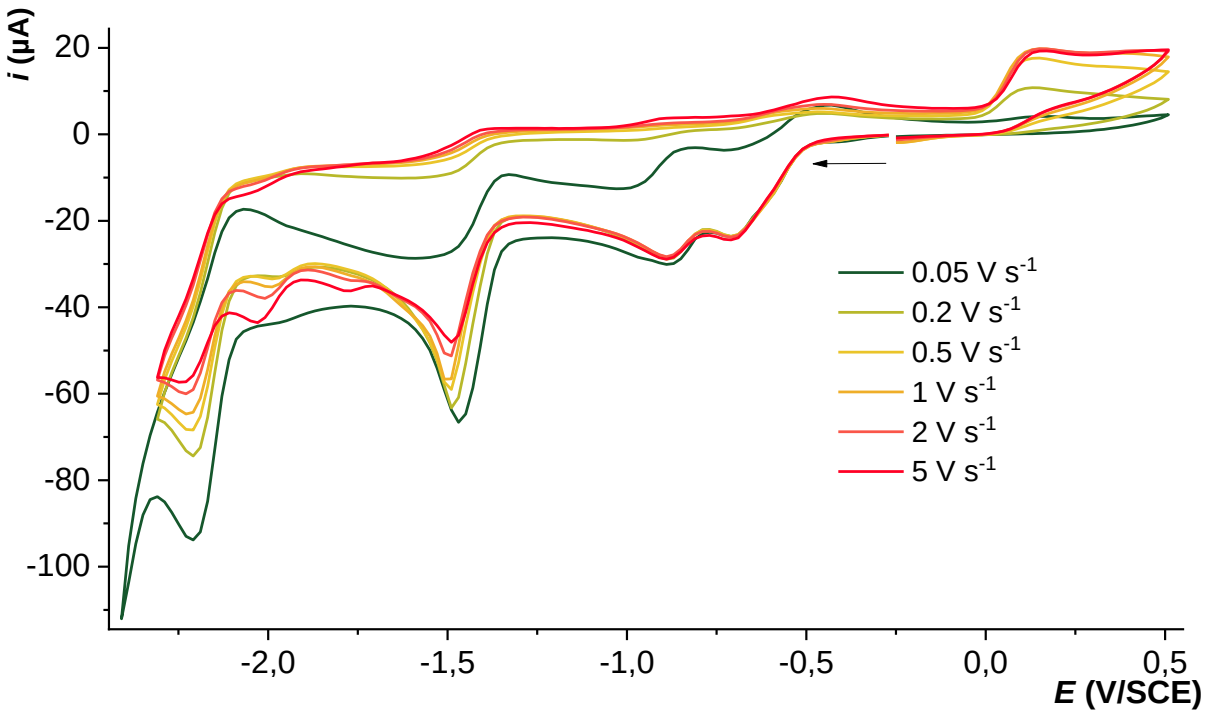

Figure S45. CVs of complex **1** (0.5 mM) under CO in anhydrous CH_3CN with 0.1 M of $TBAPF_6$ at variable scan rates, the CVs are normalized at 0.1 $V \cdot s^{-1}$.

6.2 In DMF

6.2.1 By cyclic voltammetry

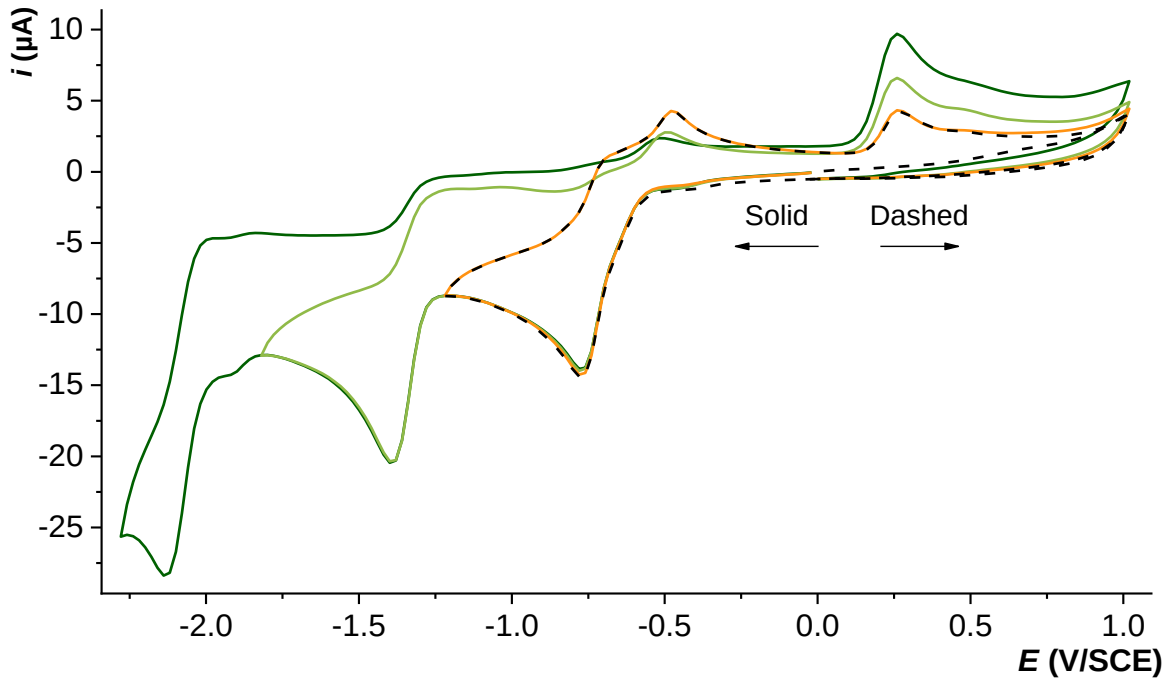

Figure S46. CVs of complex **1** (0.5 mM) under CO in anhydrous DMF with 0.1 M of $TBAPF_6$, scan rate of 0.1 $V \cdot s^{-1}$.

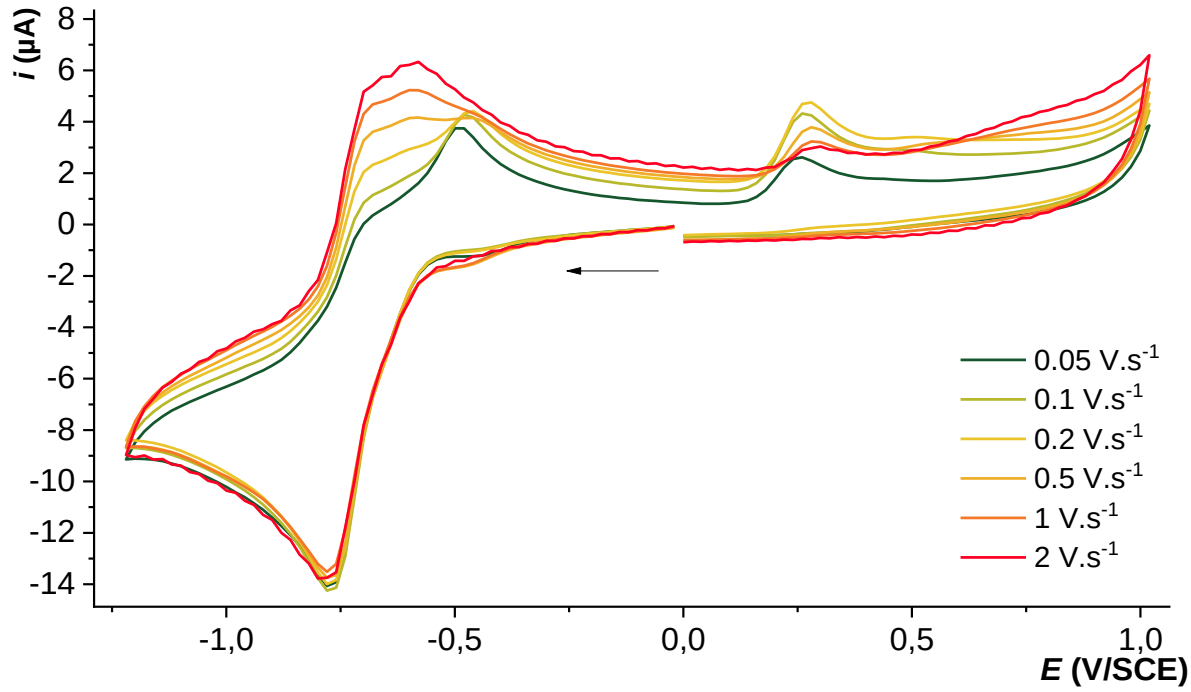

Figure S47. CVs of complex **1** (0.5 mM) under CO in anhydrous DMF with 0.1 M of $TBAPF_6$ at variable scan rates, the CVs are normalized at 0.1 $V \cdot s^{-1}$.

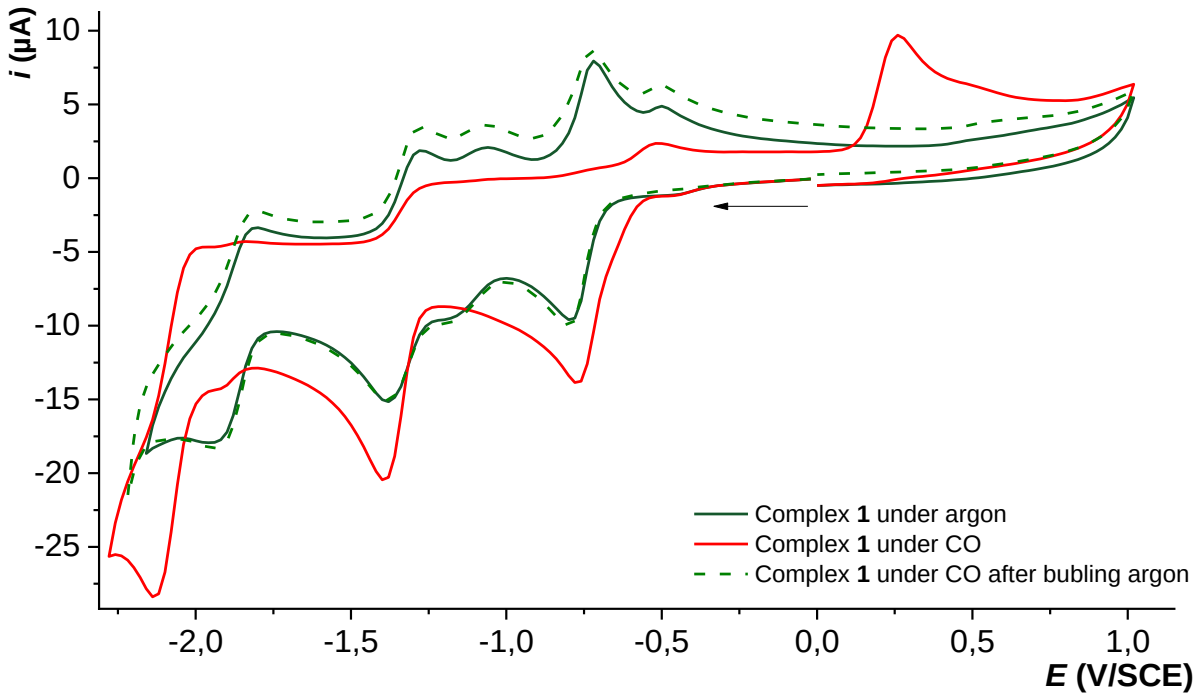

Figure S48. CVs of complex **1** (0.5 mM) under argon (green), under CO (red) and under argon again (dotted line) in anhydrous DMF with 0.1 M of $TBAPF_6$, scan rate of 0.1 $V \cdot s^{-1}$.

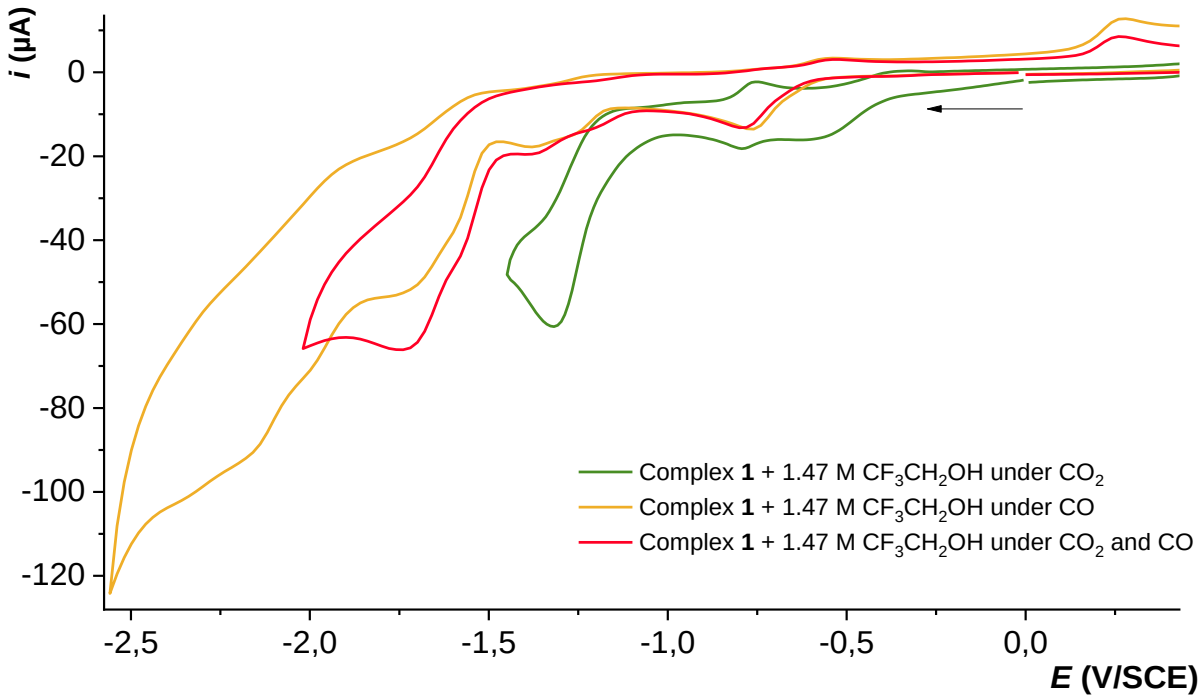

Figure S49. CVs of complex **1** (0.5 mM) under argon, CO_2 and CO in anhydrous DMF with 0.1 M of $TBAPF_6$, scan rate of 0.1 $V \cdot s^{-1}$.

6.2.2 By FT–IR–SpectroElectroChemistry (SEC)

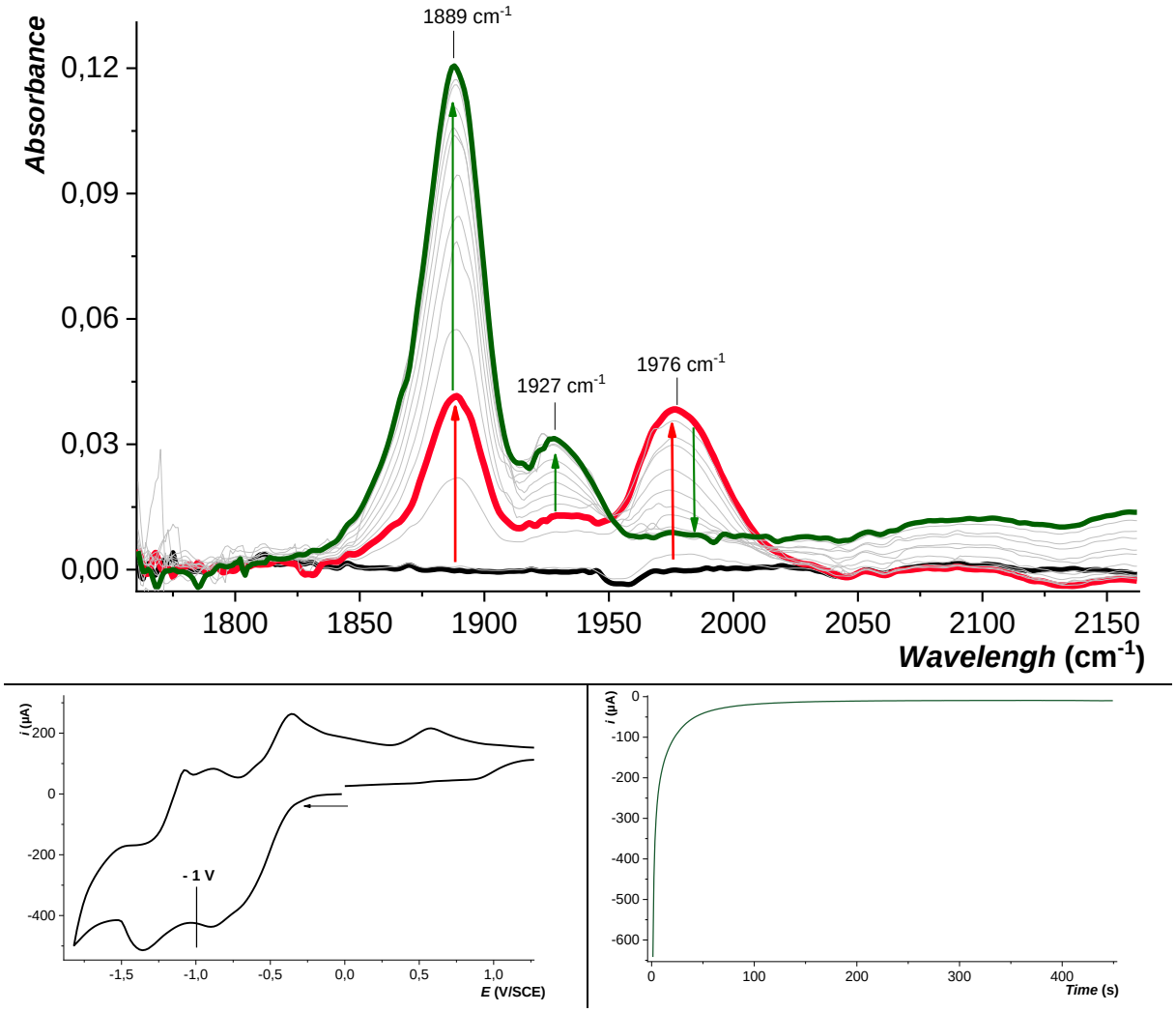

Figure S50. Top, experimental spectrum obtained by FT–IR–SEC of a 0.5 M $TBAPF_6$/DMF solution of **1** (6 mM) under CO at – 1 V *vs* Ag wire. Bottom left, CVs of complex **1** (6 mM) under CO in anhydrous DMF with 0.5 M of $TBAPF_6$, scan rate of 0.1 $V \cdot s^{-1}$, working electrode reference electrode is a microwired Ag electrode, bottom right corresponding chronoamperogram.

7 Effect of a proton source under CO_2 atmosphere

7.1 In CH_3CN

7.1.1 Effect of water as a proton source

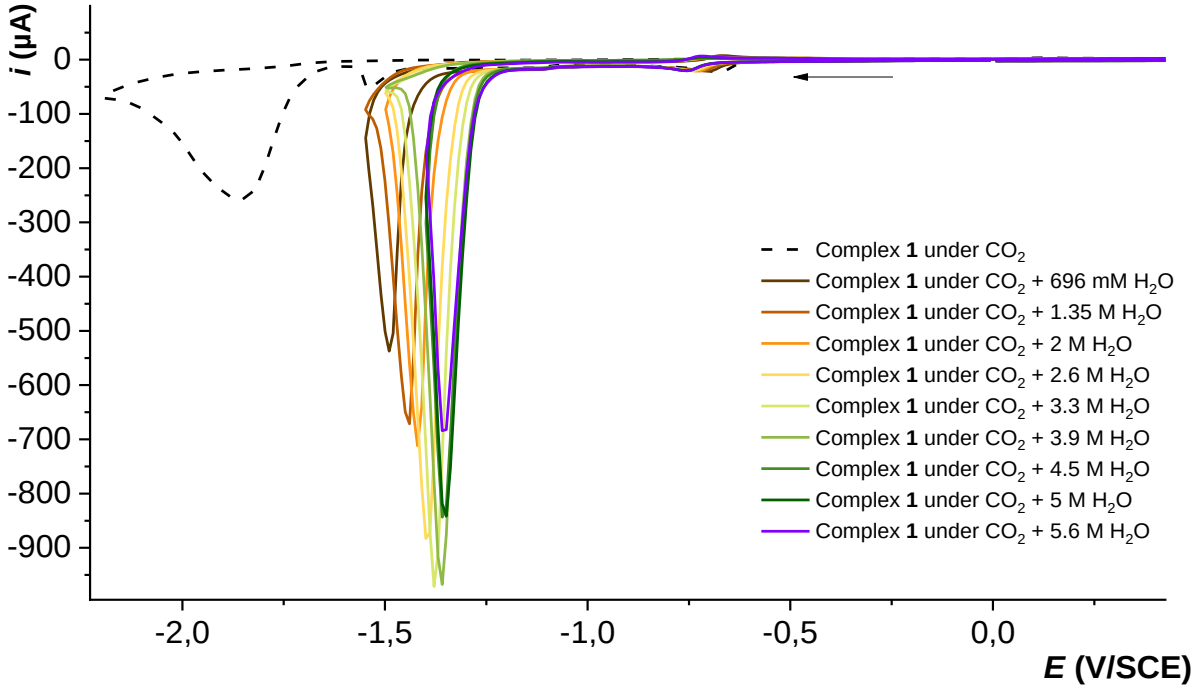

Figure S51. CVs of complex **1** (0.5 mM) in anhydrous CH_3CN with 0.1 M of $TBAPF_6$, at 20 °C under CO_2 with increasing amount of water ; 0 mM (black) to 5.6 M (purple). Scan rate of 0.1 $V \cdot s^{-1}$.

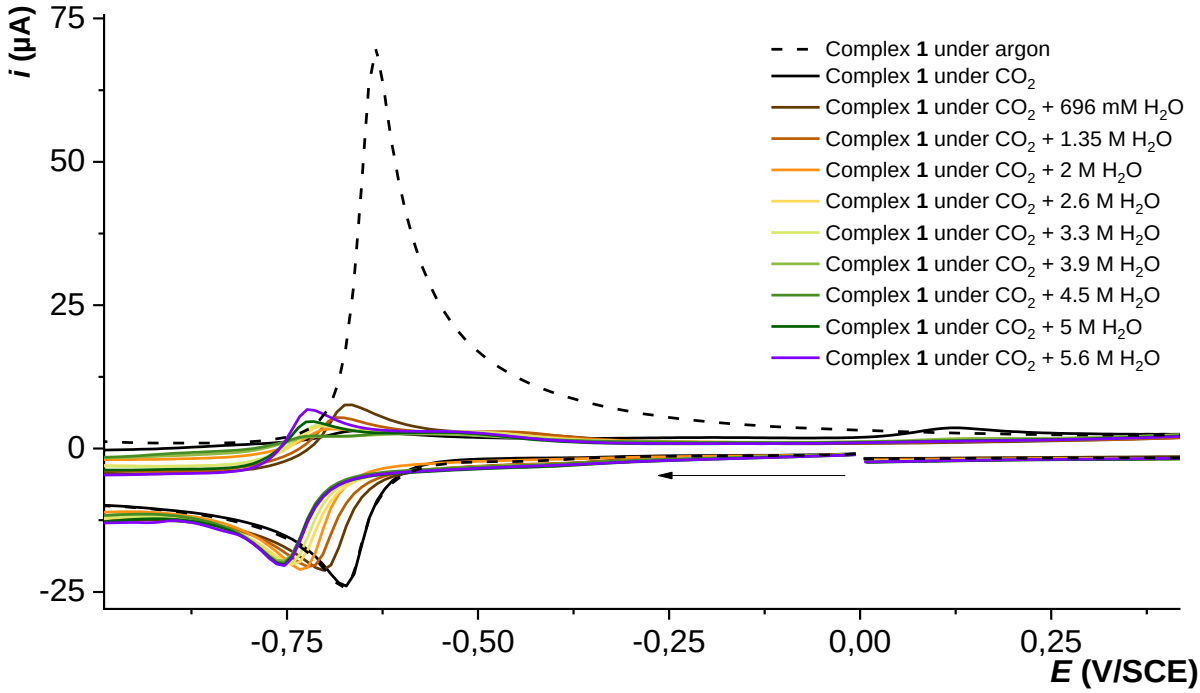

Figure S52. Details of the first cathodic wave for CVs of complex **1** (0.5 mM) in anhydrous CH_3CN with 0.1 M of $TBAPF_6$, at 20 °C under CO_2 with increasing amount of water ; 0 mM (black) to 5.6 M (purple). Scan rate of 0.1 V s^{-1}.

7.1.2 Effect of phenol as a proton source

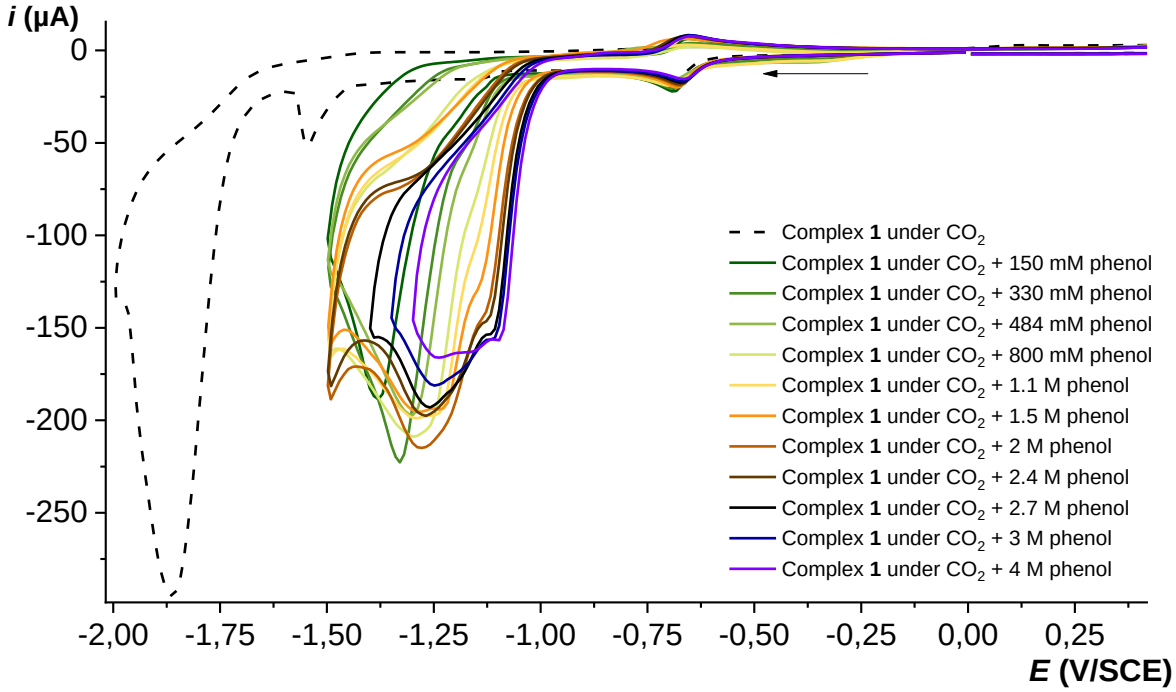

Figure S53. CVs of complex **1** (0.5 mM) under CO_2 in anhydrous CH_3CN with 0.1 M of $TBAPF_6$, at 20 °C with increasing amount of phenol; 1 M (red) to 6 M (cyan). Scan rate of 0.1 $V \cdot s^{-1}$.

7.1.3 Effect of 2,2,2–Trifluoroethanol as a proton source

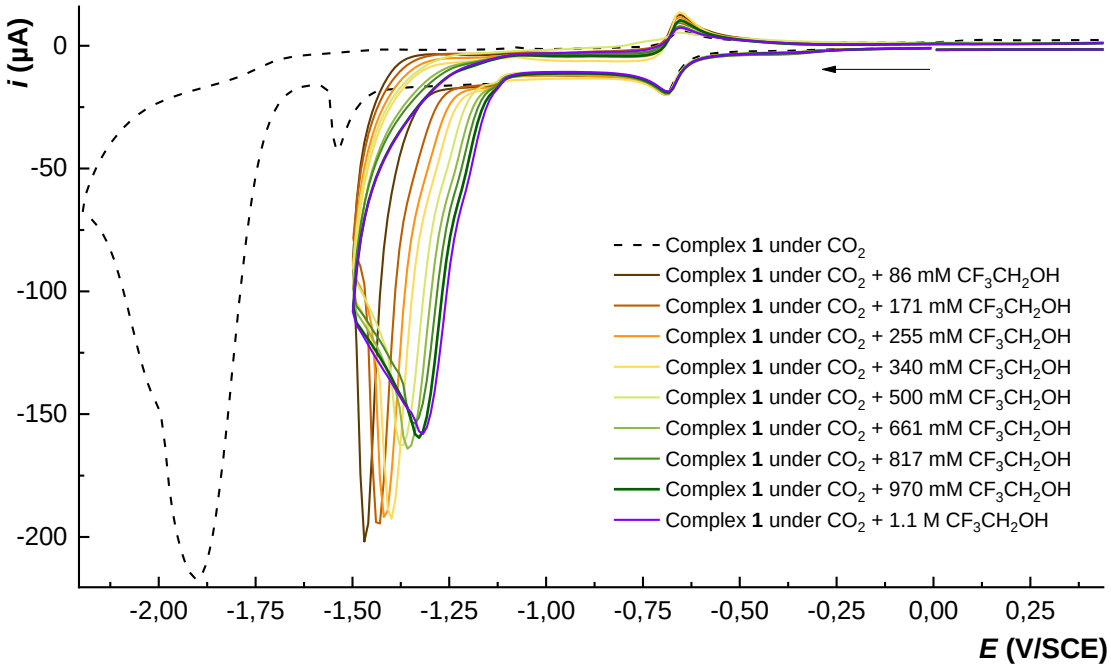

Figure S54. CVs of complex **1** (0.5 mM) under CO_2 in anhydrous CH_3CN with 0.1 M of $TBAPF_6$, at 20 °C with increasing amount of CF_3CH_2OH; 0 mM (black) to 1.1 M (purple). Scan rate of 0.1 $V \cdot s^{-1}$.

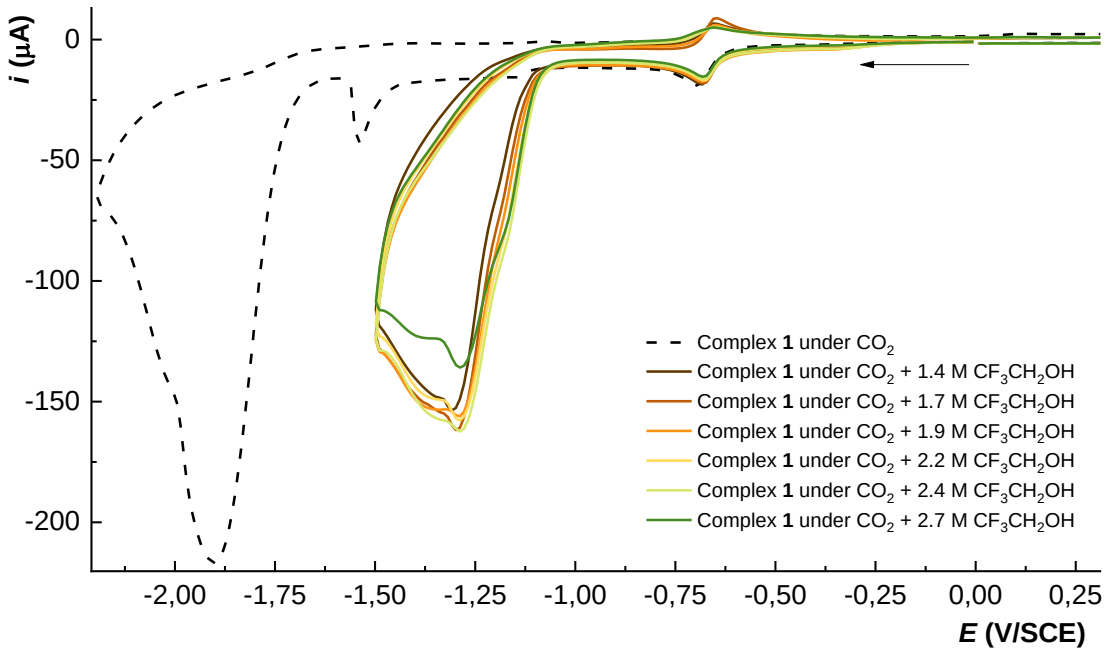

Figure S55. CVs of complex **1** (0.5 mM) under CO_2 in anhydrous CH_3CN with 0.1 M of $TBAPF_6$, at 20 °C with increasing amount of CF_3CH_2OH; 1.4 M (pink) to 2.7 M (green). Scan rate of 0.1 $V \cdot s^{-1}$.

7.2 In DMF

7.2.1 Effect of water as a proton source

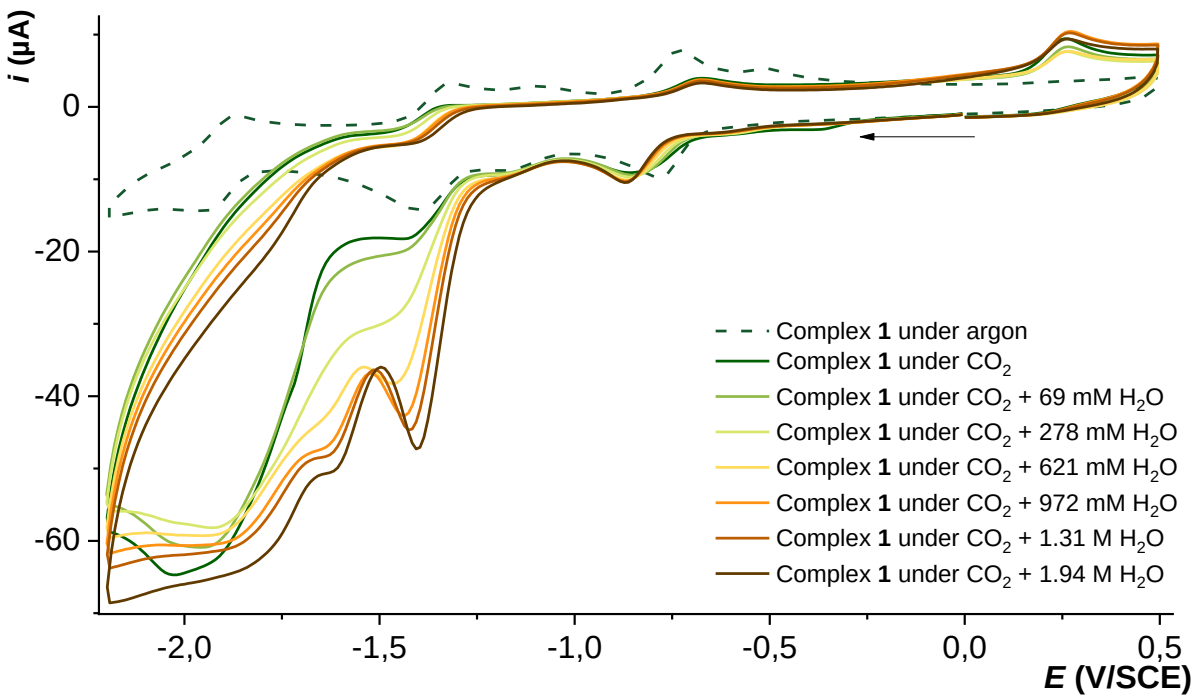

Figure S56. CVs of complex **1** (0.5 mM) under CO_2 in anhydrous DMF with 0.1 M of $TBAPF_6$, at 20 °C (dark green) and with increasing amount of H_2O; 0 mM (green) to 1.94 M (brown). Scan rate of 0.1 $V \cdot s^{-1}$.

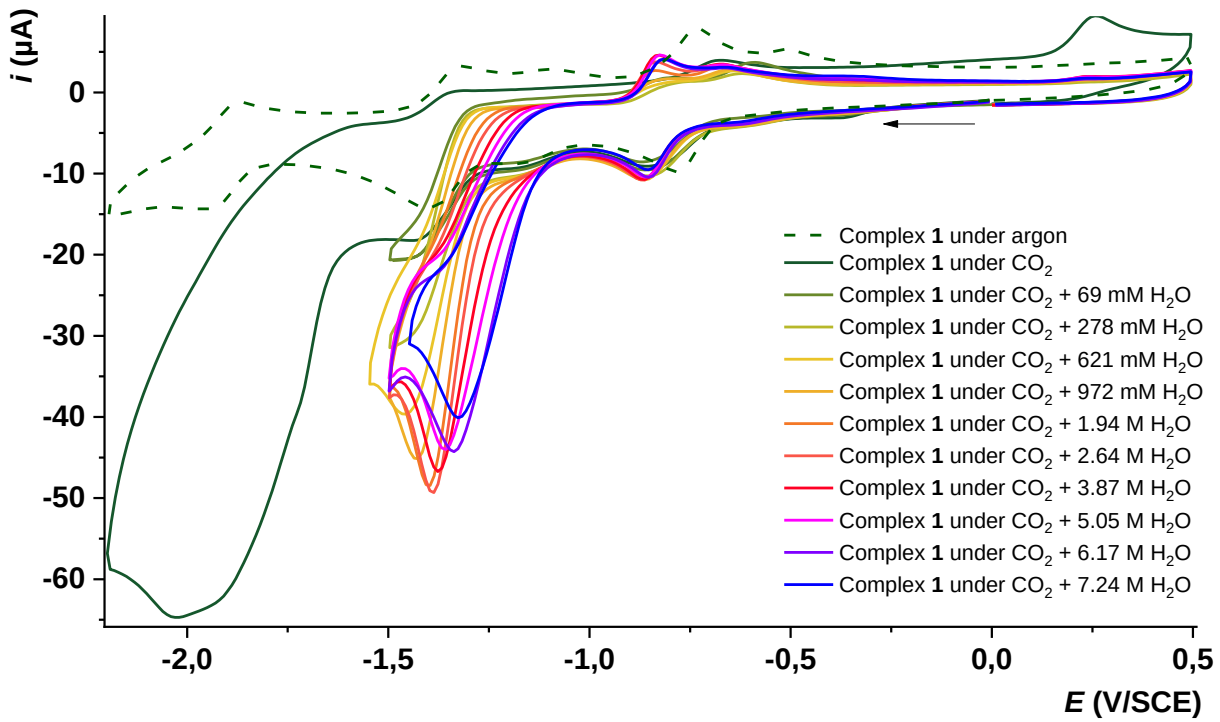

Figure S57. CVs of complex **1** (0.5 mM) under CO_2 in anhydrous DMF with 0.1 M of $TBAPF_6$, at 20 °C (dark green) and with increasing amount of H_2O; 0 mM (green) to 1.7 M (pink). Scan rate of 0.1 $V \cdot s^{-1}$.

7.2.2 Effect of phenol as a proton source

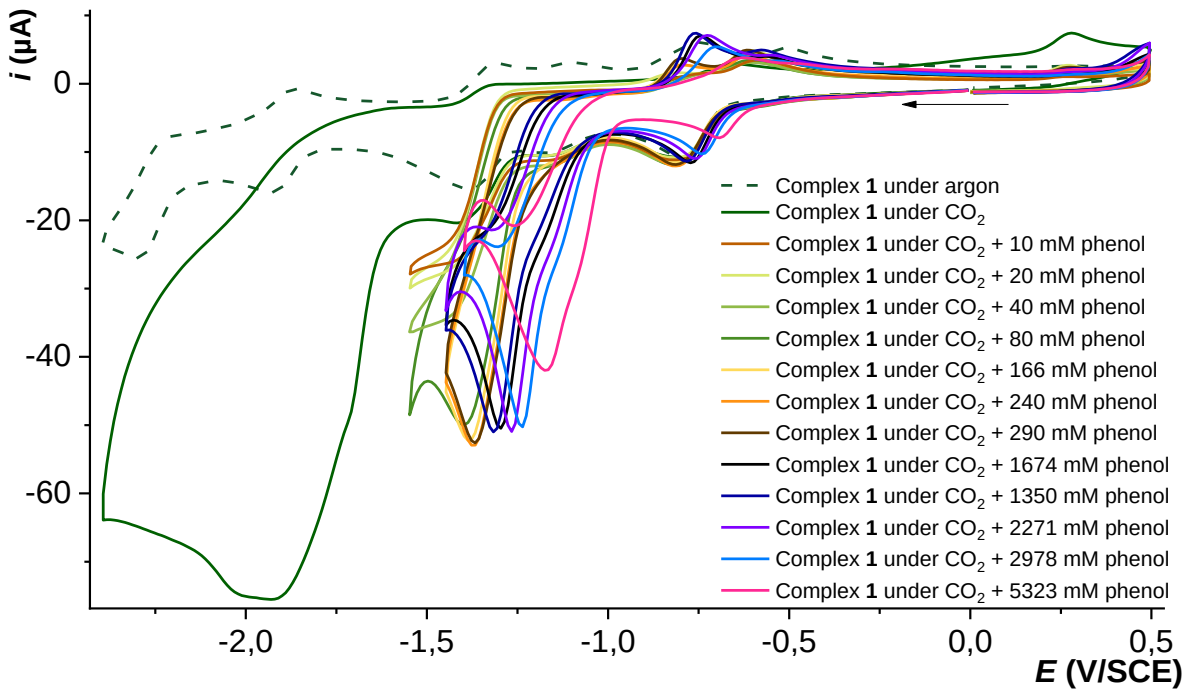

Figure S58. CVs of complex **1** (0.5 mM) under CO_2 in anhydrous DMF with 0.1 M of $TBAPF_6$, at 20 °C (black) and with increasing amount of phenol; 80 mM (brown) to 5.3 M (purple). Scan rate of 0.1 $V \cdot s^{-1}$.

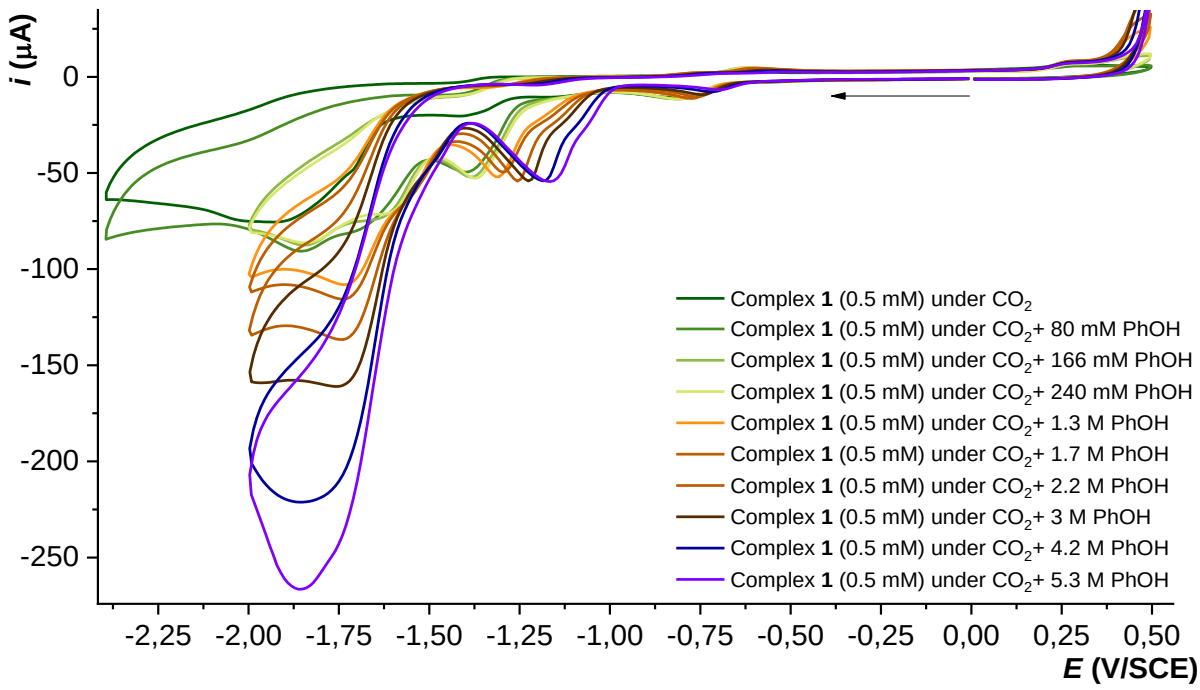

Figure S59. CVs of complex **1** (0.5 mM) under CO_2 in anhydrous DMF with 0.1 M of $TBAPF_6$, at 20 °C (black) and with increasing amount of phenol; 80 mM (brown) to 5.3 M (purple). Scan rate of 0.1 $V \cdot s^{-1}$.

7.2.3 Effect of 2,2,2–Trifluoroethanol as a proton source

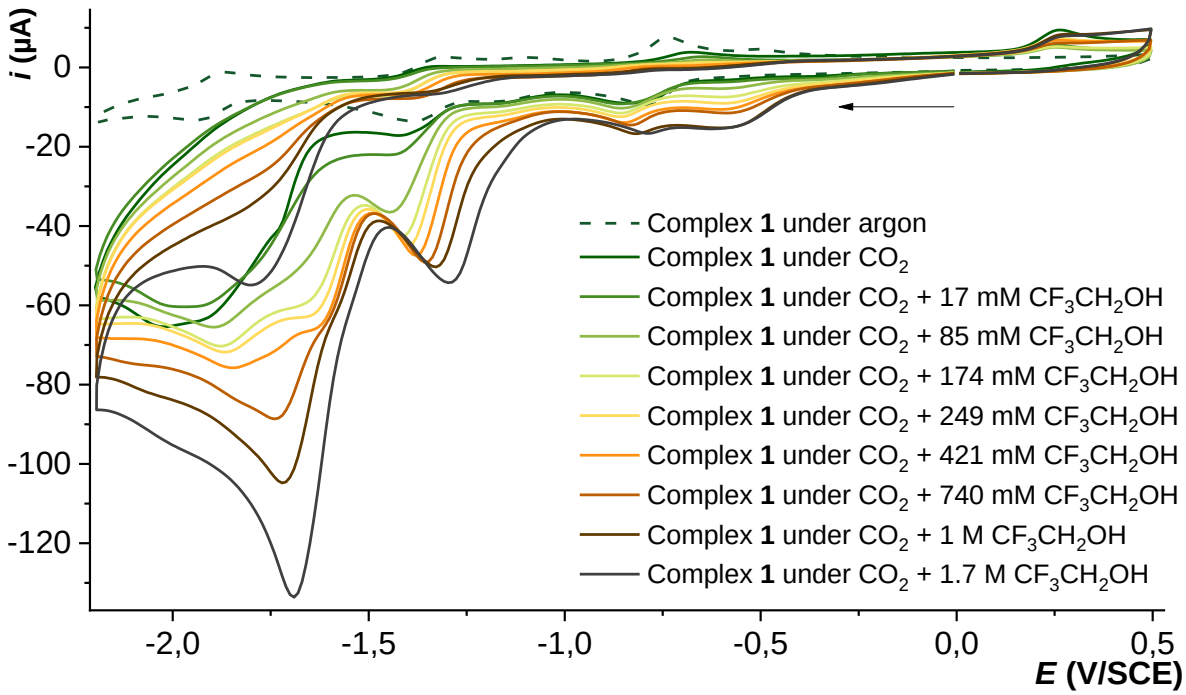

Figure S60. CVs of complex **1** (0.5 mM) under CO_2 in anhydrous DMF with 0.1 M of $TBAPF_6$, at 20 °C (dark green) and with increasing amount of CF_3CH_2OH; 0 mM (purple) to 2 M (pink). Scan rate of 0.1 $V \cdot s^{-1}$.

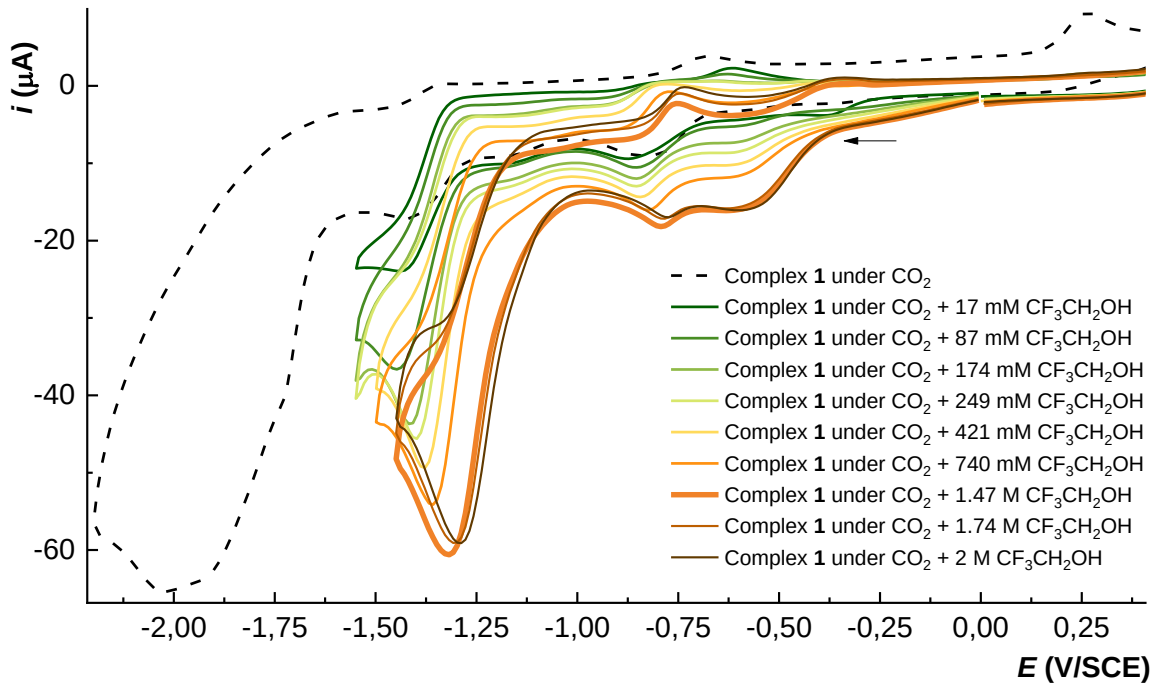

Figure S61. CVs of complex **1** (0.5 mM) under CO_2 in anhydrous DMF with 0.1 M of $TBAPF_6$, at 20 °C (dark green) and with increasing amount of CF_3CH_2OH; 0 mM (purple) to 2 M (pink). Scan rate of 0.1 $V \cdot s^{-1}$.

8 Controlled Potential Electrolyses (CPE)

8.1 CPE under CO_2

	CH_3CN		DMF	
Applied potential (V/SCE)	–1.95		–2.05	
Charge passed (C)	–12.9		–3.9	
Quantity of catalyst (mol)	2.10^{-6}		2.10^{-6}	
Current density (mA/cm²)	0.77		0.18	
Time (s)	8300		10800	
	CO	H_2	CO	H_2
Quantity (mol)	$5.7 \cdot 10^{-7}$	0	$2.8 \cdot 10^{-7}$	0
Faradic Efficiency (%)	1	0	1	0
TON	0.3	0	0.1	0

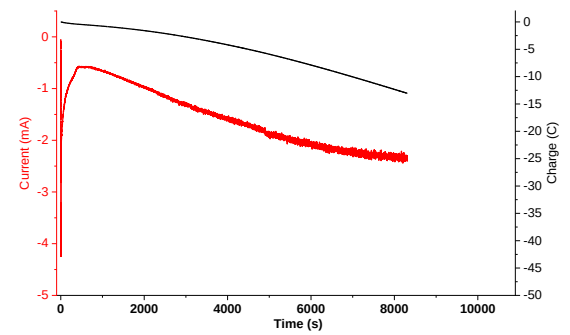

a

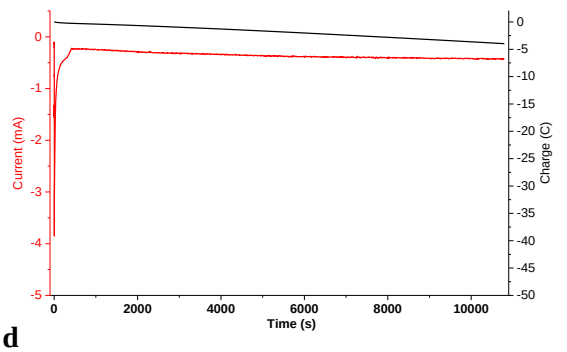

d

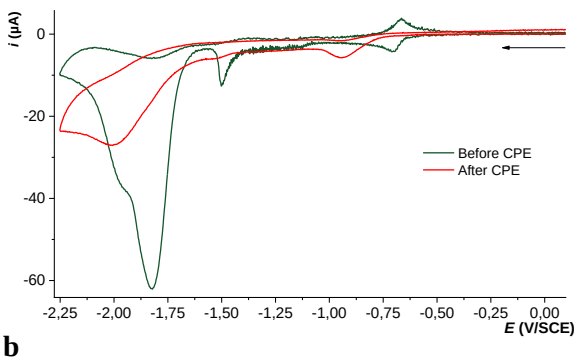

b

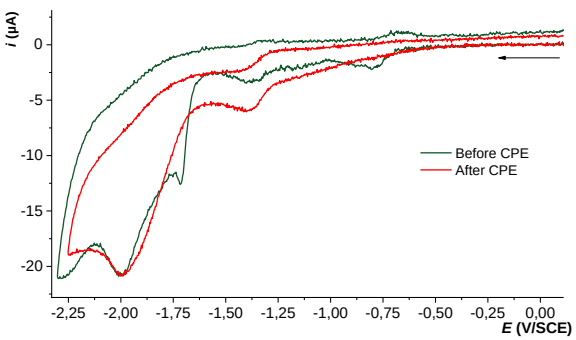

e

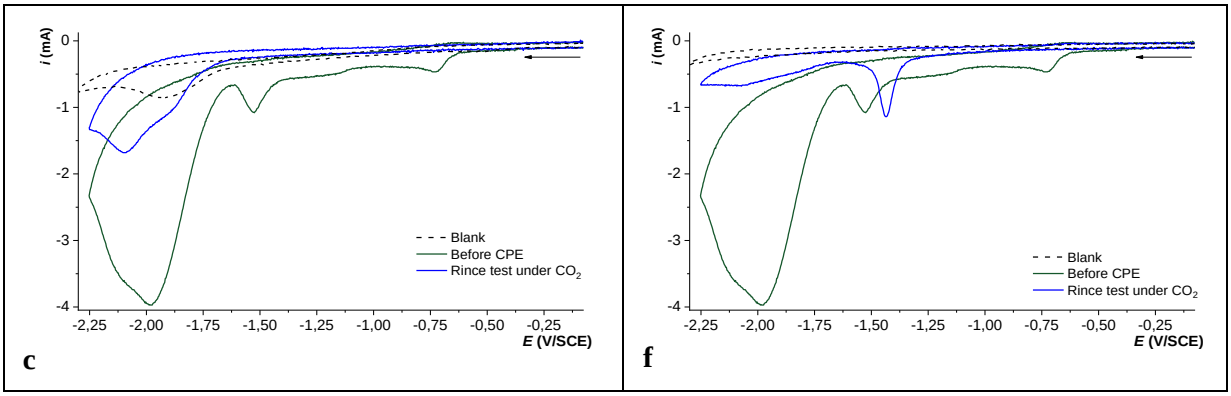

Table S3. a) Current (red) and charge (black) overtime during CPE experiments of complex **1** (0.5 mM) in anhydrous CH_3CN under CO_2. **b)** CVs of complex **1** (0.5 mM) under CO_2 in anhydrous CH_3CN before CPE (green) and after CPE (red). Glassy carbon electrode of 0.03 cm² area, scan rate of 0.1 $V \cdot s^{-1}$. **c)** CVs of a saturated solution of CO_2 in anhydrous CH_3CN (black dashed) of complex **1** (0.5 mM) under CO_2 in anhydrous CH_3CN before CPE (green) and after CPE with the same glassy carbon plate in a solution without catalyst in CH_3CN under CO_2 (blue). Glassy carbon plate of 2 cm² area, scan rate of 0.1 $V \cdot s^{-1}$. **d)** Current (red) and charge (black) overtime during CPE experiments of complex **1** (0.5 mM) in anhydrous DMF under CO_2. **e)** CVs of complex **1** (0.5 mM) under CO_2 in anhydrous DMF before CPE (green) and after CPE (red). Glassy carbon electrode of 0.03 cm² area, scan rate of 0.1 $V \cdot s^{-1}$. **f)** CVs of a saturated solution of CO_2 in anhydrous DMF (black dashed) of complex **1** (0.5 mM) under CO_2 in anhydrous DMF before CPE (green) and after CPE with the same glassy carbon plate in a solution without catalyst in DMF under CO_2 (blue). Glassy carbon plate of 2 cm² area, scan rate of 0.1 $V \cdot s^{-1}$.

8.2 CPE under CO_2 in the presence of water

CH_3CN			**DMF**	
Applied potential (V/SCE)	–1.47		–1.4	
Charge passed (C)	–30		–14.5	
Quantity of catalyst (mol)	$2.3 \cdot 10^{-6}$		3.10^{-6}	
Current density (mA/cm²)	1.4		0.7	
Time (s)	10800		10800	
	CO	H_2	CO	H_2
Quantity (mol)	$1.5 \cdot 10^{-6}$	$1.6 \cdot 10^{-6}$	$1.3 \cdot 10^{-5}$	$1.6 \cdot 10^{-5}$
Faradic Efficiency (%)	1	1	18	21
TON	0.6	0.7	4	5

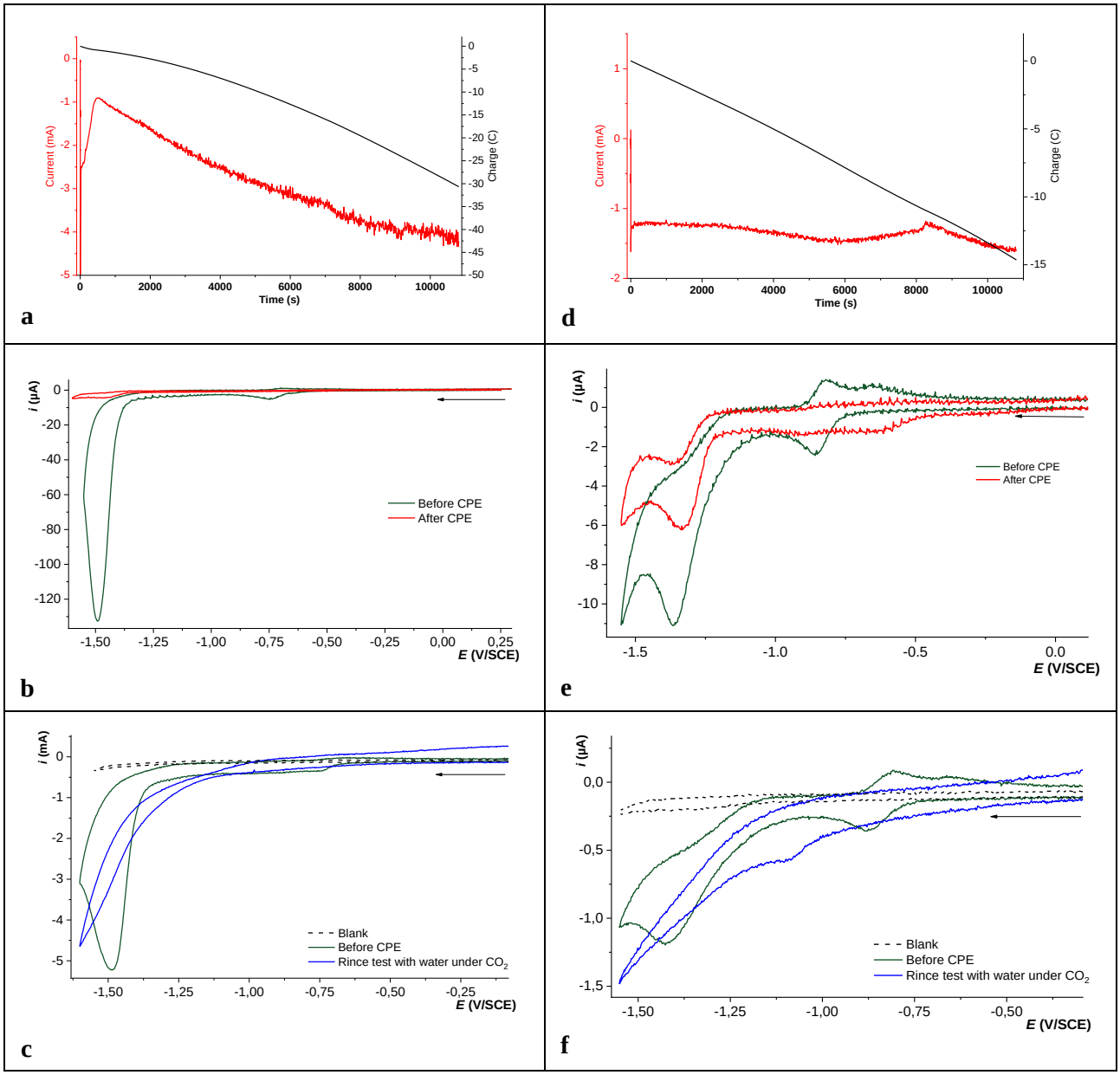

Table S4. a) Current (red) and charge (black) overtime during CPE experiments of complex **1** (0.5 mM) in anhydrous CH_3CN under CO_2 with 1.6 M of water. **b)** CVs of complex **1** (0.5 mM) under CO_2 in anhydrous CH_3CN with 1.6 M of water before CPE (green) and after CPE (red). Glassy carbon electrode of 0.03 cm² area, scan rate of 0.1 $V \cdot s^{-1}$. **c)** CVs of a saturated solution of CO_2 in anhydrous CH_3CN with 1.6 M of water (black dashed) of complex 1 (0.5 mM) under CO_2 in anhydrous CH_3CN with 1.6 M of water before CPE (green) and after CPE with the same glassy carbon plate in a solution without catalyst with 1.6 M of water in CH_3CN under CO_2 (blue). Glassy carbon plate of 2 cm² area, scan rate of 0.1 $V \cdot s^{-1}$. **d)** Current (red) and charge (black) overtime during CPE experiments of complex **1** (0.5 mM) in anhydrous DMF under CO_2 with 5 M of water. **e)** CVs of complex **1** (0.5 mM) under CO_2 in anhydrous DMF with 5 M of water before CPE (green) and after CPE (red). Glassy carbon electrode of 0.03 cm² area, scan rate of 0.1 $V \cdot s^{-1}$. **f)** CVs of complex **1** (0.5 mM) under CO_2 in anhydrous DMF with 5 M of water before CPE (green) and after CPE with the same glassy carbon plate in a solution without catalyst with 5 M of water in DMF under CO_2 (blue). Glassy carbon plate of 2 cm² area, scan rate of 0.1 $V \cdot s^{-1}$.

8.3 CPE under CO_2 in the presence of phenol

	CH_3CN		DMF	
Applied potential (V/SCE)	–1.3		–1.3	
Charge passed (C)	–36.7		–11.9	
Quantity of catalyst (mol)	$2.4 \cdot 10^{-6}$		2.10^{-6}	
Current density (mA/cm²)	1.7		0.55	
Time (s)	10800		10800	
	CO	H_2	CO	H_2
Quantity (mol)	$4.3 \cdot 10^{-6}$	$1.5 \cdot 10^{-7}$	$2.5 \cdot 10^{-5}$	$6.8 \cdot 10^{-6}$
Faradic Efficiency (%)	2	0	41	11
TON	2	0	12	3

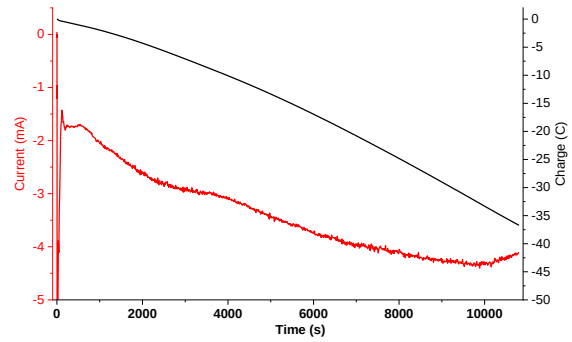

a

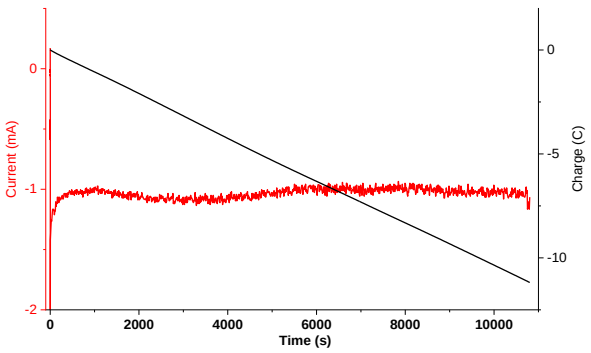

d

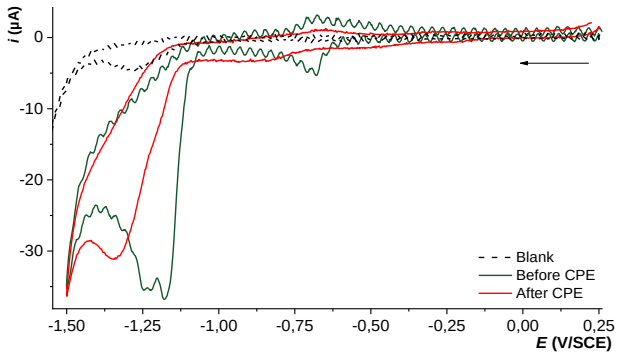

b

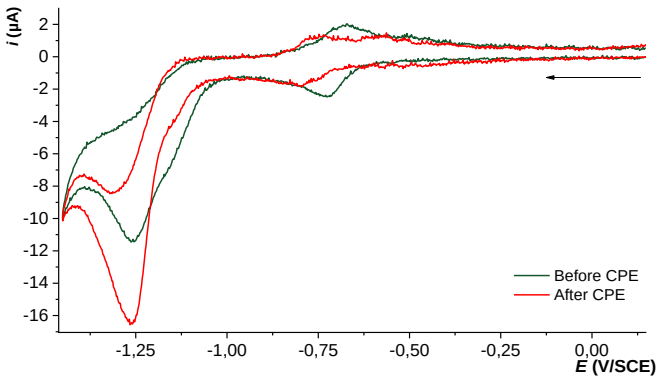

e

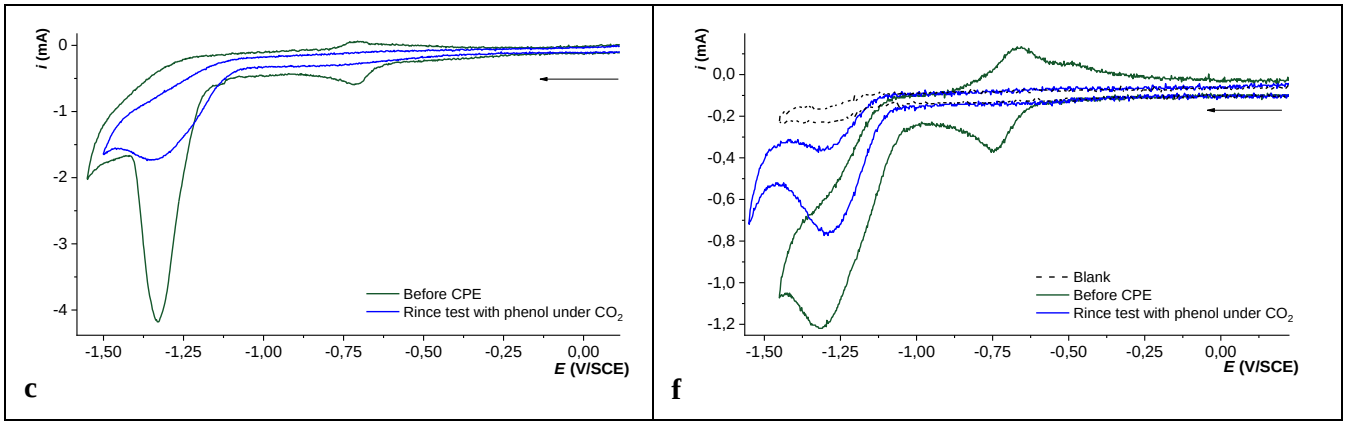

Table S5. a) Current (red) and charge (black) overtime during CPE experiments of complex **1** (0.5 mM) in anhydrous CH_3CN under CO_2 with 1.6 M of phenol. **b)** CVs of complex **1** (0.5 mM) under CO_2 in anhydrous CH_3CN with 1.6 M of phenol before CPE (green) and after CPE (red). Glassy carbon electrode of 0.03 cm² area, scan rate of 0.1 $V \cdot s^{-1}$. **c)** CVs of complex **1** (0.5 mM) under CO_2 in anhydrous CH_3CN with 1.6 M of phenol before CPE (green) and after CPE with the same glassy carbon plate in a solution without catalyst with 1.6 M of phenol in CH_3CN under CO_2 (blue). Glassy carbon plate of 2 cm² area, scan rate of 0.1 $V \cdot s^{-1}$. **d)** Current (red) and charge (black) overtime during CPE experiments of complex **1** (0.5 mM) in anhydrous DMF under CO_2 with 3 M of phenol. **e)** CVs of complex **1** (0.5 mM) under CO_2 in anhydrous DMF with 3 M of phenol before CPE (green) and after CPE (red). Glassy carbon electrode of 0.03 cm² area, scan rate of 0.1 $V \cdot s^{-1}$. **f)** CVs of a saturated solution of CO_2 in anhydrous DMF with 3 M of phenol (black dashed) of complex **1** (0.5 mM) under CO_2 in anhydrous DMF with 3 M of phenol before CPE (green) and after CPE with the same glassy carbon plate in a solution without catalyst with 3 M of phenol in DMF under CO_2 (blue). Glassy carbon plate of 2 cm² area, scan rate of 0.1 $V \cdot s^{-1}$.

8.4 CPE under CO_2 in the presence of phenol and CF_3CH_2OH at the second cathodic wave

Phenol			CF_3CH_2OH	
Applied potential (V/SCE)	–1.8		–1.8	
Charge passed (C)	26.4		8.6	
Quantity of catalyst (mol)	$1.8 \cdot 10^{-6}$		$2.2 \cdot 10^{-6}$	
Current density (mA/cm²)	1.2		0.7	
Time (s)	10800		5772	
	CO	H_2	CO	H_2
Quantity (mol)	$2.2 \cdot 10^{-5}$	$2.3 \cdot 10^{-5}$	$1.1 \cdot 10^{-5}$	$3.5 \cdot 10^{-6}$
Faradic Efficiency (%)	16	17	25	8
TON	12	13	5	1.5

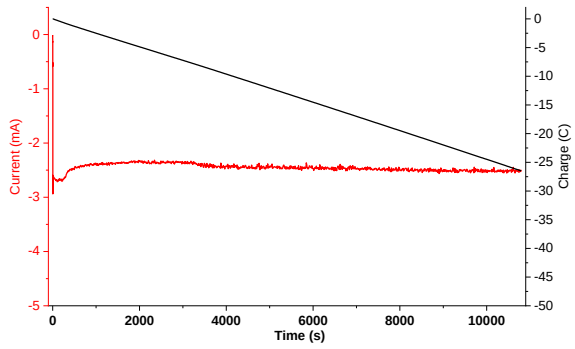

a

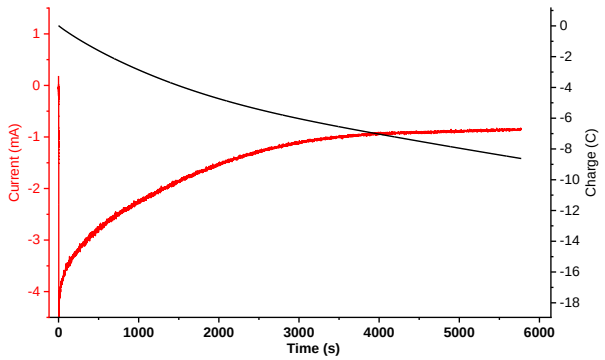

d

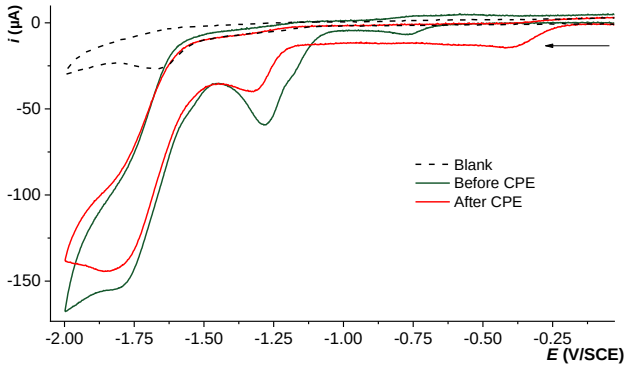

b

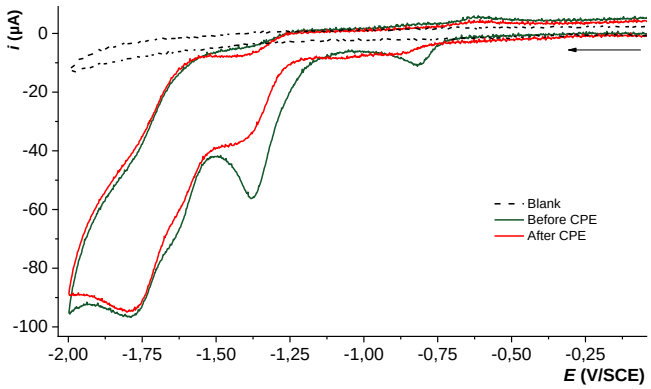

e

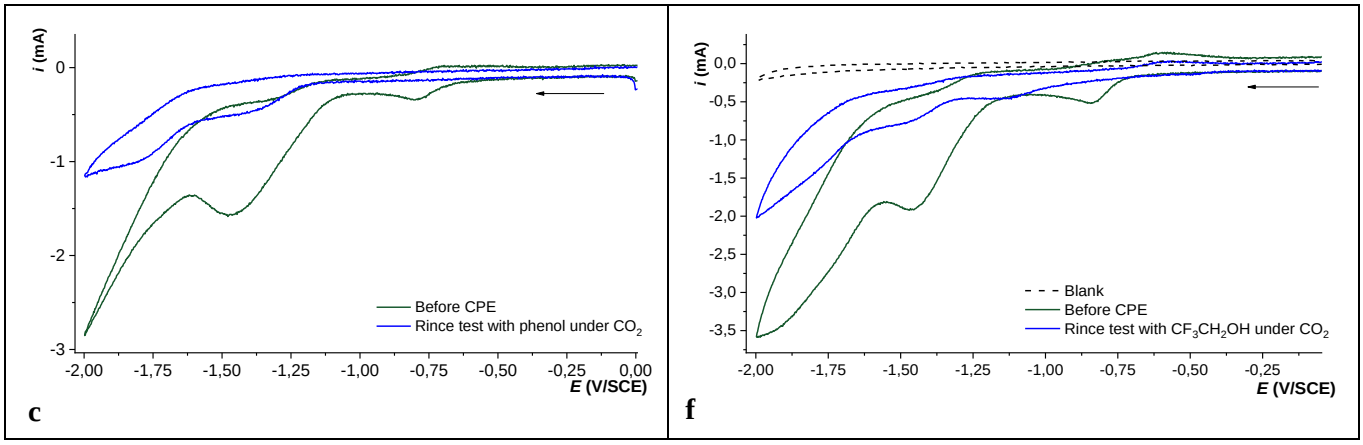

Table S6. **a)** Current (red) and charge (black) overtime during CPE experiments of complex **1** (0.5 mM) in anhydrous DMF under CO_2 with 3 M of phenol. **b)** CVs of a saturated solution of CO_2 in anhydrous DMF with 3 M of phenol (black dashed) of complex **1** (0.5 mM) under CO_2 in anhydrous DMF with 3 M of phenol before CPE (green) and after CPE (red). Glassy carbon electrode of 0.07 cm² area, scan rate of 0.1 $V \cdot s^{-1}$. **c)** CVs of a saturated solution of CO_2 in anhydrous DMF with 3 M of phenol (black dashed) of complex **1** (0.5 mM) under CO_2 in anhydrous DMF with 3 M of phenol before CPE (green) and after CPE with the same glassy carbon plate in a solution without catalyst with 3 M of phenol in DMF under CO_2 (blue). Glassy carbon plate of 2 cm² area, scan rate of 0.1 $V \cdot s^{-1}$. **d)** Current (red) and charge (black) overtime during CPE experiments of complex **1** (0.5 mM) in anhydrous DMF under CO_2 with 1.47 M of CF_3CH_2OH. **e)** CVs of a saturated solution of CO_2 in anhydrous DMF with 1.47 M of CF_3CH_2OH (black dashed) of complex **1** (0.5 mM) under CO_2 in anhydrous DMF with 1.47 M of CF_3CH_2OH before CPE (green) and after CPE (red). Glassy carbon electrode of 0.07 cm² area, scan rate of 0.1 $V \cdot s^{-1}$. **f)** CVs of a saturated solution of CO_2 in anhydrous DMF with 1.47 M of CF_3CH_2OH (black dashed) of complex **1** (0.5 mM) under CO_2 in anhydrous DMF with 1.47 M of CF_3CH_2OH before CPE (green) and after CPE with the same glassy carbon plate in a solution without catalyst with 1.47 M of CF_3CH_2OH in DMF under CO_2 (blue). Glassy carbon plate of 2 cm² area, scan rate of 0.1 $V \cdot s^{-1}$.

8.5 CPE under CO_2 in the presence of 2,2,2–Trifluoroethanol

8.5.1 Comparison CH_3CN/DMF

CH_3CN			**DMF**	
Applied potential (V/SCE)	–1.3		–1.35	
Charge passed (C)	–21.9		–16.8	
Quantity of catalyst (mol)	$2.1 \cdot 10^{-6}$		2.10^{-6}	
Current density (mA/cm²)	1.1		0.8	
Time (s)	10800		10800	
	CO	H_2	CO	H_2
Quantity (mol)	$6.8 \cdot 10^{-5}$	$4.7 \cdot 10^{-7}$	$3.4 \cdot 10^{-5}$	2.10^{-6}
Faradic Efficiency (%)	6	0	39	2
TON	3	0	17	1

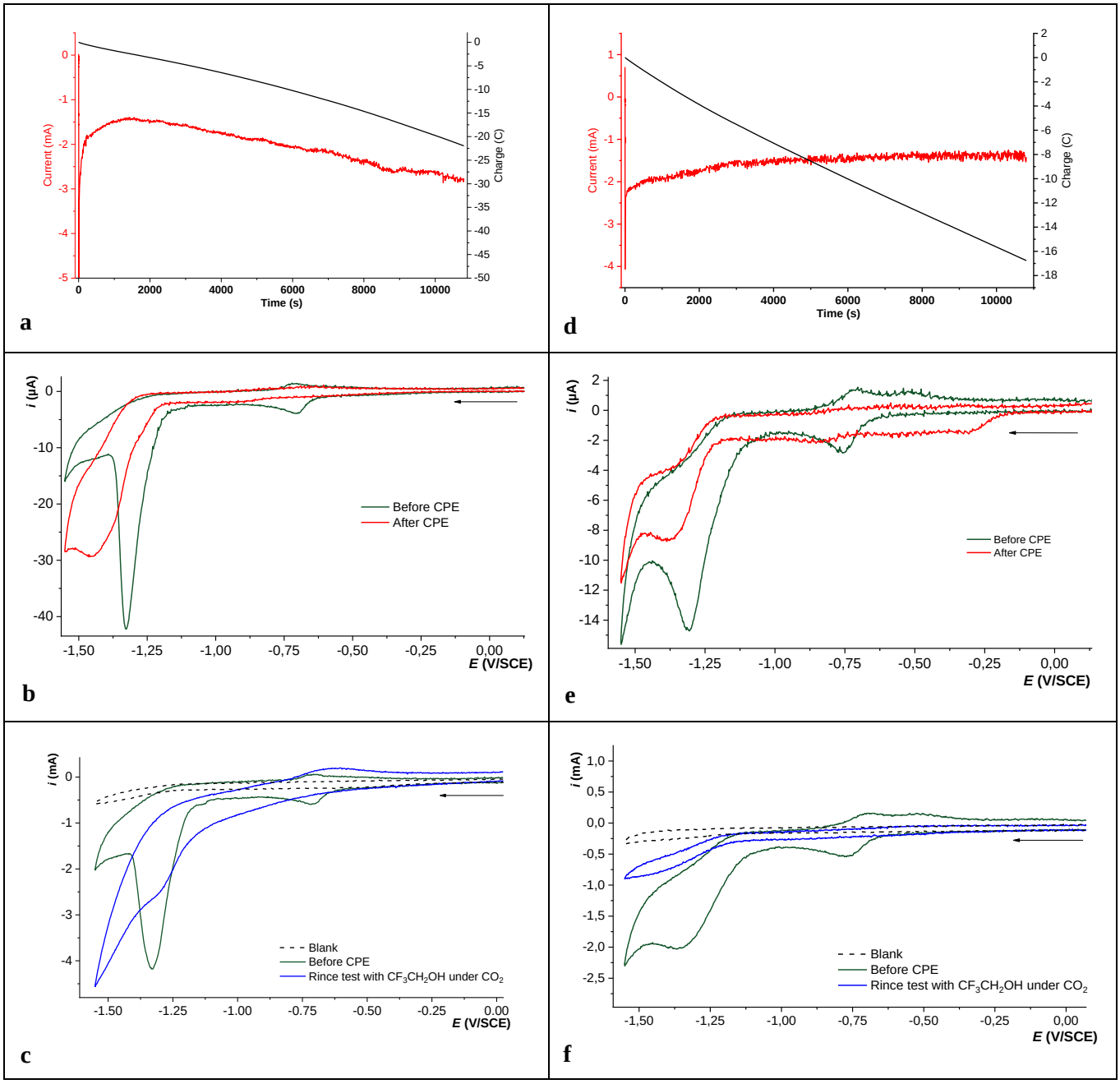

Table S7. **a)** Current (red) and charge (black) overtime during CPE experiments of complex **1** (0.5 mM) in anhydrous CH_3CN under CO_2 with 0.97 M of CF_3CH_2OH at −1.3 V vs SCE. **b)** CVs of complex **1** (0.5 mM) under CO_2 in anhydrous CH_3CN with 0.97 M of CF_3CH_2OH before CPE (green) and after CPE (red). Glassy carbon electrode of 0.03 cm² area, scan rate of 0.1 V $\cdot s^{-1}$. **c)** CVs of a saturated solution of CO_2 in anhydrous CH_3CN with 0.97 M of CF_3CH_2OH (black dashed) of complex **1** (0.5 mM) under CO_2 in anhydrous CH_3CN with 0.97 M of CF_3CH_2OH before CPE (green) and after CPE with the same glassy carbon plate in a solution without catalyst with 0.97 M of CF_3CH_2OH in CH_3CN under CO_2 (blue). Glassy carbon plate of 2 cm² area, scan rate of 0.1 $V \cdot s^{-1}$. **d)** Current (red) and charge (black) overtime during CPE experiments of complex **1** (0.5 mM) in anhydrous DMF under CO_2 with 1.47 M of CF_3CH_2OH. **e)** CVs of complex **1** (0.5 mM) under CO_2 in anhydrous DMF with 1.47 M of CF_3CH_2OH before CPE (green) and after CPE (red). Glassy carbon electrode of 0.03 cm² area, scan rate of 0.1 $V \cdot s^{-1}$. **f)** CVs of a saturated solution of CO_2 in anhydrous DMF with 1.47 M of CF_3CH_2OH (black dashed) of complex **1** (0.5 mM) under CO_2 in anhydrous DMF with 1.47 M of CF_3CH_2OH before CPE (green) and after CPE with the same glassy carbon plate in a solution without catalyst with 1.47 M of CF_3CH_2OH in DMF under CO_2 (blue). Glassy carbon plate of 2 cm² area, scan rate of 0.1 $V \cdot s^{-1}$.

8.5.2 CPE in DMF: use of labelled $^{13}CO_2$ and without catalyst (blank)

$^{13}CO_2$		blank
Applied potential (V/SCE)	–1.44	–1.3 V
Charge passed (C)	–19.5	–7.7
Quantity of catalyst (mol)	$2.2 \cdot 10^{-6}$	0
Current density (mA/cm²)	0.9	0.3
Time (s)	10800	10800

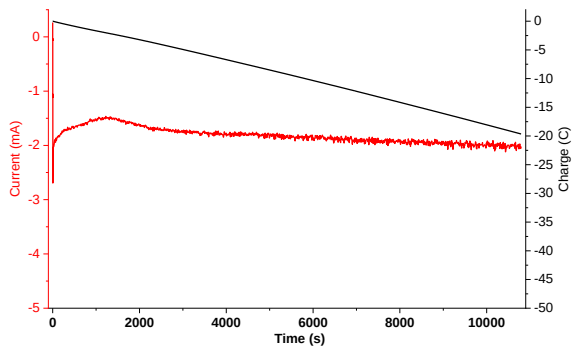

a

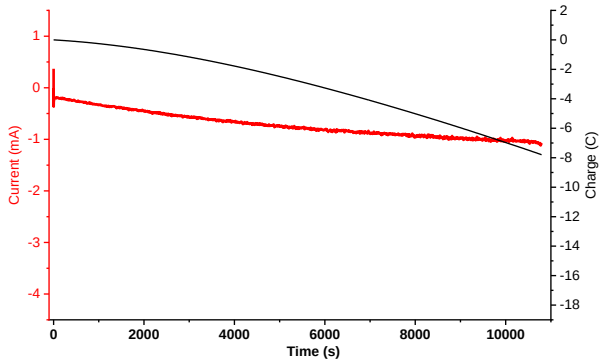

b

Table S8. a) Current (red) and charge (black) overtime during CPE experiments of complex **1** (0.5 mM) in anhydrous DMF under $^{13}CO_2$ with 1.47 M of CF_3CH_2OH. **b)** Current (red) and charge (black) overtime during CPE experiments of complex **1** (0.5 mM) in anhydrous DMF under CO_2 with 1.47 M of CF_3CH_2OH (full line) and without catalyst (dotted line).

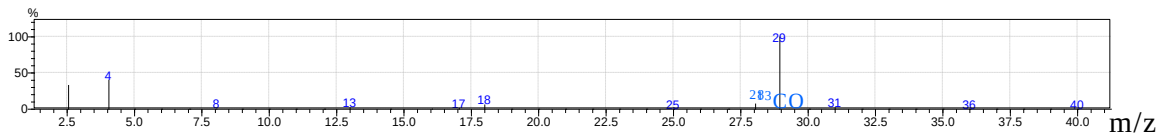

Figure S62. Mass spectra of the headspace corresponding to the previous CPE with labelled $^{13}CO_2$,

8.5.3 CPE in DMF: variation of the temperature

40°C	
Applied potential (V/SCE)	–1.4
Charge passed (C)	–12.7
Quantity of catalyst (mol)	2.10^{-6}
Current density (mA/cm²)	0.6
Time (s)	10800

	CO	H_2
Quantity (mol)	$1.6 \cdot 10^{-5}$	$6.7 \cdot 10^{-7}$
Faradic Efficiency (%)	25	1
TON	8	0

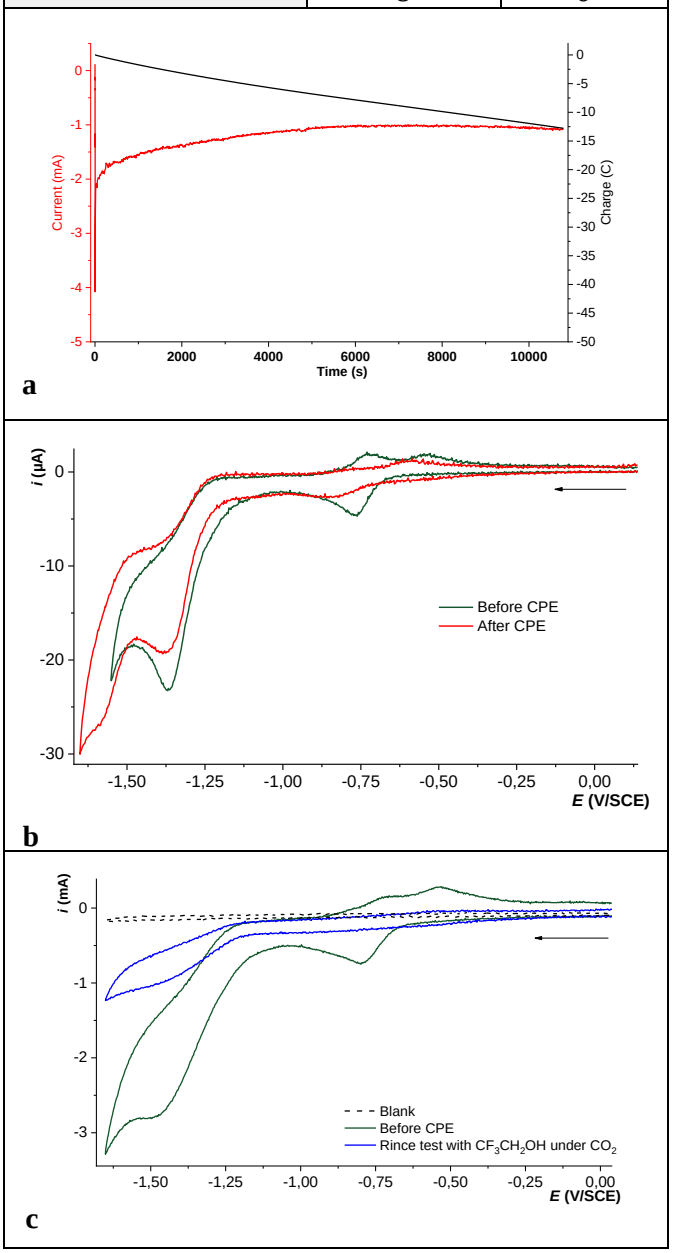

Table S9. **a)** Current (red) and charge (black) overtime during CPE experiments of complex **1** (0.5 mM) in anhydrous DMF under CO_2 with 1.47 M of CF_3CH_2OH at −1.4 V vs SCE. **b)** CVs of complex **1** (0.5 mM) under CO_2 in anhydrous DMF with 1.47 M of CF_3CH_2OH before CPE (green) and after CPE (red). Glassy carbon electrode of 0.03 cm² area, scan rate of 0.1 V $\cdot s^{-1}$. **c)** CVs of a saturated solution of CO_2 in anhydrous DMF with 1.47 M of CF_3CH_2OH (black dashed) of complex **1** (0.5 mM) under CO_2 in anhydrous DMF with 1.47 M of CF_3CH_2OH before CPE (green) and after CPE with the same glassy carbon plate in a solution without catalyst with 1.47 M of CF_3CH_2OH in DMF under CO_2 (blue). Glassy carbon plate of 2 cm² area, scan ratze of 0.1 V$\cdot s^{-1}$.

8.5.4 CPE in DMF: change in the quantity of catalyst

3 mM of complex 1		
Applied potential (V/SCE)	–1.5	
Charge passed (C)	–35.5	
Quantity of catalyst (mol)	$1.2 \cdot 10^{-5}$	
Current density (mA/cm²)	1.6	
Time (s)	10800	
	CO	H_2
Quantity (mol)	$7.8 \cdot 10^{-5}$	$1.6 \cdot 10^{-5}$
Faradic Efficiency (%)	43	9
TON	6	1

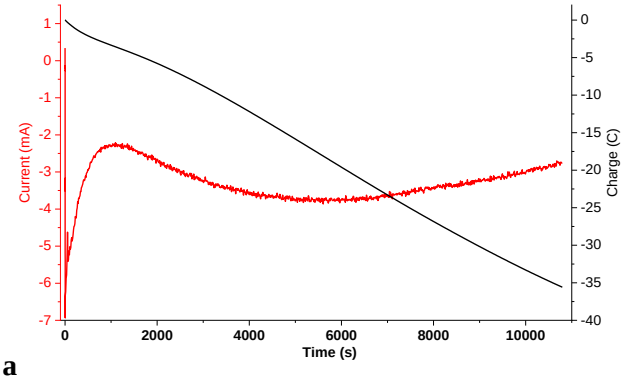

a

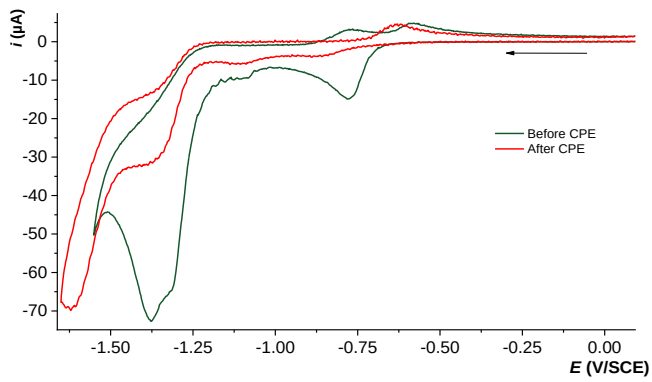

b

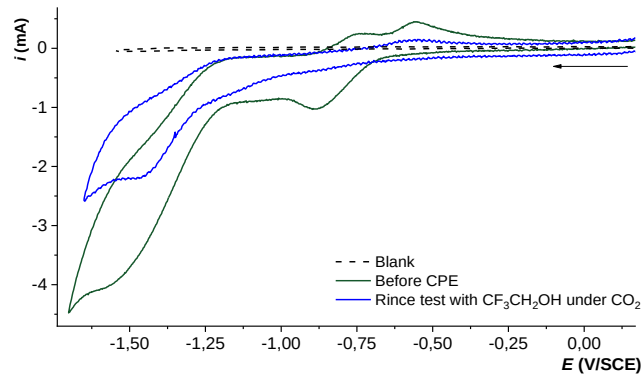

c

Table S10. a) Current (red) and charge (black) overtime during CPE experiments of complex **1** (3 mM) in anhydrous DMF under CO_2 with 1.47 M of CF_3CH_2OH. **b)** CVs of complex **1** (3 mM) under CO_2 in anhydrous DMF with 1.47 M of CF_3CH_2OH before CPE (green) and after CPE (red). Glassy carbon electrode of 0.03 cm² area, scan rate of 0.1 $V \cdot s^{-1}$. **c)** CVs of a saturated solution of CO_2 in anhydrous DMF with 1.47 M of CF_3CH_2OH (black dashed) of complex **1** (3 mM) under CO_2 in anhydrous DMF with 1.47 M of CF_3CH_2OH before CPE (green) and after CPE with the same glassy carbon plate in a solution without catalyst with 1.47 M of CF_3CH_2OH in DMF under CO_2 (blue). Glassy carbon plate of 2 cm² area, scan rate of 0.1 $V \cdot s^{-1}$

8.5.5 CPE in DMF: change in duration

	CPE of 1 hour		CPE of 6 hours	
Applied potential (V/SCE)	–1.38		–1.4	
Charge passed (C)	–4.6		–48.9	
Quantity of catalyst (mol)	$2.4 \cdot 10^{-6}$		2.10^{-6}	
Current density (mA/cm²)	0.6		1.13	
Time (s)	3600		21600	
	CO	H_2	CO	H_2
Quantity (mol)	$8.9 \cdot 10^{-6}$	$1.2 \cdot 10^{-6}$	$5.8 \cdot 10^{-5}$	$1.7 \cdot 10^{-6}$
Faradic Efficiency (%)	38	5	23	1
TON	4	0.5	29	1

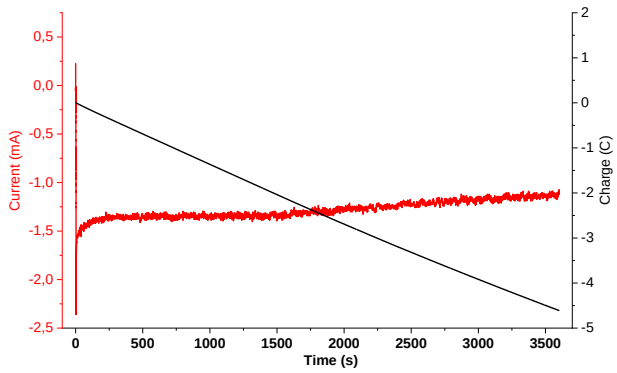

a

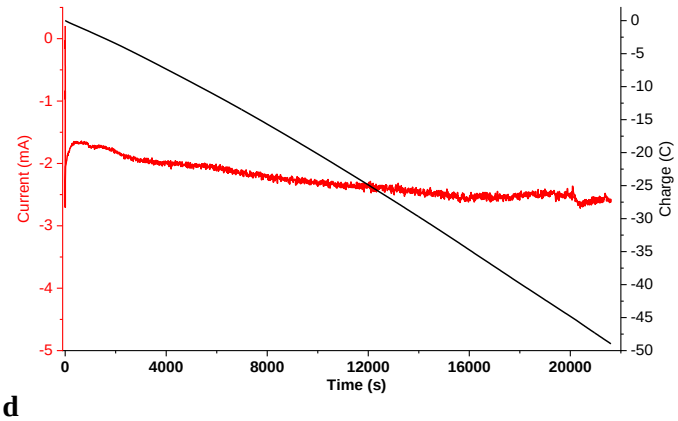

d

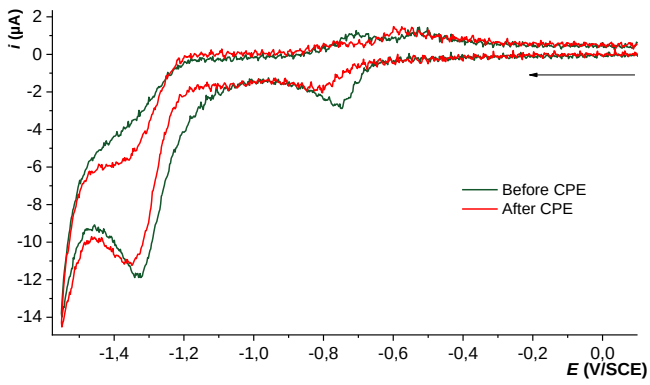

b

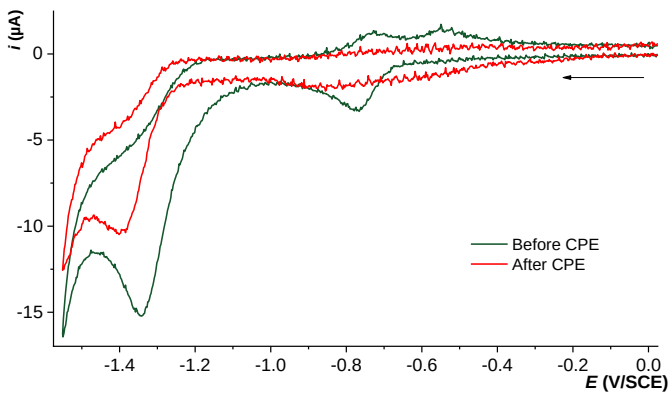

e

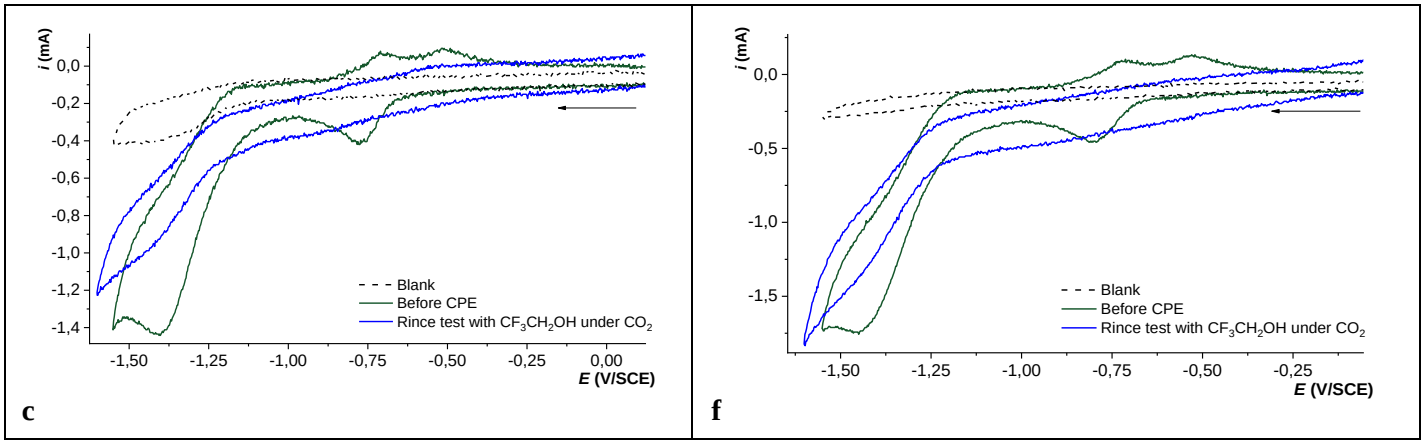

Table S11. a) Current (red) and charge (black) overtime during CPE experiments of complex **1** (0.5 mM) in anhydrous DMF under CO_2 with 1.47 M of CF_3CH_2OH. **b)** CVs of complex **1** (0.5 mM) under CO_2 in anhydrous DMF with 1.47 M of CF_3CH_2OH before CPE (green) and after CPE (red). Glassy carbon electrode of 0.03 cm² area, scan rate of 0.1 $V \cdot s^{-1}$. **c)** CVs of a saturated solution of CO_2 in anhydrous DMF with 1.47 M of CF_3CH_2OH (black dashed) of complex **1** (0.5 mM) under CO_2 in anhydrous DMF with 1.47 M of CF_3CH_2OH before CPE (green) and after CPE with the same glassy carbon plate in a solution without catalyst with 1.47 M of CF_3CH_2OH in DMF under CO_2 (blue). Glassy carbon plate of 2 cm² area, scan rate of 0.1 $V \cdot s^{-1}$. **d)** Current (red) and charge (black) overtime during CPE experiments of complex **1** (0.5 mM) in anhydrous DMF under CO_2 with 1.47 M of CF_3CH_2OH. **e)** CVs of complex **1** (0.5 mM) under CO_2 in anhydrous DMF with 1.47 M of CF_3CH_2OH before CPE (green) and after CPE (red). Glassy carbon electrode of 0.03 cm² area, scan rate of 0.1 $V \cdot s^{-1}$. **f)** CVs of a saturated solution of CO_2 in anhydrous DMF with 1.47 M of CF_3CH_2OH (black dashed) of complex **1** (0.5 mM) under CO_2 in anhydrous DMF with 1.47 M of CF_3CH_2OH before CPE (green) and after CPE with the same glassy carbon plate in a solution without catalyst with 1.47 M of CF_3CH_2OH in DMF under CO_2 (blue). Glassy carbon plate of 2 cm² area, scan rate of 0.1 $V \cdot s^{-1}$.

8.5.6 CPE in DMF: influence of a source of light

CPE of 1 hour under a source of light 447 nm		
Applied potential (V/SCE)	–1.4	
Charge passed (C)	–3.2	
Quantity of catalyst (mol)	2.10^{-6}	
Current density (mA/cm²)	0.4	
Time (s)	10800	
	CO	H_2
Quantity (mol)	$4.2.10^{-6}$	$6.6.10^{-7}$
Faradic Efficiency (%)	25	4
TON	2	0.3

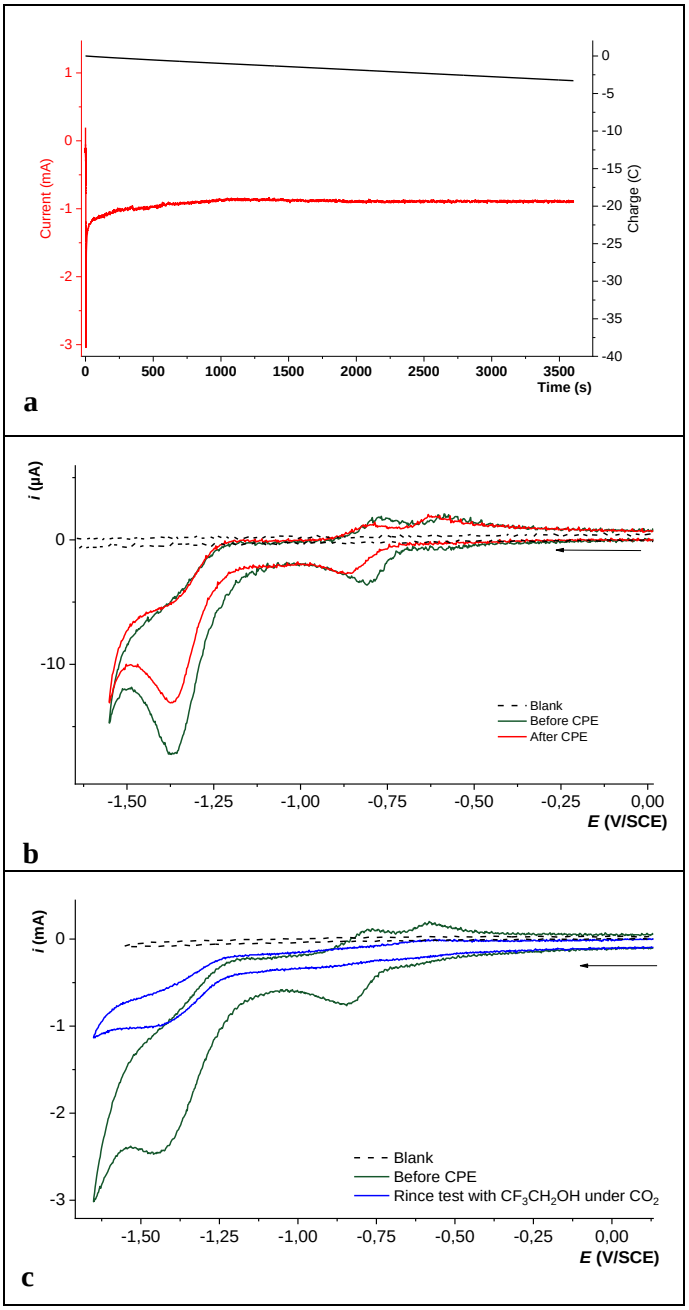

Table S12. **a)** Current (red) and charge (black) overtime during CPE experiments of complex **1** (0.5 mM) in anhydrous DMF under CO_2 with 1.47 M of CF_3CH_2OH. **b)** CVs of a saturated solution of CO_2 in anhydrous DMF with 1.47 M of CF_3CH_2OH (black dashed) of complex 1 (0.5 mM) under CO_2 in anhydrous DMF with 1.47 M of CF_3CH_2OH before CPE (green) and after CPE (red). Glassy carbon electrode of 0.03 cm² area, scan rate of 0.1 $V \cdot s^{-1}$. **c)** CVs of a saturated solution of CO_2 in anhydrous DMF with 1.47 M of CF_3CH_2OH (black dashed) of complex **1** (0.5 mM) under a source of light at 447 nm and CO_2 in anhydrous DMF with 1.47 M of CF_3CH_2OH before CPE (green) and after CPE with the same glassy carbon plate in a solution without catalyst with 1.47 M of CF_3CH_2OH in DMF under CO_2 and a source of light at 447 nm (blue). Glassy carbon plate of 2 cm² area, scan rate of 0.1 $V \cdot s^{-1}$.

8.5.7 CPE in DMF: activity of $CoCl_2$ and L–H

	$CoCl_2$		L–H	
Applied potential (V/SCE)	–1.35		–1.35	
Charge passed (C)	–15		7	
Quantity of catalyst (mol)	4.10^{-6}		2.10^{-6}	
Current density (mA/cm²)	0.7		0.3	
Time (s)	10800		10800	
	CO	H_2	CO	H_2
Quantity (mol)	0	$2.4.10^{-5}$	0	0
Faradic Efficiency (%)	0	32	0	0
TON	0	6	0	0

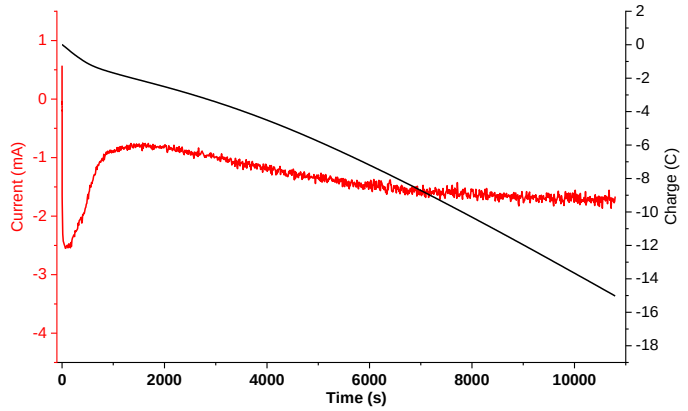

a

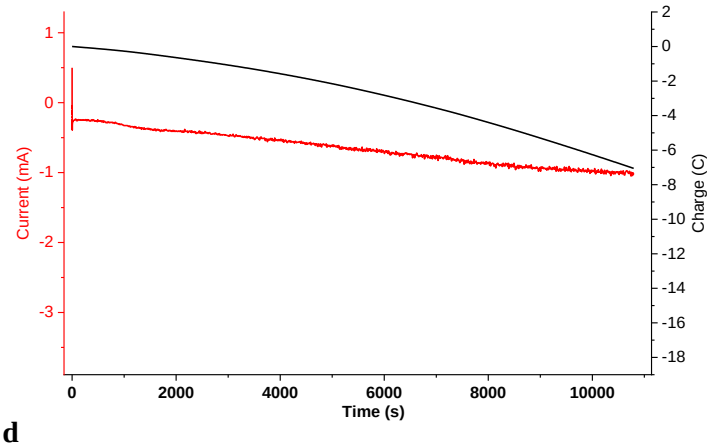

d

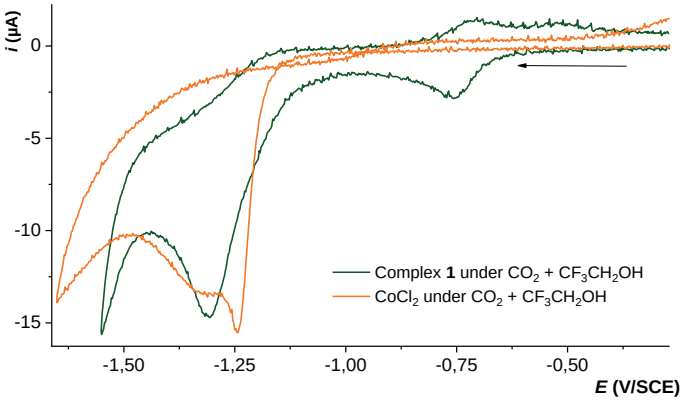

b

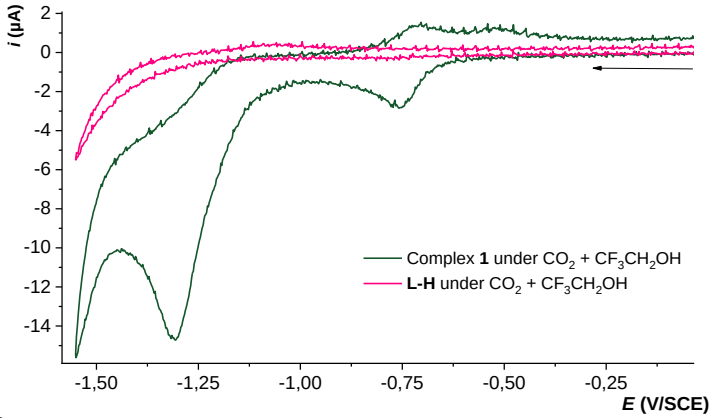

e

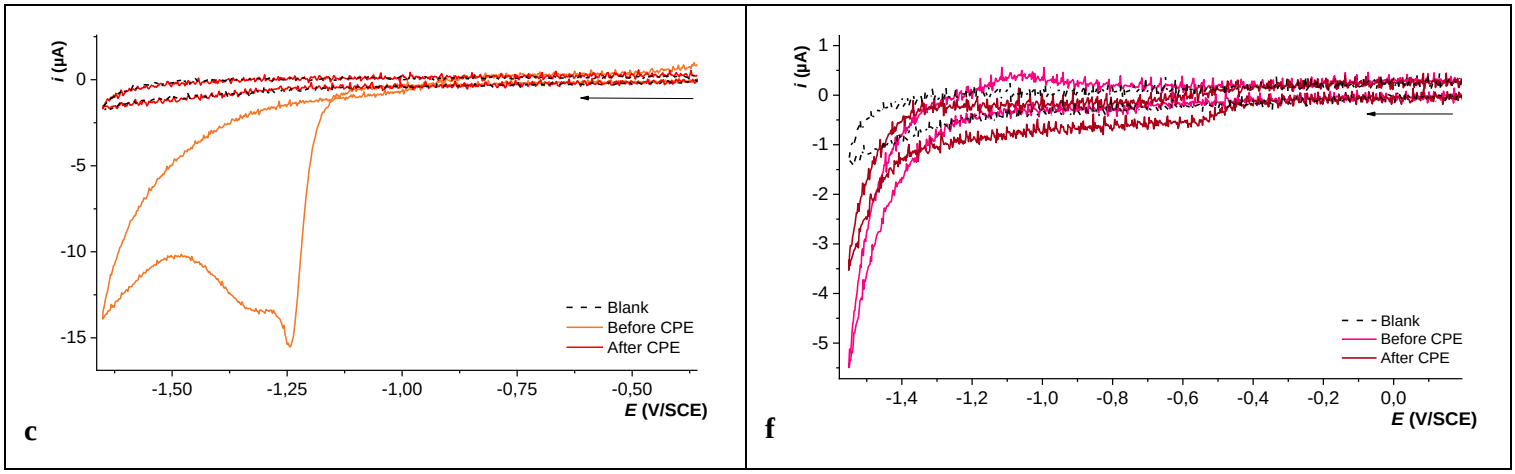

Table S13. a) Current (red) and charge (black) overtime during CPE experiments of complex **1** (full line) and $CoCl_2$ (dotted line) in anhydrous DMF under CO_2 with 1.47 M of CF_3CH_2OH. **b)** CV of complex **1** (0.5 mM) under CO_2 in anhydrous DMF (dark green) with 1.47 M of CF_3CH_2OH before CPE (green) and CV of $CoCl_2$ (1 mM) in the same conditions (orange). Glassy carbon electrode of 0.03 cm² area, scan rate of 0.1 $V \cdot s^{-1}$. **c)** CVs of a saturated solution of CO_2 in anhydrous DMF with 1.47 M of CF_3CH_2OH (black dashed) of $CoCl_2$ (1 mM) under CO_2 in anhydrous DMF with 1.47 M of CF_3CH_2OH before CPE (orange) and after CPE (red). Glassy carbon electrode of 0.03 cm² area, scan rate of 0.1 V s^{-1}. **d)** Current (red) and charge (black) overtime during CPE experiments of **L–H** (0.5 mM) in anhydrous DMF under CO_2 with 1.47 M of CF_3CH_2OH. **e)** CV of complex **1** (0.5 mM) under CO_2 in anhydrous DMF (dark green) with 1.47 M of CF_3CH_2OH before CPE (green) and CV of **L–H** (0.5 mM) in the same conditions (pink). Glassy carbon electrode of 0.03 cm² area, scan rate of 0.1 $V \cdot s^{-1}$. **f)** CVs of a saturated solution of CO_2 in anhydrous DMF with 1.47 M of CF_3CH_2OH (black dashed) of **L–H** (0.5 mM) in anhydrous DMF under CO_2 with 1.47 M of CF_3CH_2OH before CPE (pink) and after CPE (dark red). Glassy carbon electrode of 0.03 cm² area, scan rate of 0.1 $V \cdot s^{-1}$.

Table S14	Solvent	Brönsted Acid	Quantity of catalyst (mol)	Temperature	Time	Applied potential (V/SCE)	Charge passed (C)	CO		H_2		Entry
								TON	FE (%)	TON	FE (%)	
Table S3	CH_3CN	-	$2\cdot10^{-6}$	20°C	8300	–1.95	–12.9	0.3	1	0	0	**(3[a])**
Table S3	DMF	-	$2\cdot10^{-6}$	20°C	10800	–2.05	–3.9	0.1	1	0	0	**(3[b])**
Table S4	CH_3CN	water	$2.3\cdot10^{-6}$	20°C	10800	–1.47	–30	0.6	1	0.7	1	**(4[a])**
Table S4	DMF	water	$3\cdot10^{-6}$	20°C	10800	–1.4	–14.5	4	18	5	21	**(4[b])**
Table S5	CH_3CN	phenol	$2.4\cdot10^{-6}$	20°C	10800	–1.3	–36.7	2	2	0	0	**(5[a])**
Table S5	DMF	phenol	$2\cdot10^{-6}$	20°C	10800	–1.3	–11.9	12	41	3	11	**(5[b])**
Table S6	DMF	phenol	$1.8\cdot10^{-6}$	20°C	10800	–1.8	–26.4	12	16	13	17	**(6[a])**
Table S6	DMF	CF_3CH_2OH	$2.2\cdot10^{-6}$	20°C	10800	–1.8	8.6	5	25	1.5	8	**(6[b])**
Table S7	CH_3CN	CF_3CH_2OH	$2.1\cdot10^{-6}$	20°C	10800	–1.3	–21.9	3	6	0	0	**(7[a])**
Table S7	DMF	CF_3CH_2OH	$2\cdot10^{-6}$	20°C	10800	–1.35	–16.8	17	39	1	2	**(7[b])**

Table S9	DMF	CF_3CH_2OH	$2\cdot10^{-6}$	40°C	10800	–1.4	–12.7	8	25	0	1	**(9)**
Table S10	DMF	CF_3CH_2OH	$1.2\cdot10^{-5}$	20°C	10800	–1.5	–35.5	6	43	1	9	**(10)**
Table S11	DMF	CF_3CH_2OH	$2.4\cdot10^{-6}$	20°C	3600	–1.38	–4.6	4	38	0.5	5	**(11[a])**
Table S11	DMF	CF_3CH_2OH	$2\cdot10^{-6}$	20°C	21600	–1.4	–48.9	29	23	1	1	**(11[b])**
Table S12	DMF	CF_3CH_2OH source of light (447 nm)	$2\cdot10^{-6}$	20°C	10800	–1.4	–3.2	2	25	0.3	4	**(12)**
Table S13	DMF	CF_3CH_2OH	$4\cdot10^{-6}$ ($CoCl_2$)	20°C	10800	–1.35	–15	0	0	6	32	**(13[a])**
Table S13	DMF	CF_3CH_2OH	$2\cdot10^{-6}$ (**L–H**)	20°C	10800	–1.35	–7	0	0	0	0	**(13[b])**

Table S14. **(3[a]).** 2.3 hours CPE of complex **1** (0.5 mM) under CO_2 in anhydrous CH_3CN with 1.6 M of water. **(3[b])** 3 hours CPE of complex **1** (0.5 mM) under CO_2 in anhydrous CH_3CN with 1.6 M of water. **(4[a])** 3 hours CPE of complex **1** (0.5 mM) under CO_2 in anhydrous CH_3CN with 1.6 M of water. **(4[b])** 3 hours CPE of complex **1** (0.5 mM) under CO_2 in anhydrous DMF with 5 M of water. **(5[a])** 3 hours CPE of complex **1** (0.5 mM) under

CO_2 in anhydrous CH_3CN with 1.6 M of phenol. **(5[b])** 3 hours CPE of complex **1** (0.5 mM) under CO_2 in anhydrous DMF with 3 M of phenol. **(6[a])** 3 hours CPE of complex **1** (0.5 mM) under CO_2 in anhydrous DMF with 3 M of phenol. **(6[b])** 3 hours CPE of complex **1** (0.5 mM) under CO_2 in anhydrous DMF with 1.47 M of CF_3CH_2OH. **(7[a])** 3 hours CPE of complex **1** (0.5 mM) under CO_2 in anhydrous CH_3CN with 0.97 M of CF_3CH_2OH. **(7[b])** 3 hours CPE of complex **1** (0.5 mM) under CO_2 in anhydrous CH_3CN with 1.47 M of CF_3CH_2OH. **(9)** 3 hours CPE of complex **1** (0.5 mM) under CO_2 in anhydrous DMF with 1.47 M of CF_3CH_2OH at 40°C. **(10)** 3 hours CPE of complex **1** (3 mM) under CO_2 in anhydrous DMF with 1.47 M of CF_3CH_2OH. **(11[a])** 1 hour CPE of complex **1** (0.5 mM) under CO_2 in anhydrous DMF with 1.47 M of CF_3CH_2OH. **(11[b])** 6 hours CPE of complex **1** (0.5 mM) under CO_2 in anhydrous DMF with 1.47 M of CF_3CH_2OH. **(12)** 3 hours CPE of complex **1** (0.5 mM) under CO_2 in anhydrous DMF with 1.47 M of CF_3CH_2OH under a source of light at 447 nm. **(13[a])** 3 hours CPE of $CoCl_2$ (1 mM) under CO_2 in anhydrous DMF with 1.47 M of CF_3CH_2OH. **(13[b])** 3 hours CPE of **L–H** (0.5 mM) under CO_2 in anhydrous DMF with 1.47 M of CF_3CH_2OH.

9 References

[1] F. W. Lewis, L. M. Harwood, M. J. Hudson, M. G. B. Drew, M. Sypula, G. Modolo, D. Whittaker, C. A. Sharrad, V. Videva, V. Hubscher-Bruder, F. Arnaud-Neu, *Dalton Trans.* **2012**, *41*, 9209–9219.

[2] J. I. van der Vlugt, S. Demeshko, S. Dechert, F. Meyer, *Inorg. Chem.* **2008**, *47*, 1576–1585.

[3] C. Amatore, M. Azzabi, P. Calas, A. Jutand, C. Lefrou, Y. Rollin, *Journal of Electroanalytical Chemistry and Interfacial Electrochemistry* **1990**, *288*, 45–63.